

Development of an in-Xe-gas Laser Ablation Source for the Ba-tagging technique for nEXO

Melissa Medina Peregrina, Faculty of Science

McGill University, Montreal

September, 2020

A thesis submitted to McGill University in partial fulfillment of the
requirements of the degree of

Master of Science in Physics

©Melissa Medina Peregrina, 2020

Abstract

nEXO is a next generation experiment searching for neutrinoless double beta decay ($0\nu\beta\beta$) in the isotope ^{136}Xe . An observation of this decay would imply lepton number violation and require the neutrino to be its own antiparticle. Such an observation would demonstrate physics beyond the Standard Model of particle physics and alter our understanding of the universe.

To increase nEXO's sensitivity in a future upgrade and to verify a potential signal as originating from true double decay ($\beta\beta$) events, the collaboration is developing a Ba-tagging technique with the aim of identifying the ^{136}Xe decay daughter ^{136}Ba . In this scheme, the decay volume is probed for the presence of Ba when a candidate $0\nu\beta\beta$ event is detected. Since ^{136}Ba is only produced in $\beta\beta$ decays, the event can be identified as a double beta decay of ^{136}Xe and backgrounds can be discarded.

The nEXO collaboration is investigating different approaches to extract and identify single barium ions. In Canada, groups at Carleton, McGill, and TRIUMF are working on extracting ions from liquid Xe into a gaseous environment and subsequently into vacuum for final identification of the barium ion. The group at McGill University is developing a laser ablation ion source to be operated in high pressure Xe-gas. This ablation source is intended to provide ions to study and optimize the ion extraction process. This thesis describes the setup, an analysis of the measured ion current in vacuum as function of different physical parameters along with future plans for this ion source. All in-gas measurements were interrupted because of COVID-19 and had to be postponed until after this MSc thesis.

Abrégé

nEXO est une expérience novatrice recherchant à détecter la double désintégration bêta sans neutrino ($0\nu\beta\beta$) dans l'isotope ^{136}Xe . Une observation de cette désintégration impliquerait une violation du nombre leptonique et exigerait que le neutrino soit sa propre antiparticule. Une telle observation démontrerait un phénomène au-delà du modèle standard de la physique des particules et modifierait notre compréhension de l'univers.

Pour augmenter la sensibilité de nEXO lors d'une future mise à jour et pour vérifier qu'un signal soit produit par une double désintégration ($\beta\beta$), notre collaboration développe une technique de traçage de Ba dans le but d'identifier le produit de la désintégration de ^{136}Xe , ^{136}Ba . Le volume de désintégration est sondé pour déterminer la présence de Ba lorsqu'un événement candidat $0\nu\beta\beta$ est détecté. Puisque ^{136}Ba n'est produit que dans les désintégrations $\beta\beta$, l'événement peut être identifié comme une désintégration bêta double de ^{136}Xe et les bruits de fond peuvent être supprimés.

La collaboration nEXO étudie différentes approches pour extraire et identifier des ions baryum uniques. Au Canada, des groupes de Carleton, McGill et TRIUMF travaillent sur l'extraction d'ions du Xe liquide dans un environnement gazeux et par la suite dans le vide pour l'identification finale de l'ion baryum. Le groupe de l'Université McGill développe une source d'ions d'ablation au laser qui fonctionnera dans du gaz Xe haute pression. Cette source d'ablation est destinée à fournir des ions pour étudier et optimiser le processus d'extraction d'ions. Cette thèse décrit la configuration, une analyse du courant ionique mesuré dans le vide en fonction de différents paramètres physiques ainsi que les plans futurs pour cette source d'ions. Toutes les mesures dans une chambre à gaz

ont été interrompues à cause de la COVID-19 et ont dû être reportées après la soumission de cette thèse de maîtrise.

Statement of originality

This is to certify that to the best of my knowledge:

The content of this thesis is the product of my own work and research. All data presented in chapter 4 was taken by me. The scripts to analyze data were written in C++ and plotted with gnuplot by me. The design and the assembly of the pressure chamber presented in Figure 3.5 was done by Dr. Yuta Ito. The simulations shown in Figure 3.1 were made by me using SIMION. The design and construction of the external gas line and the overall layout of the Laser Ablation Source shown in Figure 2.4, was made by me and Dr. Christopher Chambers. The in-Xe-gas monitor shown in Figure 3.7 was modified by me from a current monitor. This allowed it to be adapted to non-vacuum conditions. This work does not contain any previously published material by someone else nor does it include falsified content. I have clearly referenced all sources used in the work.

Melissa Medina Peregrina

Acknowledgements

I would like to start by acknowledging everyone who helped me in enrolling McGill University, my former professors from UABC, Tanya Zazueta and Leonardo Espinoza. Thanks to my supervisor Dr. Thomas Brunner for giving me the opportunity to join the Brunner Neutrino Lab and the nEXO collaboration by working on a project where I developed countless experimental skills and made me grow as a scientist.

I would also like to thank Zoé McIntyre, Cindy Pham, and everyone I got to work with during the master courses. Thanks to everyone from my research group for their friendship and particularly to Dr. Christopher Chambers for his guidance, patience and for always being available to help me.

Finally, I would like to thank Mamá Felis, my parents Socorro and Rigoberto, my siblings Kevin, Hiram and Ayleen, and God for giving me the strength to continue whenever I needed.

Contents

Abstract	i
Abrégé	ii
List of Figures	x
List of Tables	1
1 Introduction	2
1.1 Neutrinos	2
1.2 Neutrino oscillations	3
1.3 Neutrinoless double beta decay	5
1.4 Searching for $0\nu\beta\beta$ decay in liquid xenon with EXO-200 and nEXO	8
1.5 The Ba-tagging technique as an upgrade path to nEXO	11
2 Laser ablation	14
2.1 Laser Ablation Sources	14
2.1.1 General working principle of an ion source	15
2.1.2 Basic power requirements and optical considerations	15
2.1.3 Ion ejection and plasma plume	20
2.2 Applications of LAS for Ba-tagging	21
2.2.1 In vacuum LAS	21
2.2.2 In-gas LAS	22
3 Methodology and setup	24
3.1 Simulation	24

3.2	The McGill LAS setup	28
3.2.1	In vacuum LAS	32
3.2.2	In-gas Laser Ablation Source (IGLAS) setup	32
4	Measurements	37
4.1	Beam spot size measurements	37
4.1.1	Beam spot determination through superficial ablation marks	38
4.1.2	Beam spot determination through Gaussian optics	40
4.1.3	Comparison of beam spot measurements	40
4.2	Current resolution measurements	43
4.3	In-Vacuum measurements	46
4.3.1	Ion plume	46
4.3.2	Laser position and field dependence of ion current	48
4.3.3	Ion current dependence on the target position and geometry	54
4.3.4	Gold sample ablation measurements	63
4.4	In-gas studies	74
5	Conclusions and outlook	76
	Appendix	79

List of Figures

1.1	Mass hierarchies	4
1.2	$0\nu\beta\beta$ Feynman diagram	6
1.3	Theoretical $\beta\beta$ -decay electron energy spectrum.	7
1.4	Artist's view of the EXO-200 experiment	10
1.5	Artist's view of the nEXO experiment	11
1.6	Schematic of the Ba-tagging extraction and identification process	12
2.1	Effects on the variation of laser parameters	17
2.2	Effects on the variation of laser parameters	18
2.3	Evolution of an ablation plume in a gaseous environment	19
2.4	Schematic of the McGill Laser Ablation Source	23
3.1	Virtual design of the pressure chamber.	25
3.2	Simulation results for Au ablation.	27
3.3	Au and Cu ions drift velocity in gas	28
3.4	Laser Ablation Source layout	29
3.5	IGLAS system	33
3.6	Rectangular Cu sample attached to the pressure chamber.	35
3.7	LAS in-Xe-gas monitor	36
4.1	Circular-shaped copper target	39
4.2	Superficial ablation marks on the Cu target	41
4.3	UV beam profile study	42

4.4	Circuit for the study of data acquisition	43
4.5	Resolution Measurements results	44
4.6	Laser ablation over the same and different spots	47
4.7	Ions cloud in a copper target surface	47
4.8	Ion current decaying behaviour when ablation occurs in the same spot . . .	49
4.9	Ion current decaying behaviour when ablation occurs in various positions. .	50
4.10	Ion current as function of the absolute value of the applied voltage on the collector plate in copper	52
4.11	Ablation marks on the surface of the copper sample	53
4.12	Scan pattern followed over the surface of the biased copper target.	54
4.13	Resulting ion current at various applied voltages in copper	55
4.14	Resulting heat map for the rectangular Cu target.	56
4.15	1D scans of the rectangular Cu target	57
4.16	Change in the copper target geometry	58
4.17	Copper target geometry change with an applied bias	58
4.18	Ion current plot as function of applied voltages in the circular target and in the collector plate	59
4.19	1D scans of the circular Cu target	61
4.20	Diffuse reflection	61
4.21	Ion plume with circular geometry in a copper sample.	62
4.22	In-Vacuum setup with Au foil target.	64
4.23	1D scans of the Au target	65
4.24	Variation on the repetition rate	67
4.25	Laser power variation on the Au target	68
4.26	Au ions cloud	69
4.27	Measured current with the Au target	70
4.28	Measured current as function of the electrodes applied bias	71
4.29	Comparison of Cu and Au results using the same ion current scale	72

4.30 Ion current efficiency	73
1 Laser trajectory followed by the UV beam	80
2 Schematic of the added gas line.	81
3 IGLAS gas line connecting the pressure chamber to the gas source	82
4 Cu in Xe simulations	83
5 Ion clouds comparison	84

List of Tables

1.1	Comparison of current experimental limits of $0\nu\beta\beta$ searches.	8
3.1	Considered parameters for the SIMION simulations.	26
4.1	Laser percentage and power	38
4.2	Beam spot size results	42
4.3	Resolution results	45
4.4	Histogram results	46
4.5	1D scans in gold	64
4.6	Changing the laser repetition rate in Au	66
4.7	Changing the laser power in Au	66

Chapter 1

Introduction

1.1 Neutrinos

Neutrinos are the second most abundant known particles in the universe after photons. Despite their abundance, we know very little about these elusive particles. A fundamental property of all elementary particles such as their mass, is yet to be determined. Neutrinos are electrically neutral weakly interacting elementary particles classified as *leptons* due to their half-integer spin nature, according to the Standard Model of Physics [1]. The neutrino was first postulated by W. Pauli to explain the continuous energy spectrum in beta decays [2]. Pauli stated that this particle could explain the difference in energy and angular momentum in the initial and final states of the decay. This proposed particle was thought to be electrically neutral in order to preserve conservation laws and to explain why it was undetectable at that time.

Neutrinos interact through gravity and weak forces. Neutrinos are to date the only known fermions without a net charge. This implies that neutrinos could be *Majorana particles*, this is, their own antiparticle¹. This would have a very important impact on the understanding of the origin of neutrino masses and mixing [3].

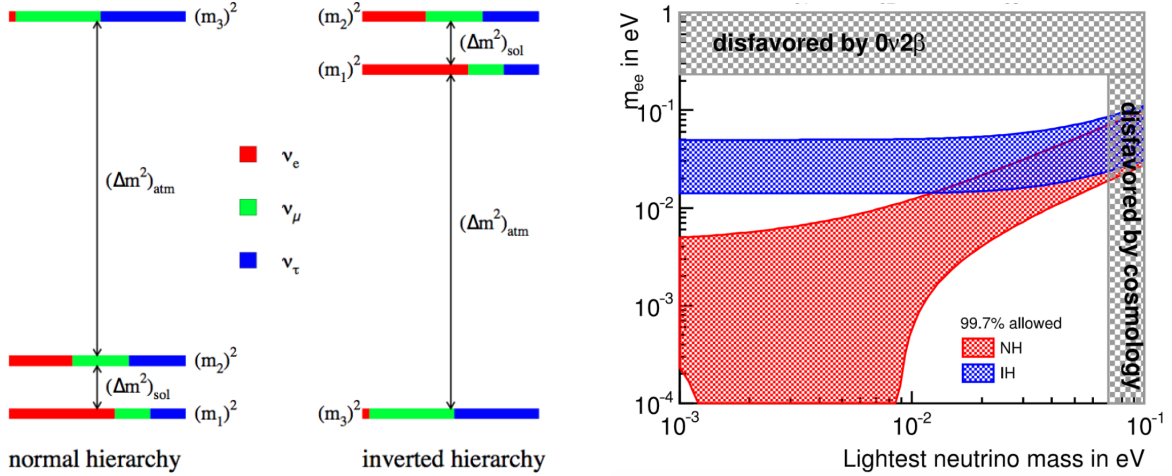
¹Antiparticles have the same mass value but opposite charge. For instance, the electron charge is negative and its antiparticle, the positron is positively charged.

1.2 Neutrino oscillations

There are three different flavors of neutrinos: electron neutrino (ν_e), muon neutrino (ν_μ) and tau neutrino (ν_τ). A unique phenomenon about these neutrinos is known as “neutrino oscillations” in which one neutrino flavor oscillates into another neutrino flavor. For example, an electron neutrino can turn into a tau neutrino or a muon neutrino. This was demonstrated by Super Kamiokande [4], KamLAND [5], and SNO [6] in the early 2000s², showing that at least two of these known neutrinos have non-zero masses.

Within the Standard Model, neutrinos were postulated to be massless. However, neutrino oscillations only happen if the lepton flavor numbers L_e , L_μ and L_τ are not conserved ($\Delta L_x \neq 0$) by the neutrino mass term, thus the study of neutrinos could reveal lepton CP violation, resulting in the discovery of physics beyond the Standard Model [8]. From the KamLAND [5] experiment, the magnitude of the mass-squared difference between neutrino mass eigenstates ν_1 and ν_2 is known and from atmospheric neutrino experiments it is known that there is a larger gap between the ν_3 mass eigenstate and the two other mass eigenstates. This leads to two possible mass hierarchies for the ordering of the neutrino mass eigenstates as shown in Figure 1.1(a). These are called *normal* and *inverted hierarchy*. In the normal hierarchy, the ν_3 state is considered to be the heaviest ($m_3 > m_2 > m_1$), whereas for the inverted hierarchy, this same state is considered to be the lightest ($m_2 > m_1 > m_3$). In addition, there is an specific case called *degenerate hierarchy* that follows the conditions when $m_3 \sim m_2 \sim m_1$. Moreover, neutrino flavor oscillations depend on Δm_{21}^2 , Δm_{32}^2 and Δm_{31}^2 , where $\Delta m_{ij}^2 = m_i^2 - m_j^2$ with $i, j=1,2,3$ and $j \neq i$. Since it is not possible to determine the sign of Δm_{31}^2 , the absolute neutrino mass scale is still unknown.

²T.Kajita and A. McDonald received the Nobel Prize in Physics in 2015. Takaaki Kajita started research in the late 80s, but it was not until 1998 when he wrote about neutrino oscillations for the first time [7]



(a) Possible neutrino mass hierarchies. Each color represents a different neutrino flavor. The sub-index 'sol' indicates that the information is obtained from solar ν oscillations and 'atm' represents values from atmospheric ν oscillations. Obtained from [9].

(b) Effective Majorana mass vs. the minimum neutrino mass (mass of the lightest neutrino) for normal, and inverted hierarchies. Obtained from [10].

Figure 1.1: Top picture: Schematic representation of the mass hierarchies. The proper understanding of these masses is the main motivation for searching for new particle physics phenomena. Bottom picture: Values for the effective Majorana mass as a function of the lightest neutrino mass for both hierarchies.

The most sensitive way to study the possible non-conservation of lepton number and small Majorana neutrino masses is through a hypothetical process called neutrinoless double beta decay. If $0\nu\beta\beta$ does indeed proceed through light neutrino exchange, the $0\nu\beta\beta$ decay half life [11] can be expressed as

$$\frac{1}{T_{1/2}^{0\nu}} = G^{0\nu} |M^{0\nu}|^2 \frac{\langle m_\nu \rangle^2}{m_e^2}. \quad (1.1)$$

In this expression $G^{0\nu}$ is the phase space factor, $|M^{0\nu}|^2$ is the nuclear matrix element, and $\langle m_\nu \rangle$ is the so-called *effective Majorana neutrino mass*, which is defined as

$$\langle m_\nu \rangle = \left| \sum_{i=1}^3 U_{ei}^2 m_i \right|, \quad (1.2)$$

where U_{ei} represents the Pontecorvo–Maki–Nakagawa–Sakata (PMNS) matrix (the e subscript ensures only electron-neutrino mixing components) and m_i denotes the i -th neutrino mass eigenvalue.

The range for the effective Majorana mass values can be displayed as a function of the lightest neutrino mass and the hierarchy of the mass splittings measured through oscillations as shown in Figure 1.1(b).

1.3 Neutrinoless double beta decay

Some nucleons can decay through *beta decay* as one form of weak interaction. The process named *beta minus* (β^-) decay turns a neutron into a proton with the emission of an electron (e^-) and an electron anti-neutrino ($\bar{\nu}_e$),

$$n \rightarrow p + e^- + \bar{\nu}_e. \quad (1.3)$$

The beta decay theory was first proposed by Enrico Fermi in 1934, considering the neutral particles proposed previously by Wolfgang Pauli [12]. An extension of the model, known as *double beta decay* ($2\nu\beta\beta$), was first proposed by Maria Goeppert-Mayer in 1935 [13]. $2\nu\beta\beta$ decay occurs in a nucleus with mass number A and proton number Z when single beta decay is energetically forbidden and decaying to a $Z+2$ proton number daughter nucleus is possible. The $2\nu\beta\beta$ decay is found in nature and the existence of this process has been verified in only a few species [14] including ^{82}Se [15] and ^{136}Xe [16]. In addition to converting two neutrons into protons, two electrons and two anti-neutrinos are simultaneously emitted as result of the decay, as

$$2n \rightarrow 2p + 2e^- + 2\bar{\nu}_e. \quad (1.4)$$

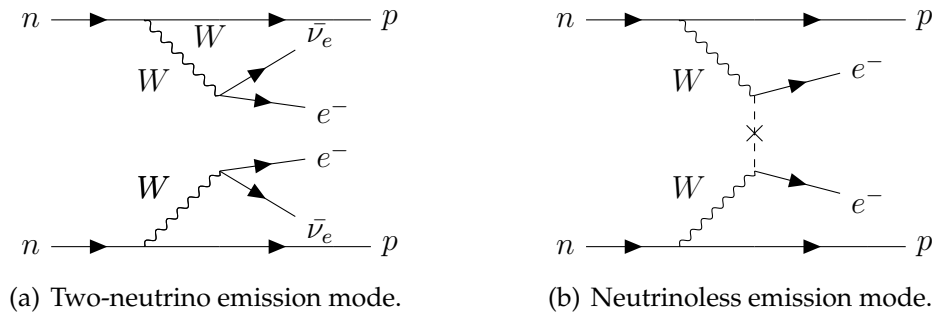
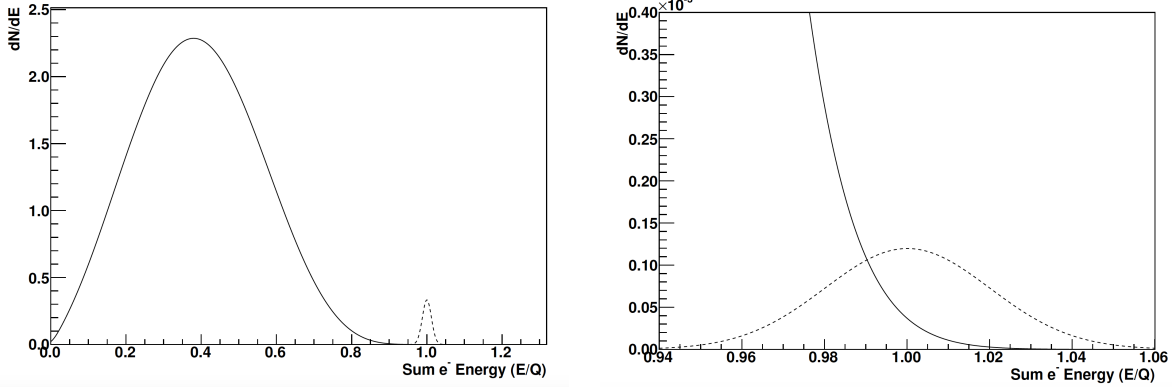


Figure 1.2: Feynman diagrams of the two double beta decay modes. In these processes two neutrons decay into two protons, two electrons and either two neutrinos as shown in Figure a) or no neutrinos as shown in Figure b).

A Feynman diagram representing this process is shown in Figure 1.2(a).

In 1937 the *neutrinoless* emission mode for double beta decay ($0\nu\beta\beta$ decay) was proposed by Ettore Majorana [17]. The $0\nu\beta\beta$ decay is a hypothetical decay that has yet to be discovered. In $0\nu\beta\beta$ decay, only the transformation from a Z proton number nucleus to a $Z+2$ daughter nucleus and the creation of two electrons occur as shown in Figure 1.2(b). This process can only occur in isotopes where $2\nu\beta\beta$ occurs.

For the two-neutrino emission mode, the spectrum is continuous since the released energy is mainly shared between the emitted particles, this is electrons and neutrinos. In the neutrinoless mode only electrons are emitted, implying that almost all the energy is transferred to them. The latter situation leads to a mono-energetic line at the Q -value in the spectrum [18]. The difference in the sum electron spectrum for the two modes can be seen in Figure 1.3. The allowed $2\nu\beta\beta$ decay results in a continuous spectrum, displayed as a solid line, while the hypothetical $0\nu\beta\beta$ decay will result in a mono-energetic peak at the Q -value, shown as dashed line. Two scenarios are plotted: Figure 1.3(a) assumes a case where one $0\nu\beta\beta$ decay occurs in 100 $\beta\beta$ decays. This scenario has been excluded experimentally. Figure 1.3(b) shows the spectrum where only 10^{-6} decays are $0\nu\beta\beta$ decays.



(a) Electron sum energy spectrum of the two double beta decay modes. The plot is normalized and the rate of $0\nu\beta\beta$ is 100 times less than that of $2\nu\beta\beta$. (b) Zoom into the region of interest around the Q-value. The $0\nu\beta\beta$ rate is 1×10^6 times smaller than the allowed $2\nu\beta\beta$ rate.

Figure 1.3: Theoretical $\beta\beta$ -decay electron energy spectrum with the energy scale normalized by the Q-value. Energy spectra of the electrons emitted in $2\nu\beta\beta$ decay are represented by a solid line, whereas the energies of the electrons emitted in neutrinoless mode are represented by a dashed line. Figures (a) and (b) show cases where $0\nu\beta\beta$ is 10^2 and 10^6 times weaker than $2\nu\beta\beta$, respectively. This energy spectrum was smeared with a 2% σ/E energy resolution. Obtained from [19].

In this case, the $0\nu\beta\beta$ peak has a significant overlap with the $2\nu\beta\beta$ spectrum.

The first experiments searching for the existence of neutrinoless double beta decay started before the discovery of the neutrino itself in 1955. Moreover, as one of the first investigations on $0\nu\beta\beta$ decay, E.L. Fireman searched for electrons from the transition $^{124}\text{Sn} \rightarrow ^{124}\text{Te}$ [20]. These experiments were thought to give a hint on the nature of the decay.

At least 35 isotopes are known to undergo $\beta\beta$ decay, however, not all of them are candidate isotopes for $0\nu\beta\beta$ decay searches [21]. Worldwide, there are several experiments searching for $0\nu\beta\beta$ decay using different techniques and different decay candidate isotopes as sources. Some of the experiments searching for this phenomenon are listed in Table 1.1, along with their published sensitivity (the half life limit assuming null signal, which depends on exposure, background index, and resolution), exposure (the mass of

Isotope	Exposure (kg × yr)	Sensitivity (×10 ²⁵ yr)	$T_{1/2}^{0\nu}$ (×10 ²⁵ yr)	$m_{\beta\beta}$ (eV)	Experiment
⁴⁸ Ca	13.5	1.8×10^{-3}	$> 5.8 \times 10^{-3}$	$< 3.5 - 22$	ELEGANT VI [22]
⁷⁶ Ge	82.4	11	> 9	$< 0.07 - 0.16$	GERDA [23]
	26.0	4.8	> 2.7	$< 0.20 - 0.43$	Majorana Demonstrator [24]
⁸² Se	5.29	5.0×10^{-1}	$> 3.5 \times 10^{-1}$	$< 0.31 - 0.64$	CUPID-0 [25]
⁹⁶ Zr	(-)	(-)	$> 9.2 \times 10^{21}$	$< 7.2 - 19.5$	NEMO-3 [26]
¹⁰⁰ Mo	34.3	(-)	1.1×10^{-1}	$< 0.33 - 0.62$	NEMO-3 [27]
¹¹⁶ Cd	(-)	(-)	$> 2.2 \times 10^{-2}$	$< 1.0 - 1.7$	Aurora [28]
¹²⁸ Te	(-)	(-)	$> 1.1 \times 10^{-2}$	(-)	[29]
¹³⁰ Te	372.5	1.7	3.2	$< 0.08 - 0.35$	CUORE [30]
¹³⁶ Xe	504	5.6	> 10.7	$< 0.06 - 0.17$	KamLAND-Zen [31]
	234.1	5.0	> 3.5	$< 0.09 - 0.29$	EXO-200 [32]
¹⁵⁰ Nd	0.19	(-)	$> 2.0 \times 10^{-3}$	$< 1.6 - 5.3$	NEMO-3 [33]

Table 1.1: Comparison of current experimental limits of $0\nu\beta\beta$ searches. The table lists exposure and sensitivity of searches in various elements. The half-life limits and the resulting limits on the effective Majorana neutrino mass are shown for the various experiments. $T_{1/2}^{0\nu}$ denotes the 0ν half-time and $m_{\beta\beta}$ the effective Majorana neutrino mass.

the target isotope times the time the data was taken, considering only the isotopic abundance), $T_{1/2}^{0\nu}$ limits (influenced by statistics), and effective Majorana neutrino mass ($m_{\beta\beta}$).

1.4 Searching for $0\nu\beta\beta$ decay in liquid xenon with EXO-200 and nEXO

EXO-200 was an experiment in which 175 kilograms of liquid xenon enriched in ¹³⁶Xe at 80.6% [34] were employed searching for $0\nu\beta\beta$ decay. The experiment consisted of a double wall copper cryostat and a lead shield (see Figure 1.4) to reach low radiation backgrounds. The xenon was deployed in a Time-Projection Chamber (TPC) that recorded energy, location and event multiplicity of detected events. The TPC acted as a calorimeter to measure the electron energy spectrum [34]. It recorded charge and scintillation light of detected events by using a set of wire anodes and Large Area Avalanche Photodiodes

APDs, respectively. EXO-200 was located underground at the Waste Isolation Pilot Plant (WIPP) in New Mexico, USA. From 2011 when data acquisition began until its decommission in 2018 no evidence of $0\nu\beta\beta$ was detected leading to a limit on the half-life of 3.5×10^{25} and a sensitivity of 5.0×10^{25} at 90% confidence level [32]. However, with EXO-200 it was possible to observe the $2\nu\beta\beta$ decay process for the first time [16] and a precision measurement of its half-life was made finding that $T_{1/2}^{2\nu} = 2.165 \pm 0.016(stat) \pm 0.059(syst) \times 10^{21}$ years [34]. This is the most precise half-life measurement for $2\nu\beta\beta$, and moreover, it is so far the slowest directly observed $\beta\beta$ process in nature.

As an upgrade to EXO-200, nEXO is searching for $0\nu\beta\beta$ decay in 5 tonnes of LXe [36]. The experiment plans to use LXe enriched to 90% in the isotope ^{136}Xe which $\beta\beta$ decays to ^{136}Ba as $^{136}\text{Xe} \rightarrow ^{136}\text{Ba} + 2e^- + n\bar{\nu}_e$, where n can be either 0 for neutrinoless double beta decay or 2 for two-neutrino double beta decay. A defining parameter for this research is the Q -value of the decay $Q[^{136}\text{Xe}] = 2458.07 \pm 0.31$ keV [37]. In $2\nu\beta\beta$ decay the total energy is split between the decay products, this is two electrons and two neutrinos. In this case, electrons would only carry one part of the total energy. The latter is represented with a continuous energy spectrum as in Figure 1.3(a). In the case of $0\nu\beta\beta$ decay, there are no neutrinos to carry away energy. This leads electrons in the final state to fully carry the energy corresponding to the Q -value of the decay. This is the reason why $0\nu\beta\beta$ decay is represented by a sharp peak at exactly the Q -value previously mentioned and shown in Figure 1.3(b).

A schematic of the nEXO design is shown in Figure 1.5. nEXO is a single phase Time Projection Chamber (TPC) where a static electric field drifts ionization charge to a segmented anode while scintillation light is being detected by silicon photomultipliers (photo-detectors also known as SiPMs). It will contain 5000 kg of liquid xenon inside its TPC. Because of the big drift length of the TPC, electron lifetimes longer than 10 ms are required [36]. Outside the TPC, there will be an inner cryostat full of refrigerant, keeping the Xe in liquid

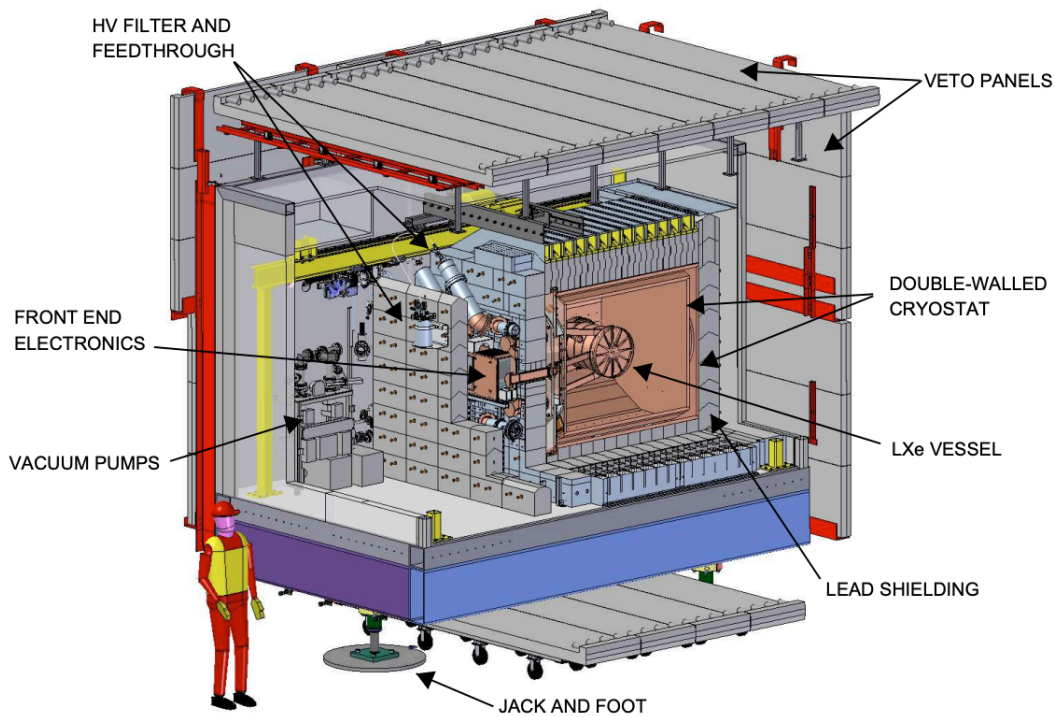


Figure 1.4: Artist's view of EXO-200, an experiment which searched for $0\nu\beta\beta$ decay with 175 kg of liquid Xenon enriched to 80.6% in the isotope ^{136}Xe . The detector was located inside a class 1000 clean room at a depth of 1050 m water equivalent [35] in New Mexico. The main component of the detector was a LXe time projection chamber (TPC) at 168 K, inside a double-walled copper cryostat, a lead shielding and a muon veto. The inner cryostat contained an ultra-clean fluid to shield against background radiation and to keep the Xe liquid. The front end electronics were located outside of the 25 cm-thickness lead for the simplicity and accessibility of room temperature electronics. Finally, a cosmic-ray veto counter surrounded the cleanroom in which the detector was placed. Picture obtained from [16].

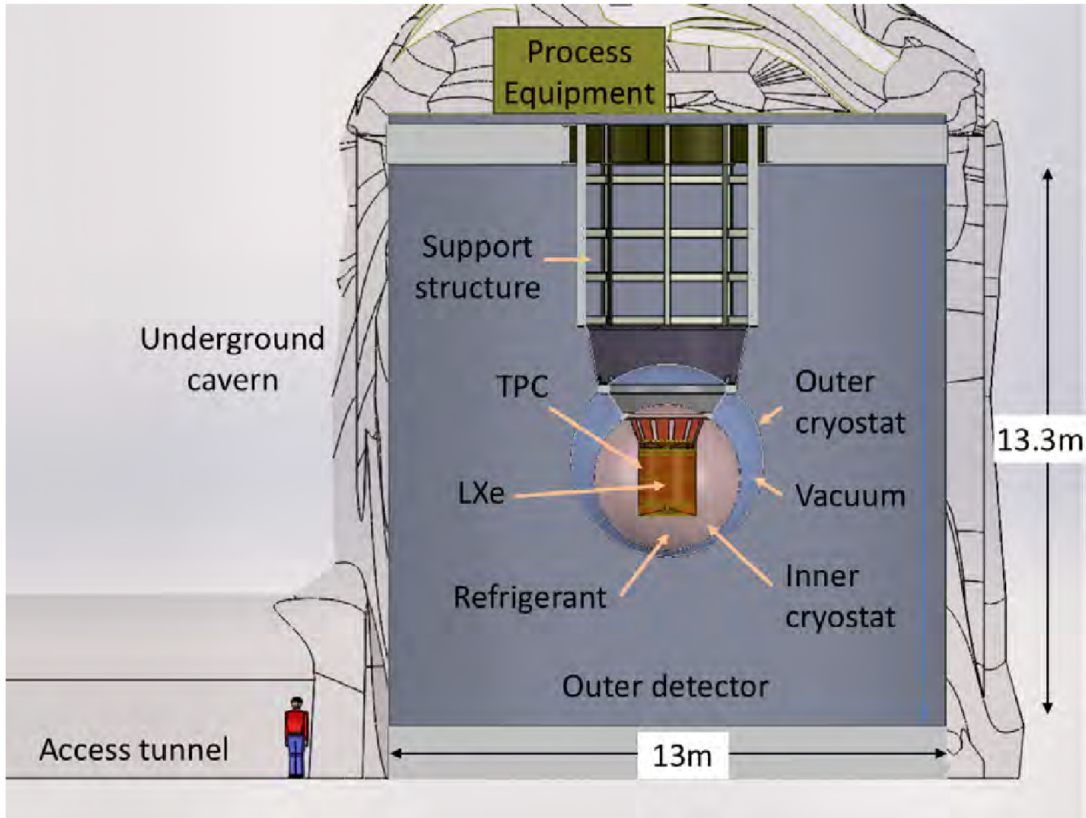


Figure 1.5: Artist's view of the nEXO experiment which is expected to operate almost two kilometers underground at SNOLAB in Ontario, Canada. The key elements are displayed: The TPC full of LXe contained in the inner cryostat, which at the same time is contained in the outer cryostat, and the outer detector to shield against external radiation. Picture obtained from [36].

phase at nearly 168 K. The outer cryostat encloses the system, providing an insulating vacuum environment. Finally, the 13m-diameter outer detector filled with water [36] shields from γ backgrounds and acts as a muons veto. nEXO's projected half-life sensitivity is approximately 10^{28} years [38].

1.5 The Ba-tagging technique as an upgrade path to nEXO

Despite its size, nEXO's sensitivity will be limited by backgrounds. Radioactive isotopes such as ^{222}Rn have a steady-state presence in LXe, long-lived radionuclides from the ma-

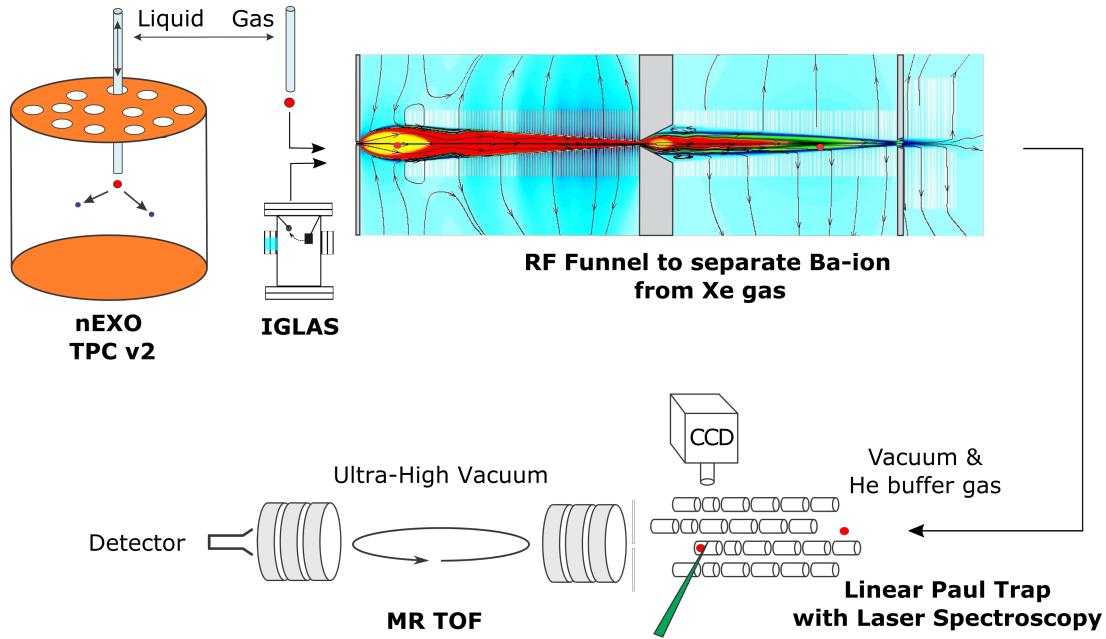


Figure 1.6: Schematic of extraction and identification process. When a candidate event is identified in the TPC, it is extracted from the LXe and transferred into a GXe environment. As the ion passes through the RF funnel, the system will reduce the pressure until the Xe gas is mostly pumped out. Lastly, the ion is captured in the LPT and MR-TOF for further identification. Figure modified from K. Murray private communication.

materials of the detector emit gamma and beta radiation that ionizes Xe and underground cosmogenic activation products in LXe, produce large signals in the detector. Results from EXO-200 indicate that then-activated Xe isotope ^{137}Xe is another important background in searching for $0\nu\beta\beta$ decay [35]. Because of this situation, the nEXO collaboration is working on the development of the so-called *Barium tagging technique* [39]. The goal is to discriminate against backgrounds by identifying true $\beta\beta$ events by "tagging" the Ba ion daughter to confirm real ^{136}Xe decay events [40]. However, the Ba-tagging technique does not reject $2\nu\beta\beta$ events. These are discriminated by the Q-value of the event shown on the energy spectrum, which is also limited by the energy resolution of nEXO ($\leq 1.0\%$) [36].

A more detailed scheme of a proposed Ba-tagging technique which is being pursued by collaborators at TRIUMF, McGill, and Carleton University, is shown in Figure 1.6. If a

potential $0\nu\beta\beta$ event is observed, then a ^{136}Xe sample in its liquid phase is extracted with the ^{136}Ba ion contained in it. After a phase transition, a Radio-Frequency (RF) funnel [41] transfers the Ba ion from high pressure gaseous xenon to vacuum for ion trapping and individual identification of barium-136. The particle is subsequently trapped by a Linear Paul Trap (LPT) and identified by laser spectroscopy in vacuum [42]. The final stage of the technique allows $^{136}\text{Ba}^+$ to go through a Multi-Reflection Time of Flight (MR-TOF) Mass Spectrometer to provide mass confirmation and a way to systematically study the extraction process.

Particularly, this thesis focuses on the development of an in-gas Laser Ablation Source (IGLAS) to study the extraction process. The anticipated future location of IGLAS in the Ba-tagging scheme is shown in Figure 1.6.

Chapter 2

Laser ablation

Laser ablation occurs when a sufficiently powerful laser interacts with the surface of a given material. With the laser energy, the surface temperature increases until reaching a value above its vaporization temperature through single-photon and multi-photon absorption as well as dielectric breakdown [43]. This results in evaporation and melt expulsion interaction processes, leading to significant material removal.

The resulting ejected material is a mix of neutral atoms and ions. The ion density n_i and the electron density n_e , the ablation volume, and the penetration depth are functions of several parameters. The laser repetition rate, the beam spot size, the pulse duration, the laser energy, and the laser wavelength (with increasing photon energy, an increase in the number of produced ions is observed [44]) play crucial roles in the ablation process and affect how ions are created.

2.1 Laser Ablation Sources

A laser ablation source (LAS) is a functional source of highly concentrated energy. This makes it an extremely useful instrument in many fields of science and technology. For instance, a LAS can be used in surgical procedures in medicine, manufacturing in industry,

and research.

For this work, a LAS has been developed as an ion source for studying the production and interaction of ions in environmental conditions similar to those in nEXO. This work has been undertaken as part of the Ba-tagging development which is being pursued as a future upgrade path for nEXO. The LAS has been developed to study the extraction process in Ba-tagging.

2.1.1 General working principle of an ion source

For ion sources (and plasma-generator instruments in general), the approach used to produce ions defines energy range of the source and subsequently, the charge states [45] and its operation purpose. The ionization of the sample can be done through *surface ionization* by being in contact with a high temperature surface; *photoionization*, a high power laser interacting with a background gas; *electron impact ionization*, electrons colliding with gas particles, and *field ionization*, very intense electric field emissions. The different ion sources commonly are named based on the way ions are formed, for example, *field emission ion sources*, *electron beam ion source* and for this work, *laser ablation ion source*. Much of the laser ablation process depends on the setup configuration. For instance, operating a laser with shorter wavelength, leads to higher photon energy, being more suitable for efficient vaporization and ionization of a solid sample [46], ideal for thin film deposition or ion production. Common laser ablation studies are performed on materials such as C, Al, Au, Ag, Cu, Fe, and Zn [47] with Q-switched Nd:YAG lasers in vacuum or in low pressure environments.

2.1.2 Basic power requirements and optical considerations

The intrinsic absorption coefficients of the target material and the pressure of the surrounding gas in which the experiment is being developed, will decide the experimental parameters such as the beam wavelength, intensity and voltages to be set. For instance, if

the wavelength is not adequate, the target could stop absorbing the incoming energy and consequently plasma production could stop. A study [46] suggest that with decreasing laser wavelength an increase in the ablation rate is expected. In the same way, an abnormal distribution in the laser beam profile leads to an angular energy distribution in the laser plume [48].

Nd:YAG laser systems are typically employed in LAS systems because the divergence of the laser beam is considered to be small and they require minimum maintenance. Moreover, these lasers offer a broad range of wavelengths. The fundamental wavelength for a Nd:YAG is found in the near-infrared at 1064 nm. Harmonics can also be obtained to generate wavelengths at 532 nm, 355 nm, 266 nm, and 213 nm.

Figure 2.1 shows how the laser pulse fluence will affect the plasma and the ablation depth per pulse on the surface induced by laser ablation. In this plot, short pulses are represented by empty dots and long pulses are represented by filled dots. The continuous curves are two different fits represented by Equations 2.1 and 2.2, respectively. These Equations calculate the ablation depth ΔZ_v through the laser fluence F_L , the threshold laser fluence for vaporization F_{th} , the latent heat of evaporation per unit volume ρLv and surface absorbance of the target A ,

$$\Delta Z_v \approx \alpha^{-1} \ln\left(\frac{F_L}{F_{th}}\right), \quad (2.1)$$

$$\Delta Z_v \approx A\left(\frac{F_L - F_{th}}{\rho Lv}\right). \quad (2.2)$$

The difference in the laser pulse fluence values will result in a change on the beam profile $P(\tau)$ which in most cases is approximated by a Gaussian distribution of the form

$$P(\tau) \approx \frac{1}{j\sqrt{2\pi}} \exp \frac{-\tau^2}{2j^2}, \quad (2.3)$$

where j is the pulse length and τ is the pulse width of the beam.

Furthermore, to achieve the production of ions through laser ablation, the duration of the pulse must be on the order of nanoseconds (ns) or less. For pulse times longer than that, vaporization would be the main mechanism for material expulsion [49].

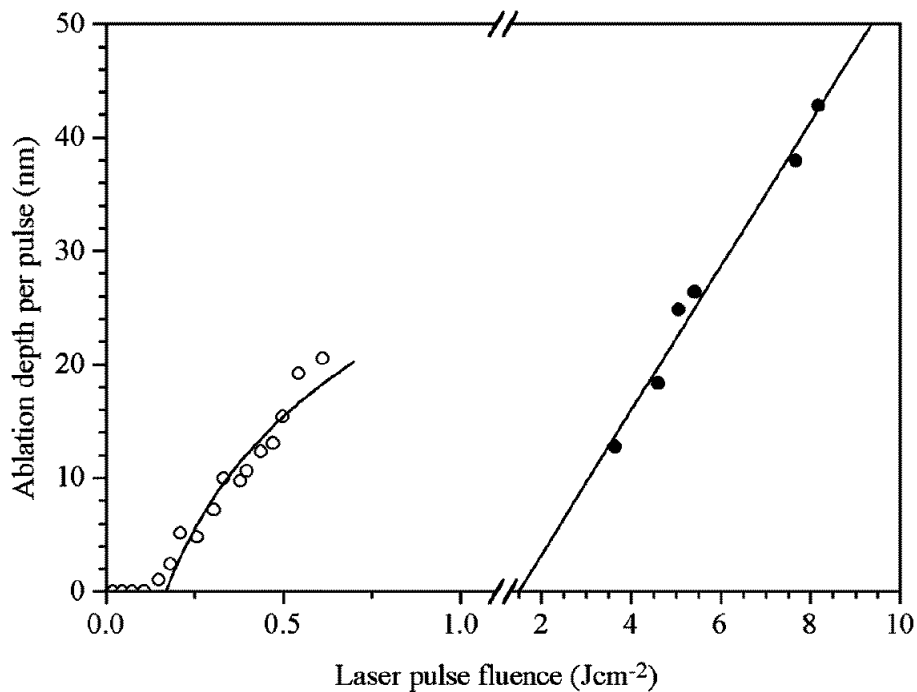


Figure 2.1: Ablation depth per pulse as function of the laser pulse fluence for 248 nm laser ablation of copper in vacuum. Empty dots represent data obtained from a 0.5 ps laser pulse and filled dots from a 20 ns pulse. Both data sets have been fitted for visibility of the reader. The continuous curves are two different fits represented by Equations 2.1 and 2.2, respectively. Image retrieved from [50].

On the other hand, for pulsed laser ablation to happen, the laser irradiance (power density per unit area) must be on the order of 1 GW/cm^2 or above [49]. The beam absorption in the plasma affects the ablation process since it cuts down the laser irradiance reaching the target, and it also heats of the plasma. The presence of a plano-convex lens (an optical component which focuses light in a specific spot) within the LAS is essential to achieve maximum focusing on the target's surface. One can use

$$2\omega_0 = \left(\frac{4\lambda}{\pi}\right)\left(\frac{F}{D}\right), \quad (2.4)$$

to calculate the spot diameter by finding twice the value of the beam waist (ω_0) knowing the focal length F of the lens, the wavelength λ of the laser and the diameter D of the beam entering at the lens. A schematic of the focusing process is found in Figure 2.2. From this result, it is possible to obtain parameters such as the laser irradiance, laser fluence (the amount of energy applied per area unit) and the laser spot size on the target.

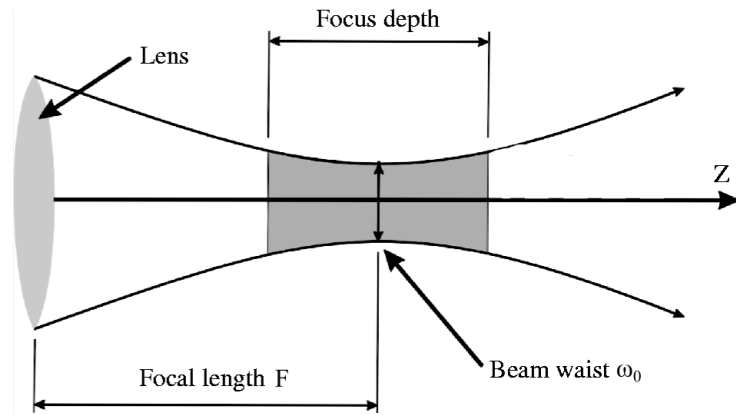


Figure 2.2: The beam waist denoted by ω_0 will find its minimum value when the lens is positioned at a distance from the target equivalent to its focal length F . Likewise, the focus depth is the distance range that the target can be placed in front of the lens and get ablation over the surface. Image retrieved from [51].

The expansion dynamics of the evaporated plasma is a function of the background gas. If the ion plume is found in a gaseous environment, it is important to consider that the gas

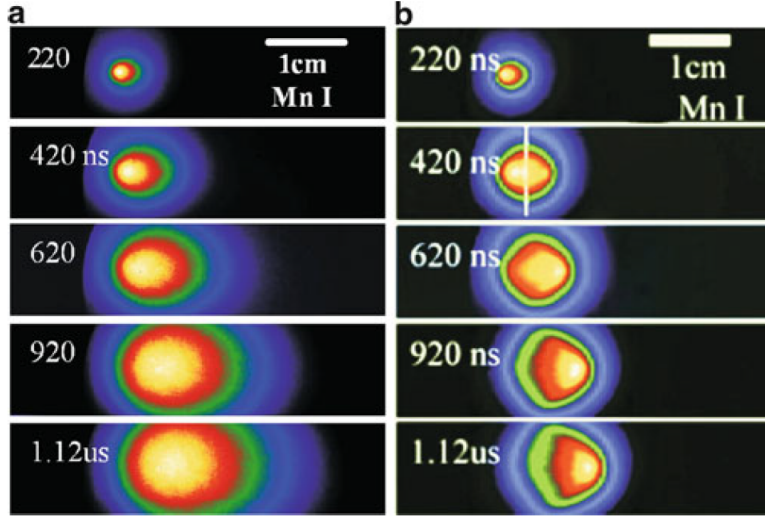


Figure 2.3: The evolution of a manganese plasma plume under a) vacuum and b) 20 Pa of oxygen. It can be seen how the plume is squeezed in the presence of a background gas. Image retrieved from [46].

pressure will compress the plasma (its expansion pushes gas particles away, compressing them and the plasma plume back). For pressures >10 Pa, the background gas particles alter the plume dynamics as shown in Figure 2.3. When the mean free path of the plume gets reduced, a shock wave is formed [46] and the plume pressure becomes equal to the background gas pressure. According to [46] the plume mass can be determined as

$$M_p \approx \frac{2}{3}\pi R_{SW}^3 \rho_{gas}, \quad (2.5)$$

where ρ_{gas} is the density of the gas and R_{SW} is the radius of the shock wave.

The influence of plasma shielding by the background gas becomes more important for high irradiance values since the background gas will start to get ionized considerably [52]. High photon energies, produced by short wavelengths, lead to more efficient vaporization/ionization of a solid sample [46]. The thresholds for target melting and vaporization and for plasma formation in the Cu plume are almost unaffected by the background gas used, but the threshold for plasma formation in the background gas is determined by the ionization potential of the gas which will be discussed later.

2.1.3 Ion ejection and plasma plume

When a laser beam with the previously mentioned characteristics hits the target of study, a group of electrically charged and neutral particles coming from the material's surface is ejected as a consequence of the laser-matter interaction. The net charge of these particles converts the ejection of ions into a plasma. The resulting plasma is known as *ablation plume* and within it, the positively charged ions are identified as the most energetic particles [53]. A complete description of the ablation process and the plume expansion is not trivial. The dynamics of these events involve extensive studies on time-dependant thermodynamic and hydrodynamic phenomena based on statistical parameters. However, the plume characteristics can be extracted with assumptions and approximations. For instance, most plasmas created in the laboratory have ion density values (n_i) that range from $n_i = 10^{10}$ to $n_i = 10^{14}$ particles per cm^3 [54]. It is also known that as more laser pulses are incident on the target, the diameter of the ablation zone widens up. Likewise, as the depth of the ablated crater increases, the expulsion of melt becomes less efficient, leading to partially close the groove and to create a pronounced and noticeable melt rim around the crater. In metallic targets, craters can be drilled in the low fluence regime ($>1 \text{ J/cm}^2$) due to the absence of thermal losses [48]. If no interaction affects the plume particles (this could be interpreted as other particles travelling in-vacuum or under the effects of a magnetic or electric field), then the result will be a plasma emitted as a cone mostly concentrated perpendicular to the target surface. If the ablation process is taking place in a gaseous environment, collisions with the gas atoms are expected to slow down the plume particles and eventually stopping them. For this work, the beam-target interaction will usually happen in a controlled gaseous Argon (GAr) or gaseous Xenon (GXe) environment. The collision cross section σ_c can be calculated from the Van der Waals radius of the target material particles (r_s) and the radius of the particles in the background gas (r_g) through

$$\sigma_c = \pi(r_g + r_s)^2. \quad (2.6)$$

These values typically range between 100 pm and 200 pm. Studies [55] have shown that the plume shape, velocity, energy distribution of density after the first laser pulse, the spatial variation of its composition in terms of its conforming species (ions, molecules and excited states) [56], and laser parameters such as the fluence and energy profile distribution, represent crucial information for the understanding of the dynamics of the ion plume expansion process.

2.2 Applications of LAS for Ba-tagging

The goal of this work is to get a better understanding of ion transport in-vacuum and in-Xe-gas. Two experimental LAS sources are available in the laboratory: I) an In-Vacuum LAS and II) an In-Gas LAS that can be operated in-vacuum or in-gas. The latter ion source is the thesis. A schematic of both ion sources are shown in Figure 2.4.

2.2.1 In vacuum LAS

The vacuum chamber has been designed to study ion optics in a vacuum environment and it is coupled to other analysis systems. When attached to as a mass spectrometer, the advantages of building a setup as the LAS are abundant. In fact, future plans for the in-vacuum LAS at McGill include using it as an ion source for a Multi-Reflection Time-of-Flight Mass Spectrometer (MR-TOF). This instrument will allow the MR-TOF to obtain high precision mass measurements and to minimize the spatial charge effects for a constant particle density of the beam [57]. For this work, measurements previously done in vacuum have been taken as a reference for further in-gas measurements.

2.2.2 In-gas LAS

The production of ions through laser ablation sources is also carried out in gaseous environments for specific purposes. For instance, a laser ablation ion source was implemented as part of the Low Energy Beam and Ion Trap (LEBIT) experiment to make precise studies of rare isotopes [58]. Additionally, laser ion sources are promising for providing heavy ion beams at accelerators [59]. However, the study and proper development of in-gas laser ablation ion sources represents a big challenge due to the loss of energy caused by the ions and background particle interactions.

Essential information about the interaction of ions with the background gas comes mainly from the ejected plasma. An In-Gas Laser Ablation Source system (IGLAS) is used to create and extract ions from a sample target in vacuum, GAr, or GXe environment. The inherent complexity introduced by the background gas combined with the interaction of the ablated particles can result in various processes which include clustering, deceleration, plume oscillations, shock wave formation, thermalization, and plume splitting [47]. All these mechanisms are laser and background gas dependant. They must be included in the study of Ba ions transport from LXe to GXe, as in nEXO.

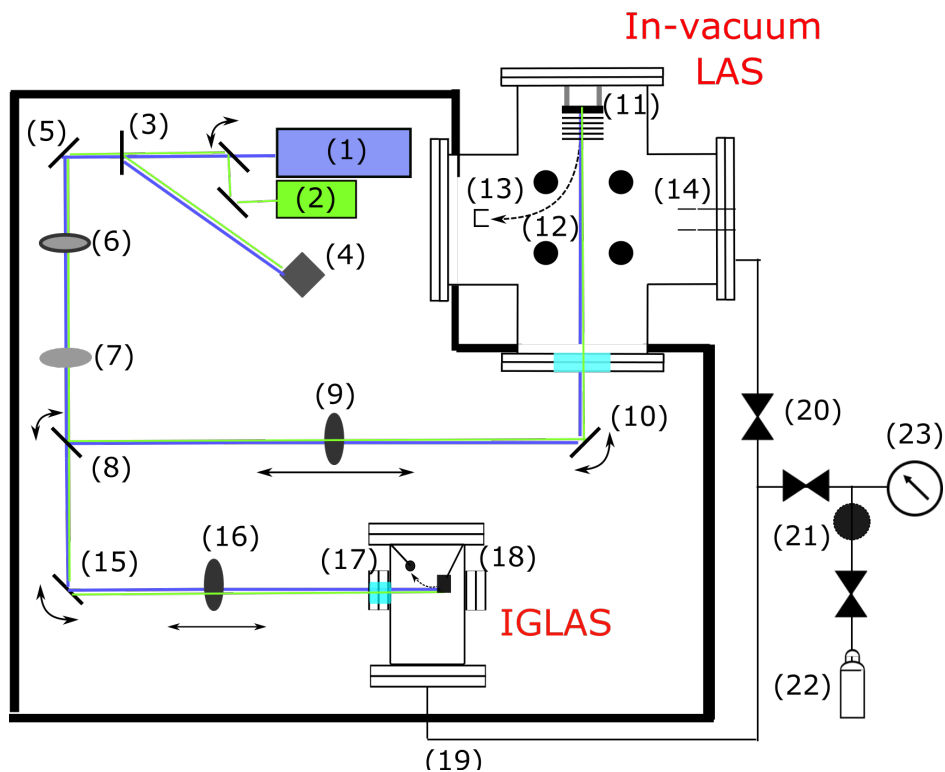


Figure 2.4: Schematic of the McGill Laser Ablation Sources, from a top view. The IGLAS gas line (19) can be seen at the right, outside the enclosed setup. This line is currently connected to an Ar-gas cylinder (22). More information about this setup will be discussed in section 3.2.

Specific research objectives in the application of a IGLAS for Ba-tagging are: (I) characterize the ablation process using various targets in the pressure chamber, i.e., measuring the ion current as a function of the target composition, laser power and lens position, (II) measure the ion extraction efficiency, and (III) determine the influence of Xe-gas flow and pressure on the extraction process.

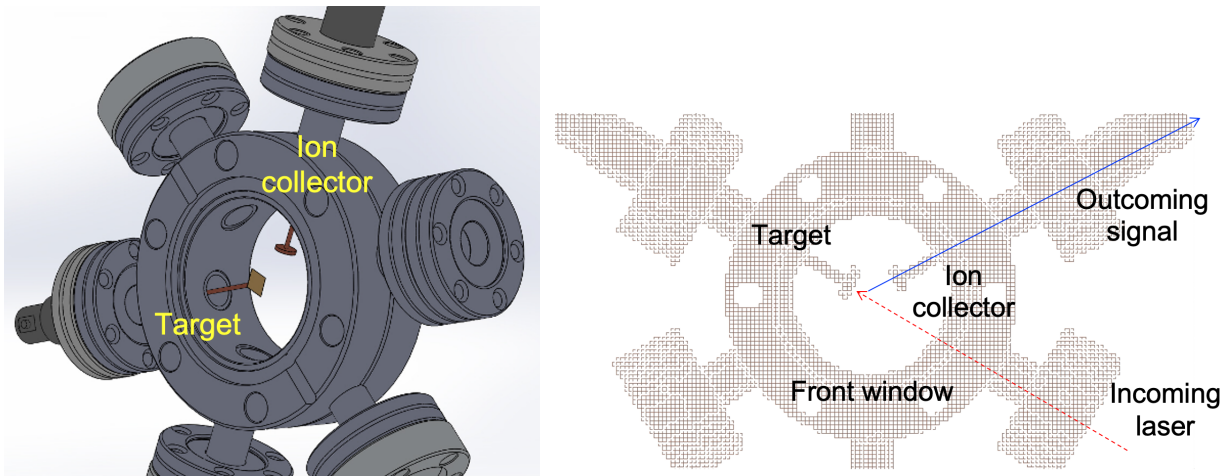
Chapter 3

Methodology and setup

3.1 Simulation

Simulations were carried out to investigate different target and ion collector geometries and to get a basic understanding of ion drift in the presence of a background gas. For this SIMION was used, a simulation software for ion and electron optics. It allows the user to create complex geometries and to assign values for key parameters such as applied potentials, kinetic energy of ions and physical properties of the flying particles. Additionally, in order to reproduce more realistic conditions, SIMION has implemented the *HS1 collision model* [60]. This simulates a background gas by following the hard-sphere collision model and setting the proper parameters such as the gas particle mass, radius, axial velocity, pressure, and cross section of the interacting particles. Through these parameters it is possible to calculate the ion drift velocity and to display the trajectory followed by the travelling ions.

Au and Cu ion trajectories have been simulated (since only these materials would be later analyzed for this work) in Ar and Xe as the background gas. The simulated setup is displayed in Figure 3.1 which represents the IGLAS source geometry. An engineering rendering of the source is shown in Figure 3.1(a). The model was exported from Solid-



(a) SolidWorks 3D rendering of the pressure chamber. (b) Rendering of the set up in the SIMION work bench.

Figure 3.1: An schematic of the IGLAS source geometry. A STL design was created in (a) SolidWorks and then (b) imported to SIMION to study ion transport properties. The square golden piece is the target and the round copper disk is the ion collector plate. A bias can be applied to both the target and the ion collector.

Works in the STL file format and imported into SIMION. The rendering of the STL file in SIMION is shown in Figure 3.1(b). The target, represented by the square golden piece is located in a direction such as the laser beam hits it perpendicular. The copper disk shown at the upper right side is the ion collector plate. The source geometry files were imported as an .STL file obtained from the SolidWorks design of the pressure chamber. The applied bias for each simulation varied initially from 0 V to 50 V for the ion collector electrode and from 0 V to -20 V for the target electrode. Since the goal is to operate the IGLAS system, simulations were performed to study ion drift in gas for the presented electrostatic geometry. Simulations ran up to the threshold value of 10^5 Pa. For high pressure values running times increased considerably and there was little difference among the resulting field lines. A more detailed explanation for the simulation results will be discussed in the following chapter. By defining detailed geometry and by adding the HS1 collision model to the main program, it was possible to replicate the gas environmental conditions up to 1 bar. In addition, since the SIMION workbench only allows to set one sample and

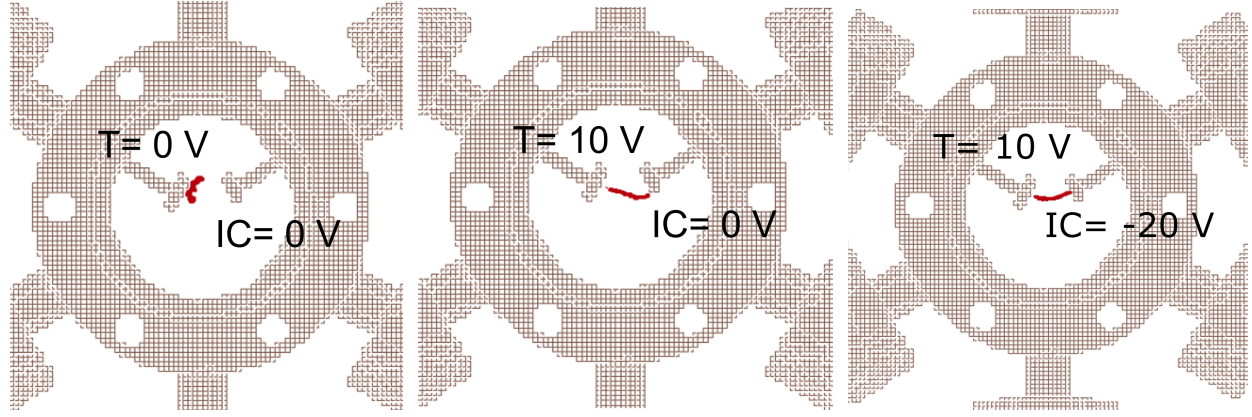
one background gas at a time, physical parameters used for these simulations changed as function of the elements. The collision cross section σ_c for each target-gas combination was calculated from the Van der Waals radius of the source particle (r_s) and the radius of the applied gas (r_g). The resulting values are listed in Table 3.1 along with other ion properties.

Parameter	Element	Value
Flying particles mass [61]	Cu	63.5 AMU
	Au	196 AMU
Van der Waals Radius [62]	Cu	238×10^{-12} m
	Au	245×10^{-12} m
	Ar	183×10^{-12} m
	Xe	206×10^{-12} m
Calculated collision cross section σ_c	Cu/Ar	5.5682×10^{-19} m ²
	Cu/Xe	6.1932×10^{-19} m ²
	Au/Ar	5.7549×10^{-19} m ²
	Au/Xe	6.3900×10^{-19} m ²

Table 3.1: Considered parameters for the SIMION simulations.

The collector plate and the target were marked as electrodes for these simulations and the software allows any positive or negative voltage to be set on them. The sample was set to fly 100 ions per simulation with a Gaussian distribution describing a kinetic energy spread of around 100 eV. This value was chosen based on previous in-vacuum studies of the energy distribution of ions produced by laser ablation of metallic materials [53]. The mean ion energy should be around this value [63]. The collision model is very crude and simulation times will become long for high pressures. The resulting trajectories are shown in Figure 3.2.

The ion production and the ion velocity are strongly dependant on the laser fluence and in many plasma processes, the electric field between the two electrodes defines the characteristics [64]. The ion velocity



(a) Target (T) and Ion Collector (IC) grounded. (b) Target biased at +10 V and Ion Collector grounded. (c) Target biased with +10 V and Ion Collector biased at -20 V.

Figure 3.2: Simulation results for Au ablation on a background Xe gas at 10^5 Pa of pressure. Even under these conditions, it is possible to attract ions to the collector plate when a bias is applied to both electrodes. (a) Ions hardly leave the sample surface if both electrodes are grounded, (b) ions drift to the ion collector, however they are not attracted and hardly reach the bottom end of the collector plate, and (c) the ion trajectory gets deflected by the applied potentials on the receptor electrode.

$$v = \sqrt{\frac{2E}{m}}, \quad (3.1)$$

in the absence of an acceleration potential has been calculated for kinetic energy E values between 0 - 100 eV. This was done in vacuum conditions for Au and Cu samples with mass m , Van der Waals radius r and calculated collision cross section σ_c as denoted in Table 3.1. The ion velocity calculated using Equation 3.1 and the ion masses listed in Table 3.1 are shown in Figure 3.3. For typical energies the ejected charged particles would travel 8 mm in $\sim 18 \mu s$ in this setup. This fast displacement represents a non-trivial challenge for capturing the growth process with a video camera, but it also provides an estimation of the observed energies coming from the laser source.

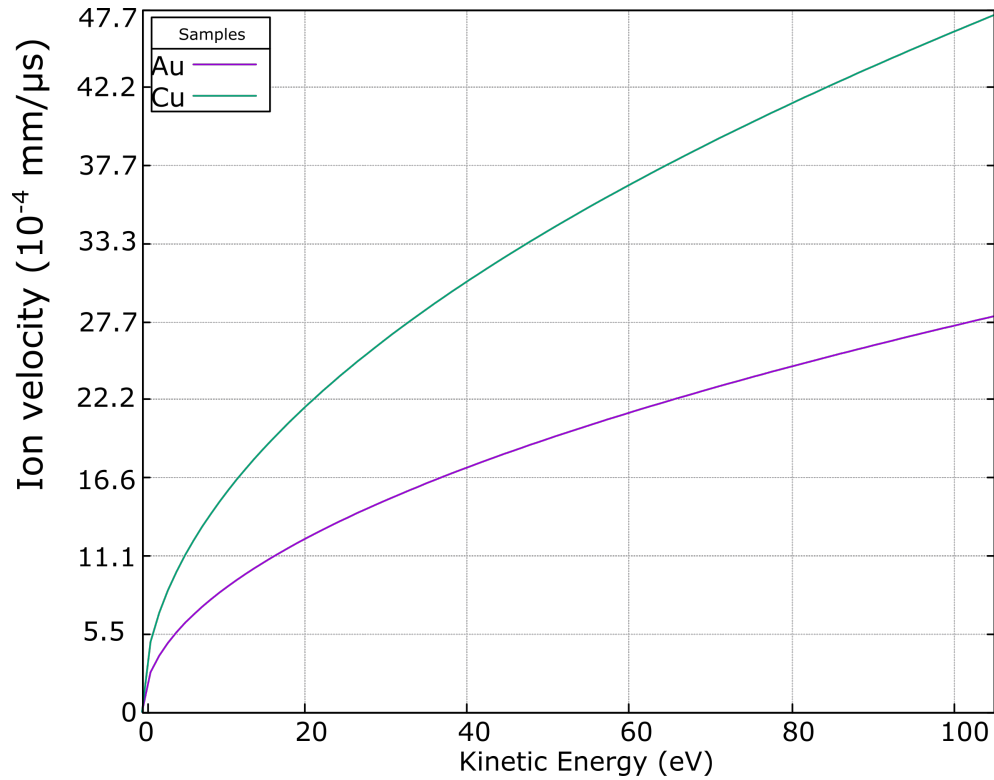


Figure 3.3: Expected Au and Cu ion drift velocity in vacuum as function of ion kinetic energy, expressed in electron-volts (eV).

3.2 The McGill LAS setup

The Laser Ablation Source (LAS) consists of a 349 nm Neodymium-doped Yttrium Aluminum Garnet Spectra-Physics Explorer (Nd:YAG) Ultra-Violet (UV) laser and a set of optical components which focus the beam causing ablation on a target. For user safety and protection, the whole LAS system is enclosed by poster-board and interlocked to prevent the laser from bouncing off within the laboratory. Additionally, all LAS optical elements have a high UV transmission for a low chance for photons to get absorbed or reflected by the optics material.

A detailed description of the optical components of the LAS following the numbering shown in Figure 3.4 is as follows:

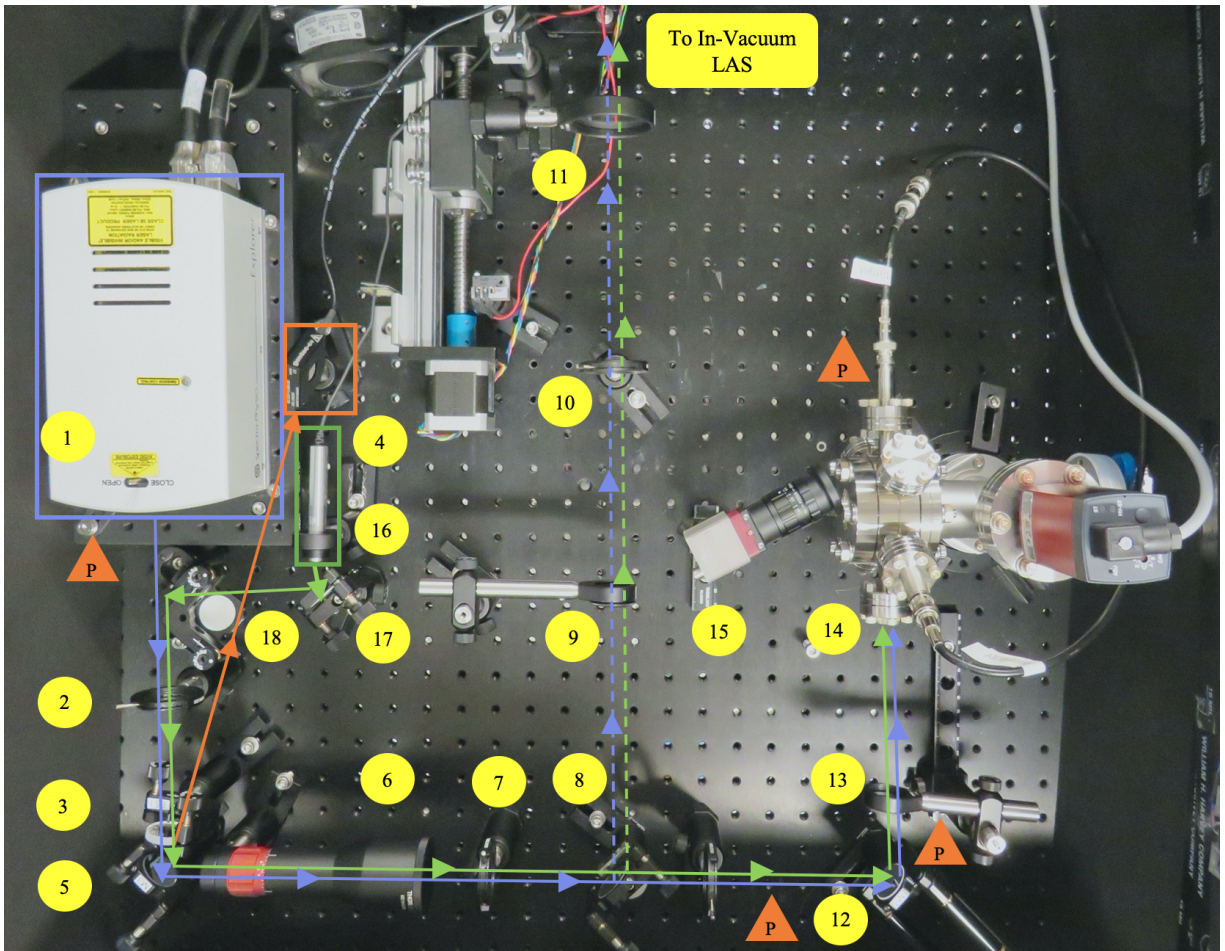


Figure 3.4: Picture of the McGill Laser Ablation Source. Optical paths^a are indicated by green and blue lines for 532 nm alignment laser and 349 nm UV laser, respectively. The dashed lines represent the optical trajectory towards the In-Vacuum LAS. The orange line represents the beam path after striking the beam splitter towards the power meter. The orange triangles represent the spots where the power meter was set to measure power and energy. Numbers in circles are optical elements described in more detail in the text.

^aSee Figure 1 in the Appendix section for a wider view.

1. The starting point of the LAS is the Spectra-Physics Explorer UV laser. This is a class 3B 349 nm-wavelength laser, connected via RS232 to the LAS computerized system for remote control.
2. The second component is a post-mountable iris aperture to define the optical axis by serving as a guide for the beam.

3. After the iris aperture, there is a Thorlabs BSF10-UV 1" Diameter beam splitter. Between 1% and 10% of the beam [65] depending on the polarization of the incident laser beam is reflected. This is used to reflect a fraction of the laser power on a power meter.
4. The Gentec QE12LP-S-MB-QED-D0 Pyroelectric detector enables laser energy measurement. An external monitor, allows the user to observe a real-time plot of the laser power.
5. A Thorlabs 1" Diameter, UV Enhanced Aluminum Mirror, 250-400 nm reflects the beam by 90°.
6. To achieve a significant laser ablation effect, the incoming beam size must be expanded and concentrated on a particular spot. For this, a Thorlabs BE10-UVB Fixed Magnification Beam Expander is located in position number six. ¹
7. A second iris aperture defines the optical axis.
8. A flip mirror directs the laser beam to either LAS or it is flipped out of the way to send the beam to the IGLAS. This is a Kinematic Mirror Mount with a 1" Diameter, UV Enhanced Aluminum Mirror, 250-400 nm. When raised up the beam follows the path towards the vacuum chamber ², and if flipped down the beam is directed towards the IGLAS.
9. A fluorescent alignment disk can be placed in the beam path to center the beam trajectory.
10. An iris aperture defines the optical axis along with (2) and (7).
11. A Thorlabs 2" Diameter, $f = 750$ mm, UVFS Plano-Convex Lens, AR-Coated focuses the beam onto the target inside the vacuum chamber (not shown in Figure 3.4).

¹For this work, this component was previously a set of defocusing and focusing lenses to expand and then focus the beam. The latter lens configuration has been changed prior to taking the photography in Figure 3.4

²Not shown in Figure 3.4.

12. After the kinematic mirror a Thorlabs 1" Diameter, UV Enhanced Aluminum Mirror, 250-400 nm mounted on a Thorlabs KS1-Z8 DC Motorized Ultra-Stable Kinematic 1" Mirror Mount bends the beam 90° counter clockwise. The kinematic stand moves the laser spot on the target surface allowing 2D scans.
13. To focus the UV beam onto the target surface, a Thorlabs 1" Diameter, $f=200$ mm, UVFS AR-Coated Plano-Convex Lens is placed before one of the port side windows of the pressure chamber. The shorter the focal length, the more focused the laser becomes. The study of in-gas ions ablation may require higher power densities in a gaseous environment than in a vacuum [66]. A Thorlabs 6" Dovetail Optical Rail allows the lens to be positioned and focus the beam on the target. The latter is crucial since no ions are created if the power density is too low.
14. The Pressure Chamber of the IGLAS. A more detailed description of this system is found later in this section.
15. A camera is located outside of the pressure chamber in front of the main view port. It allows one to capture images of visible phenomena occurring on the target inside the IGLAS.
16. A CPS532 Collimated Laser-Diode-Pumped DPSS Laser Module, 532 nm, 4.5 mW, Round Beam has been placed parallel to the UV laser for aligning optical components. The visible light allows easier beam alignment for the 349 nm laser.
17. A Thorlabs 1" Diameter, UV Enhanced Aluminum Mirror, 250-400 nm is located in front of the alignment laser, to direct the beam 90° counter clockwise.
18. Finally, a Kinematic Mirror Mount with a 1" Diameter, Broadband Dielectric Mirror, 400-750 nm directs the alignment beam onto the optical beam path.

3.2.1 In vacuum LAS

Initially, the UV laser beam optics were designed for in-vacuum studies of laser ablation with the LAS. There, the target is located in a CF8" six-way cross. Ablated ions are deflected -90° by a quadrupole bender towards a Faraday cup for current measurements or they can be deflected by 90° towards an ion detector. This in-vacuum LAS has been developed to provide ions for the calibration of a multi-reflection time-of-flight mass spectrometer. The in-vacuum LAS is described in detail in [Murray et al, LAS, in preparation for publication] and it is not part of this work. However, most of the optical UV optics setup is shared between LAS and the IGLAS. Figure 3.4 shows position and location of the IGLAS. The beam path towards the in-vacuum LAS is indicated with dashed lines, the source itself is outside of the picture.

3.2.2 In-gas Laser Ablation Source (IGLAS) setup

The IGLAS system consists of a stainless steel pressure chamber, designed to study creation and extraction of Ba ions under pressurized environmental conditions using GAR and GXe. The goal is to measure the ion current as a function of pressure, laser power, drift velocity (the velocity of individual ions acting under an electric field) and ion drift length (distance traveled by an ion with drift velocity in a period of time). It is an essential part for the development of the Ba-tagging technique. The system described here was initially designed by Y. Ito.

Pressure chamber geometry

The main body of the pressure chamber is represented in Figure 3.5. The front port is covered with a CF 2.75" pressure viewport (with high UV absorption) to allow observation inside the chamber. The central part of the setup is a double faced CF 2.75" flange with six CF 1.33" ports welded at angles of positions 0° , 60° , 120° , 180° , 240° , and 300° . In this configuration, the incoming laser beam enters the chamber through a CF 1.33"

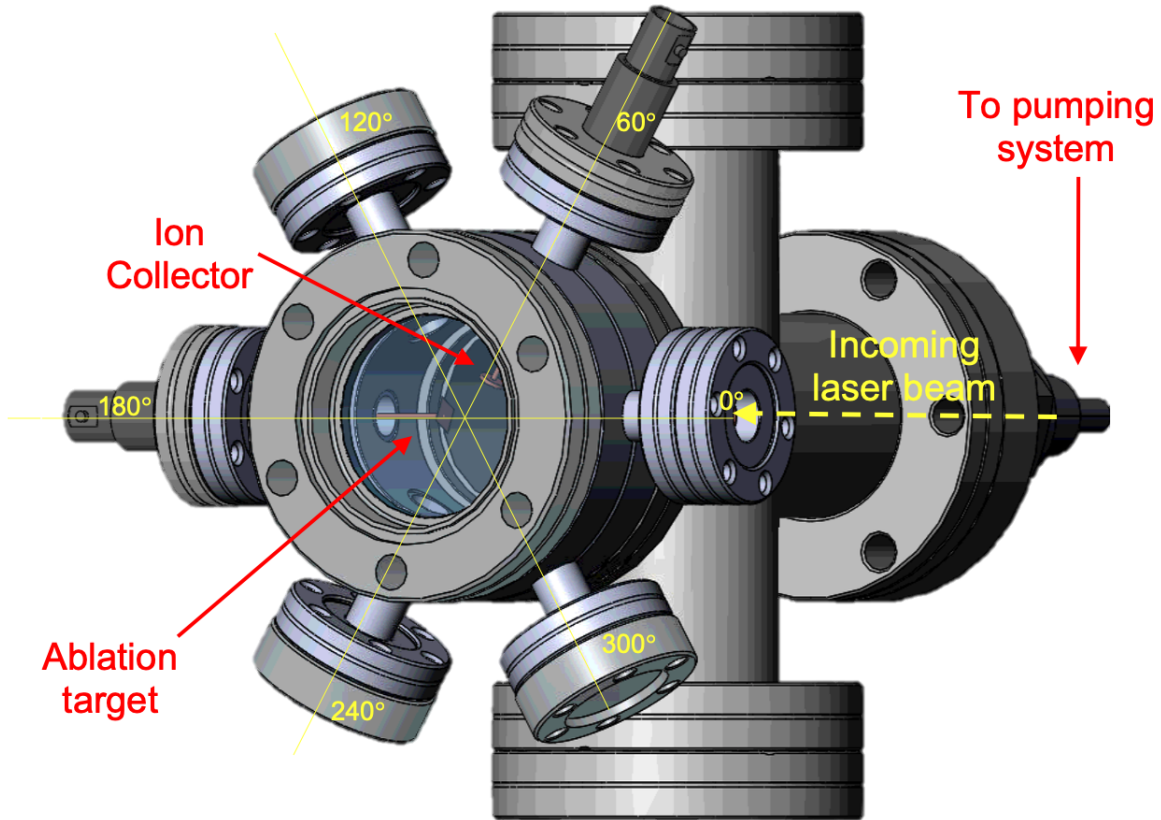


Figure 3.5: Engineering rendering of the IGLAS setup. The pressure chamber houses the target and ion collector, and it is designed to withstand pressures from vacuum to 10 bar.

pressure viewport from position 0 ° and impinges perpendicularly to the target. Two CF 1.33” rotatable SHV-5 kV feedthroughs hold the collector at 60 ° and the target is at 180 °. Both target and ion collector are soldered on a copper wire, directly connected to its correspondent SHV feedthrough. Each SHV terminal allows one to apply an external bias. The orientation between laser beam, target, and collector can be varied in multiples of 60°.

Ion current measurements were taken in-vacuum to characterize the system in absence of gas. For this, a 1/4” stainless steel pipe was installed on the back of the pressure chamber and connected to the LAS vacuum chamber ³. The IGLAS setup was securely bolted to the optical Table. A combined Pirani-Cold cathode full-range gauge reads the vacuum.

³See Figure 2 and 3 in the Appendix section.

The first values obtained from the pressure monitor were $P_1 = 3.23 \times 10^{-3}$ Torr using only a dry vacuum pump. To reach a higher vacuum, a turbomolecular pump was turned on. A couple of alcohol drops were sprinkled where gaps were thought to exist, looking for a fast increase on the pressure value. This was done to ensure the pressure chamber was hermetically closed. Finally, the whole system including the gas line was leak-checked with helium gas using an Oerlikon Leybold PhoenixL 300. At this point the system was ready to make the first ion current measurements.

Since it is not easy to see if the UV beam is striking the sample, a digital video camera was positioned in front of the CF 2.75" window avoiding obstruction of the UV beam trajectory. Other studies [67] discuss the advantages of using such a camera, and how this allows high resolution studies of the growing ablated plume.

Target holder and geometries

The tested targets inside the IGLAS were:

- A rectangular Cu bar with dimensions 9 mm x 3 mm x 2.5 mm.
- A small Cu disk of 5 mm in diameter and approximate thickness of 1 mm.
- A squared Au foil of 5 mm length per side.

These targets were soldered to a Cu wire and secured by a push-on connector to the 1.33" CF flange as shown in Figure 3.6. A power supply allows one to define the strength and direction of the electric field between the target and the collector. The target was biased using an analog power source with a limit voltage of 100 V. A negative voltage could also be applied through a Rohde & Schwartz NGC100 Power Source with a maximum operating voltage of 30 V. To prevent accidental electric shorts with the vacuum chamber ground it was necessary to wrap the target with kapton tape.



Figure 3.6: Image of the rectangular Cu sample attached to the CF 1.33" feedthrough flange. Dimensions of the Cu holder and the target itself are shown in red.

A fluorescent card was used to align the UV laser. The beam is directed towards the target by passing through the optical elements prior to the pressure chamber. After the alignment, the power and the energy emitted by both, the 532 nm and the UV laser, were measured. These measurements were executed at 4 different positions: right after the laser aperture, before (11), between (12) and (13) in Figure 3.4, and after the pressure chamber once the UV beam left the second port with no target installed. These tests were carried out by adjusting the UV laser power to 40%, 60%, 80% and 100% of its full capacity and measured with the power meter.

The actuators of the motorized mirror (12) in Figure 3.4 are manipulated remotely using Kinesis, a Thorlabs software, that allows the user to tilt the mirror in the x- or y-direction between 0 mm and 12 mm, with a minimum repeatable incremental movement of 0.2 μm^4 .

DAQ system

A *LAS in-Xe gas monitor* control LabVIEW VI has been developed to control all measurement parameters. A screenshot of the monitor is shown in Figure 3.7. The monitor simultaneously reads, calculates statistical parameters, and generates plots of the signals

⁴Important: This distance represents the displacement of the mirror. To find the distance the beam travels on the target's surface, it is necessary to find a conversion factor to translate from mirror coordinates to target coordinates.

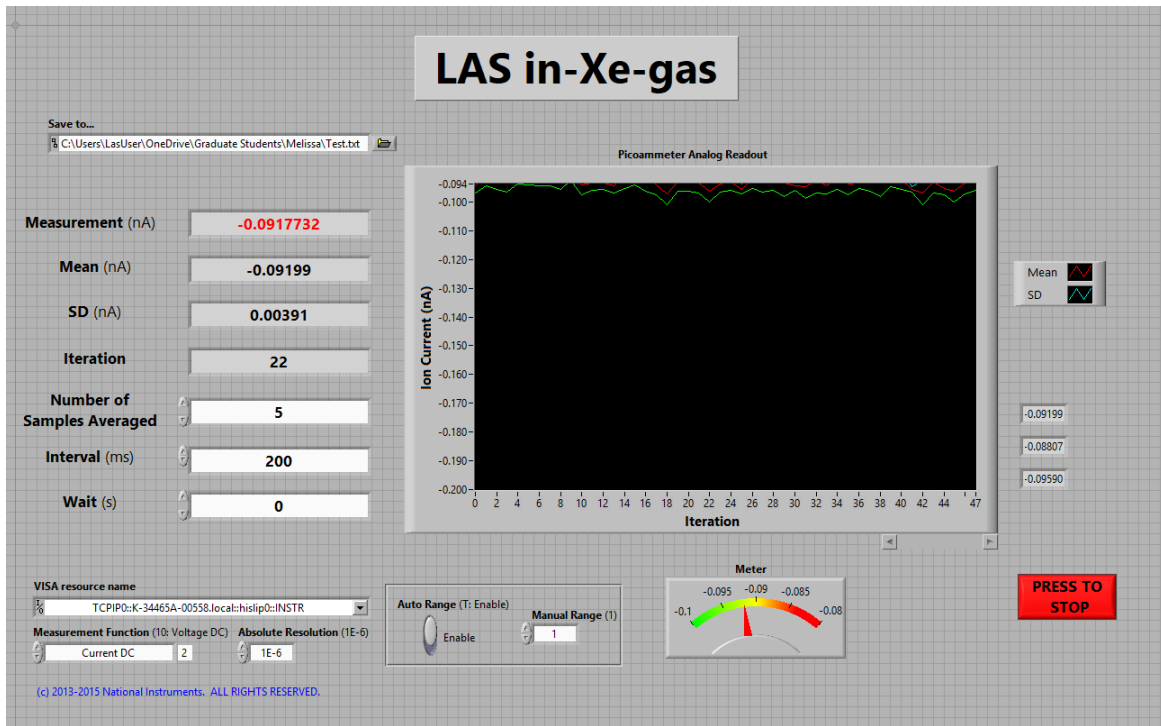


Figure 3.7: Screenshot of the LAS in-Xe-gas monitor. This LabVIEW VI reads the measured ion current from the collector plate and the target electrode, the laser power meter, the position controller, and it also sets the electrode biases.

obtained by the data acquisition systems (power and current meters). This VI is based on a monitor program developed by former students for the vacuum system LAS with which only the values corresponding to the measured current and statistical parameters can be obtained. The monitor program has been adapted by the author of this work for the specific needs of this project. Since it was expected to measure current values on the order of nanoAmperes (nA), a series of initial ion current measurements were executed using a Keysight 34465A picoammeter. These measurements are described in section 4.2.

Chapter 4

Measurements

Systematic studies were performed with the IGLAS setup at McGill to study ion production and extraction in vacuum and in-gas environments. This knowledge is thought to be later applied on the Ba extraction process for the development of the Ba-tagging technique. For the current work, however, only the study of ion production using the IGLAS setup has been executed and only in vacuum.

In this chapter, the results of several measurements to study the ion current response of Cu and Au targets as well as measurements related to possible sources of errors will be discussed.

4.1 Beam spot size measurements

Dimensional measurements of the laser spot size on the target are relevant to interpret future results. Focusing the UV laser beam down as much as possible leads to sufficient energy density and consequently to laser ablation. Different methods were applied to determine the diameter of the beam spot. These consisted of laser ablation on the surface of a paper, a Cu, and an Al sample. Since no ablation marks were observed for the Al target under the studied conditions, its analysis will stay out of the scope of this work.

The experimentally obtained values were later compared to a calculation from Gaussian optics and it will be discussed in the following section.

4.1.1 Beam spot determination through superficial ablation marks

The focused laser beam will create a small crater upon impact on the surface resulting from the melting process of the material. For this experiment, the position of the beam spot was fixed at all times. The laser power was measured by positioning the power meter right before (14) in Figure 3.4. The mean readings for various laser power values at a repetition rate of 1kHz are shown in Table 4.1. After measuring the power, the sample was placed on an optical mount at the same position.

Laser %	Average power (mW)
40	0.7 ± 0.1
60	9.1 ± 0.3
80	22.0 ± 0.7
100	32.8 ± 0.1

Table 4.1: Laser percentage value and its correspondent average power equivalence measured prior the pressure chamber.

Copper target exposure

The copper sample shown in Figure 4.1 was exposed multiple times to different laser energies from 60% to 100% for a duration of 5, 10, and 20 minutes. After 10 minutes of laser ablation at 1000 Hz, the circular-shaped copper target displayed a visible hole on its surface. The Cu samples were later analyzed to find the dimensions of the ablation marks. Although these marks were big enough to be visible to the naked eye, it was not possible to provide an estimation of their sizes by using simple measuring tools such as a measuring tape or a vernier scale. Instead, these samples were analyzed under an optical microscope linked to Toupview (a microscope camera control and image processing software) and compared to a CD stamper with known industrial standard dimensions, as

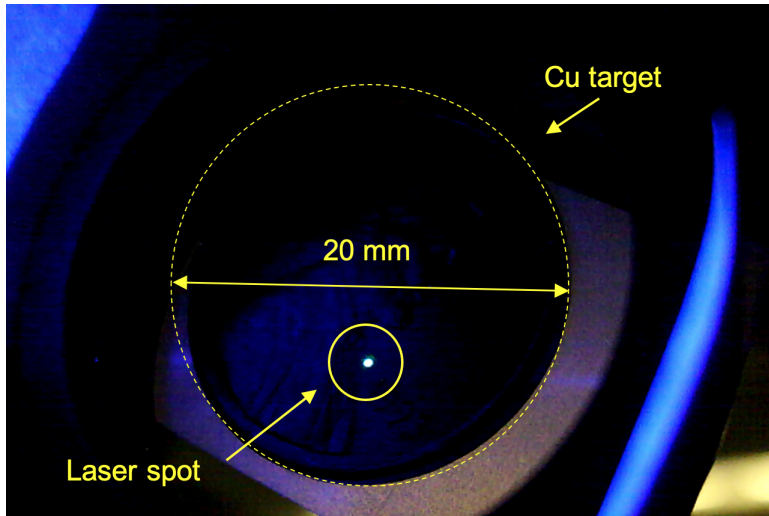


Figure 4.1: Circular-shaped copper target during the laser beam focusing process. The UV beam spot is visible at the bottom of its surface.

shown in Figure 4.2. Figure 4.2(a) was obtained by applying a 100x zoom on the microscope to the sample. The remaining images were taken with only 20x zoom. In order to compensate for the difference between the results, a scaling factor of 5 was included in the calculation of the beam diameter for the 20x zoomed images.

Longer exposure times increased the drill hole depth. The expulsion of melt became less efficient, reaching the point of partially re-enclosing the hole. This generate a pronounced rim from the melted material accumulated outside the crater. Because of the observed rim, for each measurement the inner and outer diameter of the rim was identified and their correspondent circumferences were measured as shown in Figure 4.2(d). For each circle, four diagonals were traced in order to find a proper estimation of the inner and outer diameters. These values were later averaged to find an intermediate value to estimate the size of the ablation mark if no melting rim was produced. The standard error was obtained from the standard deviation of the inner diameter and the outer diameter. The resulting values are shown in Table 4.2.

Paper target exposure

To ensure the previous results were reproducible for other materials, a thin piece of paper was used as a sample for a 2-minute long ablation process at 1000 Hz and beam laser

power from 60% to 100%. In the same way, the resulting marks were analyzed under an optical microscope. For each measurement, four diagonals representing the resulting marks were traced, measured and averaged to find the mean value of the focused beam spot size. The error value was obtained by taking the variance of these values. The diameter of the crater on each sample is shown in Table 4.2.

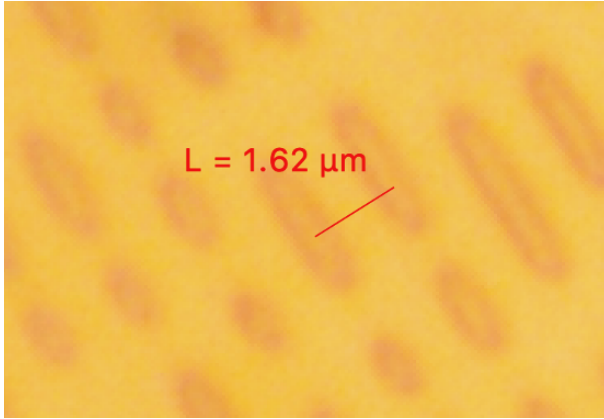
4.1.2 Beam spot determination through Gaussian optics

To find the expected beam spot size through Gaussian optics using Equation 2.4, the UV beam was set such that it would hit a fluorescent card before (14). A measuring tape was attached to the card and it was used as a reference for beam diameter measurements. Four diagonals were traced inside the beam mark as shown in Figure 4.3 and were later measured using ImageJ (a software to display, edit, analyze, process, save and print images [68]), and averaged to find the mean value of the widened beam diameter. The results are also shown in Table 4.2.

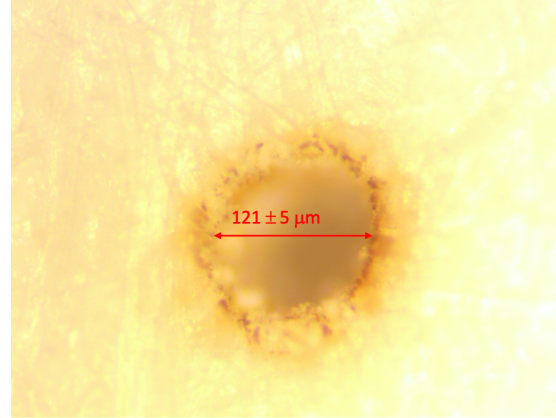
Figure 4.3(b) shows a saturation in the gray values, which represent the concentration of light in the center of the laser beam along the black line in Figure 4.3(a). Despite that, it is possible to delimit the beam from the background and to get an approximation of the error of the beam spot diameter. In order to do this, the width of the beam profile curve at two different gray values was taken and the relative difference between them was calculated. This value is then a statistical error and along with the systematic error provided by the calibration tools of Image J, it was taken into account for the final estimated error.

4.1.3 Comparison of beam spot measurements

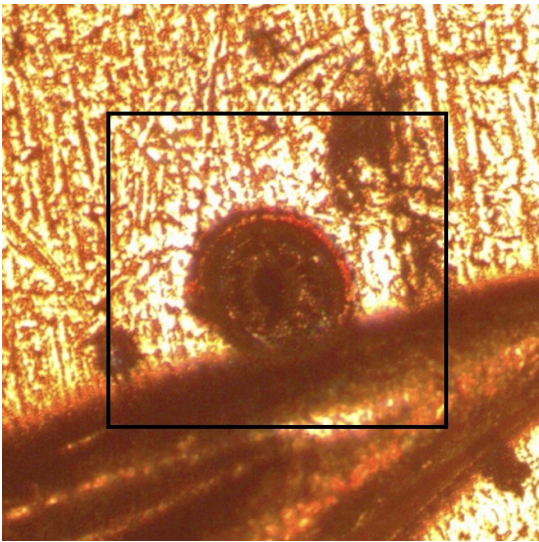
The presented laser spot size measurements produce values from 85 μm to 122 μm depending on an applied method. The discrepancy between these values could be a consequence of the method used for measuring the ablation mark diameter. Another explanation for this could be the background environment: for instance, a larger crater diameter



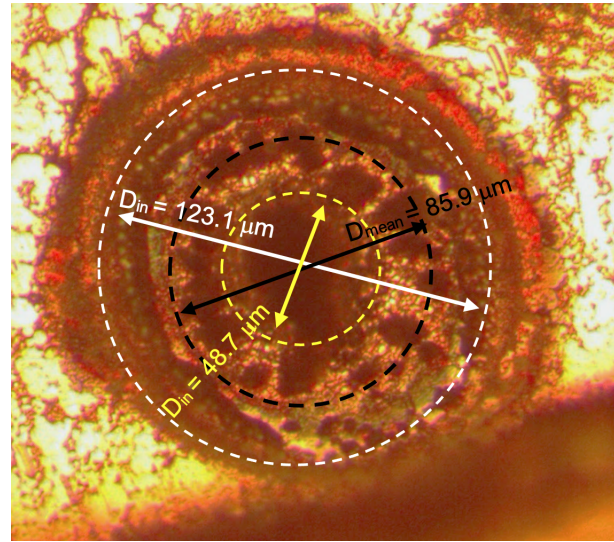
(a) Picture of a CD stamper. Device taken as a reference for length measurements.



(b) Ablation marks in thin paper. Result of a 2-minute long ablation exposure.

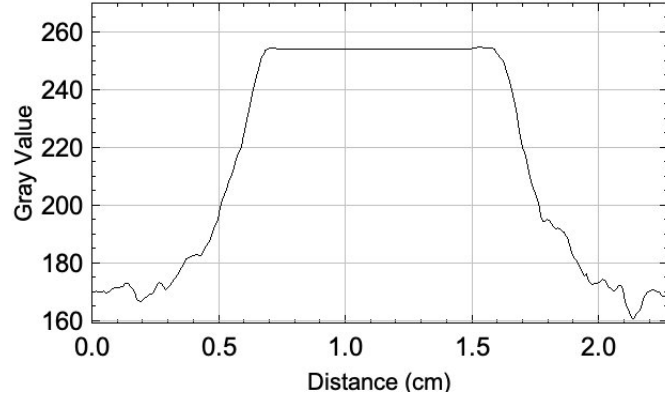
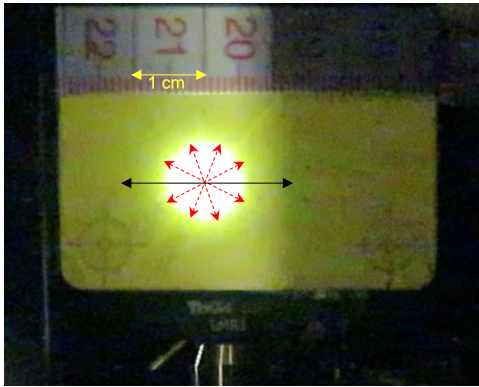


(c) A drill hole on the surface of the Cu sample resulting from the ablation process is shown inside the black square. It can be observed after a 10-minute exposure to the UV laser.



(d) Zoomed in section of Figure 4.2(c). Since the ablation mark included a large rim, an inner and an outer diameter were delimited. They are represented in yellow and white. Their diameters were averaged to find a mean diameter, a good estimation of the real value.

Figure 4.2: Images of the ablation marks on paper and a Cu sample after being exposed to a UV laser power $P = 40 \pm 0.1$ mJ.



(a) UV beam spot on the fluorescent card. A measuring tape was used as a reference for the measurement.

(b) UV beam profile obtained from a trace over the beamspot on the fluorescent card.

Figure 4.3: UV beam profile study. In (a) the four red arrows represent the traced diagonals to find the mean value of the unfocused beam spot diameter. The black arrow represent the section studied in the beam profile. In (b) the beam profile is studied and the gray value intensity is shown.

Diameter source	Mean value
Fluorescent card (unfocused beam)	(9 ± 1) mm
$2\omega_0$ (beam waist Equation)	(88 ± 9) μm
Ablation mark in copper	
Outer diameter (D_{out})	(123 ± 1) μm
Inner diameter (D_{in})	(49 ± 1) μm
Mean diameter (D_{mean})	(86 ± 37) μm
Ablation mark in paper	(121 ± 5) μm

Table 4.2: Resulting beam spot diameter values as obtained from different measurements. These values were obtained by using ImageJ and Toupview image analysis software.

can be obtained using paper since the ablation threshold is lower in air [66]. Despite that, while the resulting beam spot diameters differ slightly between different methods, they all indicate that the beam spot diameter is on the order of 100 μm . Using the latter value,



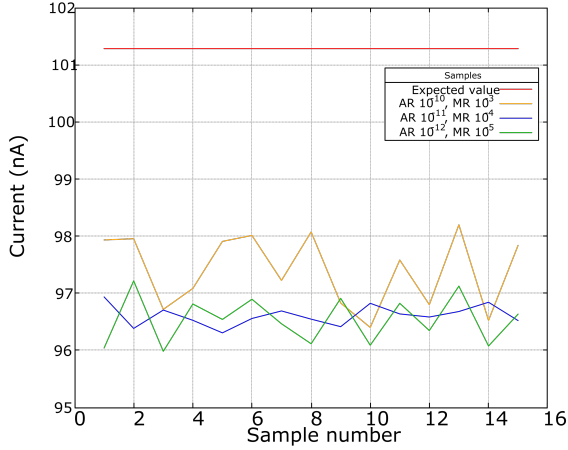
Figure 4.4: Circuit to study current data acquisition. 0.05 V were applied from an external power supply to a $493.7 \pm 0.1 \text{ k}\Omega$ resistor, leading to a current measurement of $\sim 100 \text{ nA}$.

an average power of 40 mW, a repetition rate of 1 kHz, and pulse duration of 1 ns, the outcome is a laser fluence of 1.01 J/cm^2 .

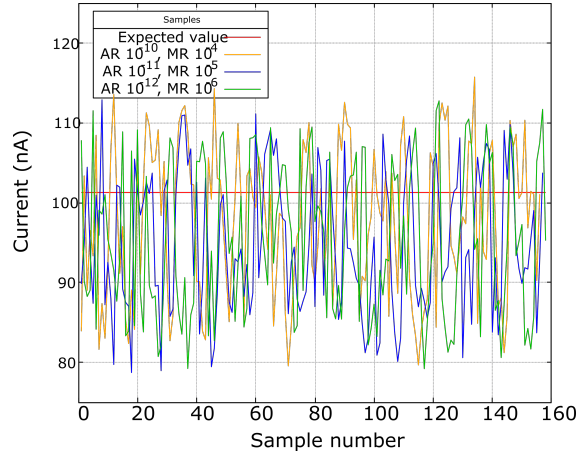
4.2 Current resolution measurements

The data acquisition methods play a crucial role in the sensitivity of the experiment, leading to real and accurate data. In this work, a Keysight 34465A is used to measure the current of ablated ions. The Keysight picoammeter acquires data through two main modes: *Auto-range* and *Manual-range*. The latter sets the order of magnitude given by the user, which fixes the sensitivity of the system. Auto-range sets the order of magnitude automatically, so the system changes its sensitivity range during every measurement. The first data sets were taken in auto-range mode which slowed down the data acquisition process significantly. To study the feasibility to take data in auto mode, an electronic circuit was used to measure current as shown in Figure 4.4. This circuit included a $493.7 \pm 0.1 \text{ k}\Omega$ resistor and an applied voltage of $50.00 \pm 0.01 \text{ mV}$, taking into account that values close to 100 nA were expected in the laser ablation measurements. These measurements were repeated using the *Manual-range mode* and compared to find the most effective way to take data for the upcoming experiments.

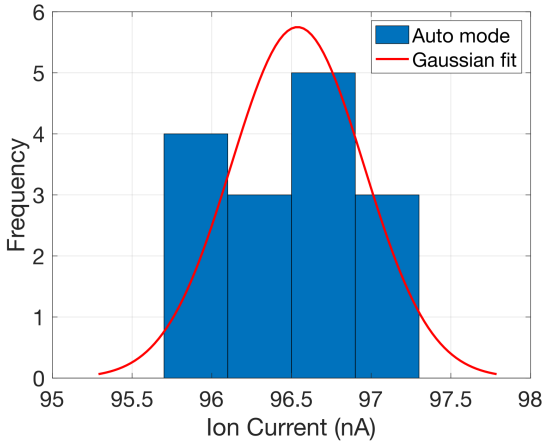
The resolution measurements showed that when using the manual range, the larger the set resolution value the longer it takes to collect data. Within two seconds 53 measurements were obtained with a dimensionless absolute resolution [69] of 10^{-6} , 11 measurements for a resolution of 10^{-7} , and 4 measurements for a resolution of 10^{-8} . Any other



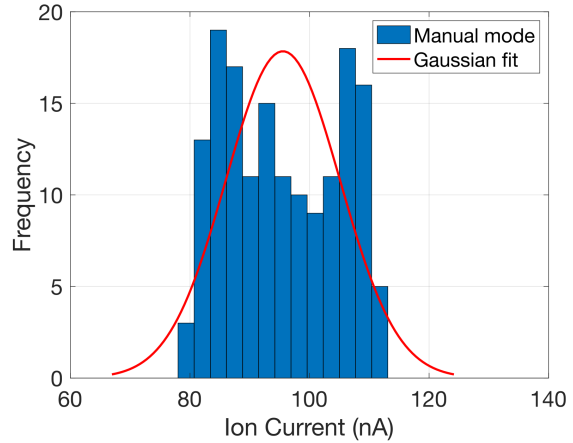
(a) Auto-range mode measurement results. Less than 20 data points were obtained with a small variation in the overall result, as shown in (c).



(b) Manual range mode measurement results. more than 150 data points were obtained, and the variation in the overall result is shown in (d).



(c) Data distribution obtained in auto-range mode.



(d) Data distribution obtained in manual mode.

Figure 4.5: Obtained results of the resolution measurements: (a) in auto-range (AR) mode, (b) and in manual-range (MR) mode. A representation of the data distribution (c) in auto-range mode and (d) in manual range mode. In (a) and (b) the red line represents the expected theoretical value (101 ± 1) nA.

value resulted in meaningless negative, extremely high values, or zero values.

This experiment was undertaken considering measurements previously executed with the LAS in similar conditions. Therefore, it was anticipated that the ion current values would be around 100 nA. In the resulting plots it is possible to see the discrepancy be-

Mode	Resolution set value	Mean value (nA)	Percentage difference
Auto	AR 10^{-10} , MR 10^{-3}	9.74	3.8%
	AR 10^{-11} , MR 10^{-4}	9.66	4.6%
	AR 10^{-12} , MR 10^{-5}	9.65	4.7%
Manual	AR 10^{-10} , MR 10^{-4}	9.77	3.5%
	AR 10^{-11} , MR 10^{-5}	9.51	6.1%
	AR 10^{-12} , MR 10^{-6}	9.55	5.7%

Table 4.3: Resolution results. The obtained values were averaged to find the mean ion current value for each data acquisition mode. The calculated systematic error (percentage difference) corresponds to the difference between the obtained value and the expected theoretical value (using Ohm’s law) from the circuit.

tween the obtained values and the expected value. The red line shown in the upper plots in Figure 4.5 represents the theoretical expected value as calculated from Ohm’s law. The rest of the color lines represent the scattered data obtained from the multimeter, which showed values around 100 nA as expected. The data for each line was averaged and the result is shown in Table 4.3. In order to find a mean value for these measurements, a secondary analysis was carried out. It consisted in creating histograms of the resolution plots and fitting them with a Gaussian function. From analyzing the histograms, it was possible to study the sampling rate’s impact on the consistency of the data and decide what is more important for the incoming results: if having a low amount of data points with higher accuracy (to get to know a mean value, for example) or a higher amount of data points with a slightly larger standard deviation (to study the overall trend in the data). Since the data values obtained in auto-range mode had a smaller standard deviation than in manual-range mode as shown in Table 4.4 all the measurements shown in the next sections were taken one time in auto-range mode to find the mean value, and then taken in manual-mode to obtain more data around it. The analysis shown in this work was based only on the manual-mode results.

Mode	Mean value (nA)	Standard deviation (nA)
Auto	96.5	0.4
Manual	95.5	9.5

Table 4.4: Statistical parameters obtained from applying a Gaussian fit to the ion current frequency plots shown in Figure 4.5.

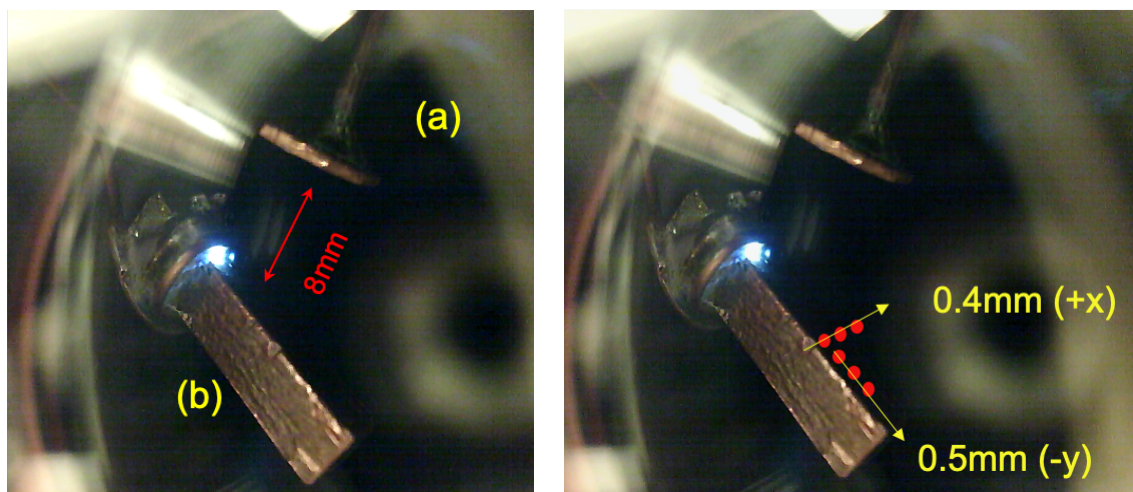
4.3 In-Vacuum measurements

For the in-vacuum measurements the pressure chamber was pumped down and the measured pressure by the full-range gauge was $P = (4.3 \pm 0.1) \times 10^{-7}$ Torr. The value remained the same for all experiments.

4.3.1 Ion plume

To ensure the IGLAS setup was set up properly and that it was possible to read current values, a voltage of -15 V (a starting value estimated in simulations) was applied to the collector plate, while grounding the target. The total set laser power varied from 50% to 90% in intervals of 10% until the ions plume could be observed with the camera shown at (15) in Figure 3.4. During all measurements the laser repetition rate was set to 1000 Hz. From Figure 4.6(a) the separation between the target and the collector plate can be inferred to be about 8 mm.

After several attempts of striking the target with the UV laser it was possible to focus the beam to its optimum concentration, leading to the long-awaited current signal in the LAS monitor, meaning that ions were being expelled out of the target. To verify ion ablation, the external camera was capturing images of the sample ablation process from the front side of the chamber. The ejection of ions from the copper source was confirmed by the observed ion cloud, which had a brilliant emerald color characteristic of copper [70]. Figure 4.7, which shows an image of the laser-ablated ion plume, was captured from an angle that distorts the object proportions. In order to guarantee the accuracy of the ion cloud



(a) External view of the (a) collector plate and the (b) target. The estimated separation between both electrodes is shown in red.

(b) Indicated laser ablation locations on target. Red dots indicate where the laser spot was moved. Measurements started at (5 mm, -3.5 mm) and ended at (5.16 mm, -3.70 mm) in mirror coordinates.

Figure 4.6: Rectangular copper target as seen through the front window. Fluorescence from the interaction of the UV laser with the sample material can be observed as blue spot.

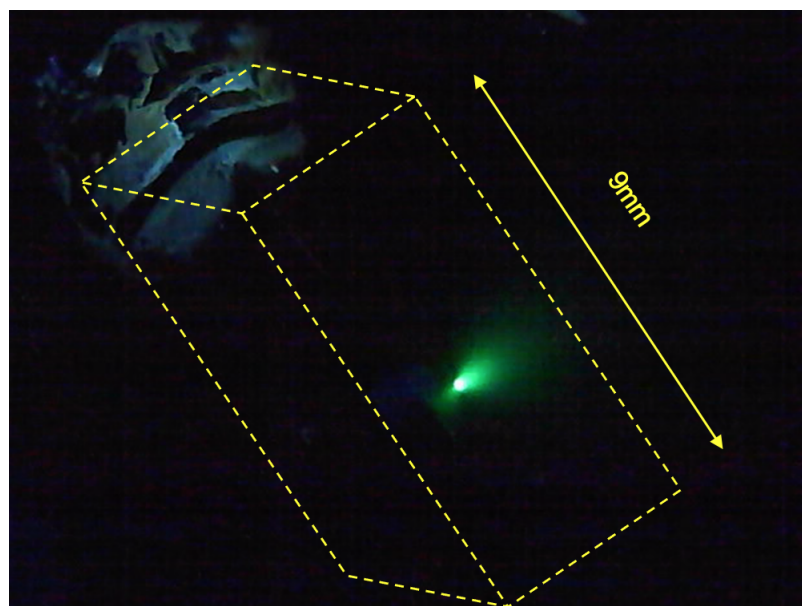


Figure 4.7: Observed ion cloud on a copper target surface. The laser beam hits close to the sample's midpoint. The target length of 9 mm is indicated in the Figure.

length, the target dimensions were obtained prior any measurements.

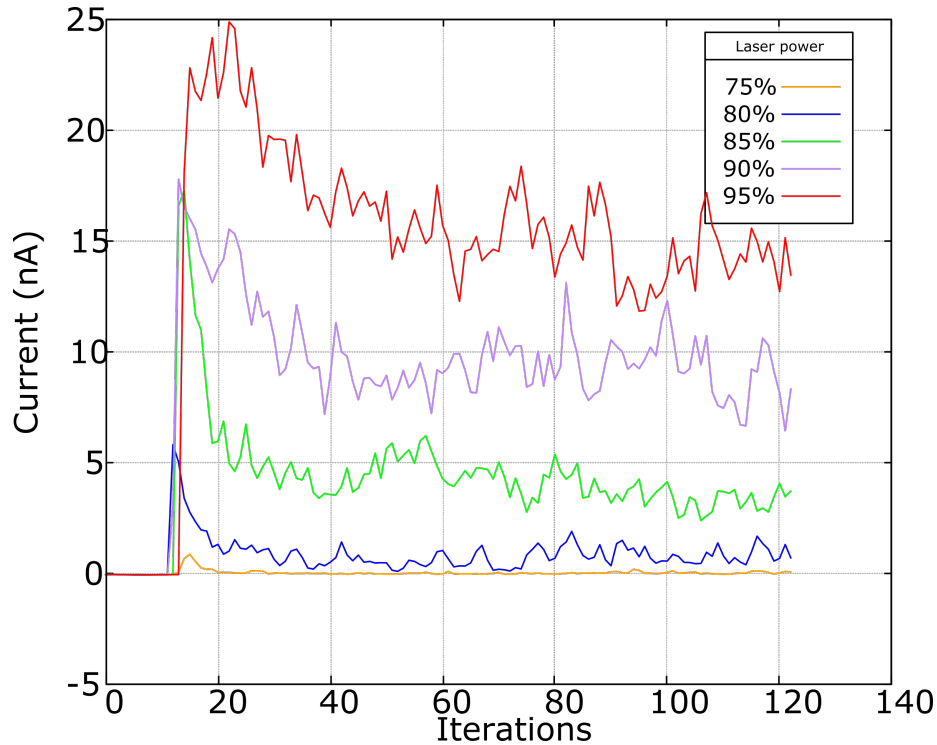
When the focused UV beam hits the target it ionizes superficial atoms. Depending on the energy concentration, atomic ions can be released from the material. These free ions are now positively charged and to attract them a negative bias must be applied to the ion collector. In the same way, if the target is positively biased then negatively-charged electrons will get attracted to it. One key approximation for describing this phenomena through simple equations (as will be shown later) is to assume a collisionless expansion since no background gas is present inside the chamber. The interaction of the laser target material in a vacuum produces plasma on the target's surface which expands significantly into the chamber. The plasma expansion takes place within a few ns [71] and if there is no more exposure, the complete process ends in less than 1 μ s. Experimental studies involving visible and UV laser ablation of metallic targets have shown that under laser intensities between 10^8 – 10^{10} W/cm², the produced plasma has a degree of ionization between 1% – 10% after the electron–ion recombination process and higher ionization occurs in the plasma right before recombination takes place [48].

4.3.2 Laser position and field dependence of ion current

In this section, the measured ion current was studied as a function of the exposure time. These measurements were subdivided in fixed and changing position. The results correspond to the ablation process being carried out at the same site through all the measurements and in different sites when changing the beam position.

Fixing the position of the ablation beam spot

To get control on the position of the beam, a particular pair of coordinates was set using Kinesis. These coordinates represent the position of the mirror, which can be moved from 0 mm to 12 mm in both axis. The laser spot was fixed at $x = 5.05$ mm and $y = 3.50$ mm. This positioned the beam at nearly the center of the target and allowed it to freely move in any direction over the frontal face. The laser power value was increased from 75% to 95% (equivalent to a change from 17 mW to 30 mW according to Table 4.1) in steps of 5%



on current decaying behaviour when ablation occurs at the same position for all the measurements. Each color represents an increase of laser power in 5%. All these measurements were obtained by applying -5 V to the ion collector and each iteration represents the average of 5 laser pulses.

Figure 4.8: I

for each voltage from 0 V to -20 V in steps of -5 V applied to the ion collector. Figure 4.8 shows the data for the particular case of -5 V being applied to the ion collector. The target electrode was grounded and nearly 120 measurements were obtained for this experiment. An explanation for these results is, when the laser strikes the metallic surface, it drills a hole which gets deeper as time passes by. As shown before, the melted material stays around the hole and accumulates, partially closing the ions exit way. In the same way, when the hole gets deep enough, the field lines coming from the extraction field will not penetrate into the hole anymore, therefore, leading to a lower extraction efficiency.

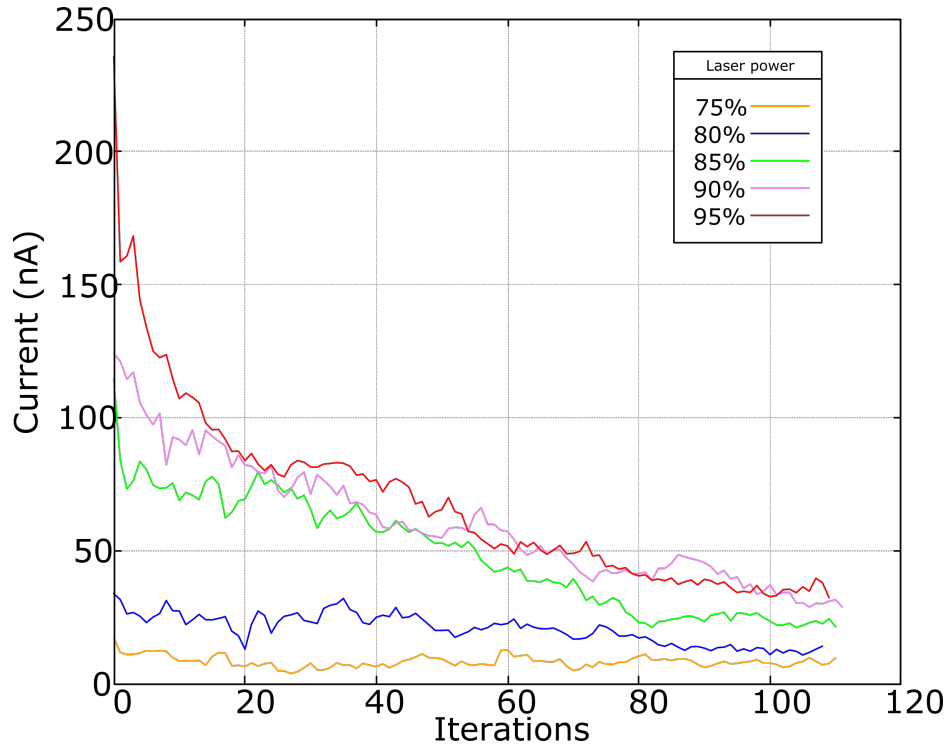


Figure 4.9: Ion current decaying behaviour when ablation occurs at a different position for each set of parameters. This position had no previous contact with the UV beam. As in Figure 4.8, each color represents an increase of laser power in 5%. All these measurements were obtained by applying -5 V to the ion collector.

Swaping the position of the ablation beam spot

For these measurements, all the set parameters remained the same except for the position of the ablation spot, which was previously fixed. The starting position was given by Kinesis at $(x = 5.00 \text{ mm}, y = -3.50 \text{ mm})$. The beam position was changed by $(+ 0.40 \pm 0.01)$ mm in the horizontal axis for every 5% increase in the laser power and $(- 0.50 \pm 0.01)$ mm in the vertical direction for every 5 V applied to the ion collector. For example: for 90% laser power ($P = 27 \text{ mW}$) and -15 V applied to the collector, the set coordinates would have been $(5.16 \pm 0.01 \text{ mm}, -3.65 \pm 0.01 \text{ mm})$.

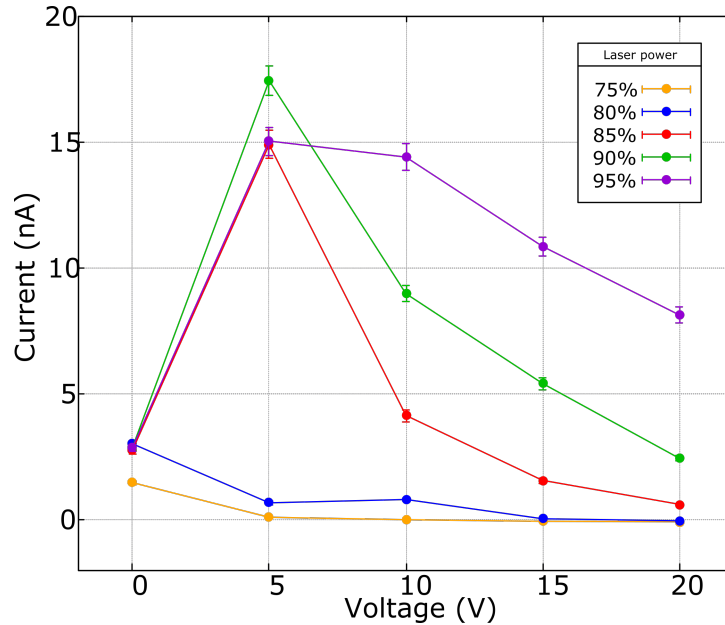
The experiment showed that after ~ 120 measurements (or 20 seconds of data) taken in auto-range mode the ion current curve flattens out and it is possible to treat it as a

constant. When repeated laser ablation occurs at a fixed position the ion current value becomes minimum with time. This can be seen in more detail in Figure 4.9.

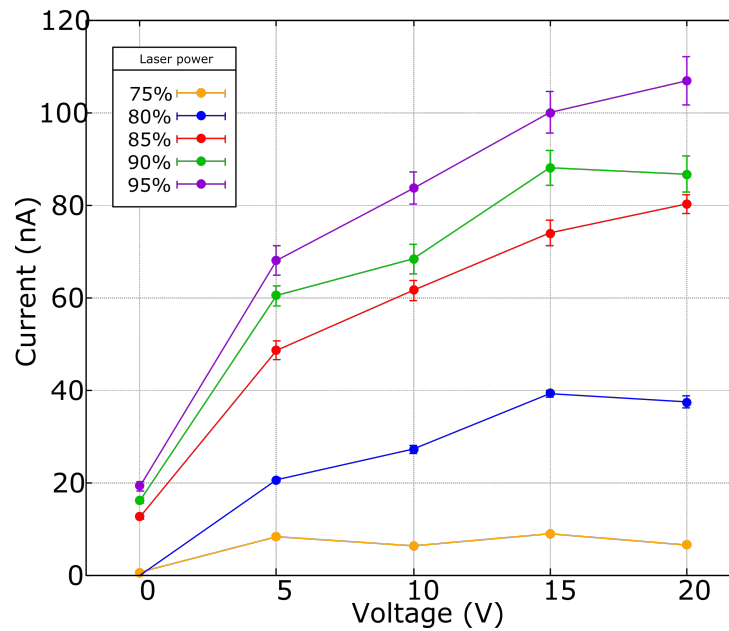
Two plots summarizing the results for both schemes are represented in Figure 4.10. In this Figure, the differences among the values show that in addition to the unexpected decaying behaviour, the current values differ by almost one order of magnitude. These results confirm that much lower ion current values are obtained when ablation occurs over a long period of time at a fixed position.

Mirror-target calibration

The traveled distance by the stepper motor mirror do not represent the same distance over the target surface. There is a conversion factor calculated for every target. This factor is a function of the intermediate lens and the final position of the target. When the sample gets replaced a couple of test measurements are first needed. The target position might vary by a few millimeters, thus a conversion factor must be calculated. An initial configuration showed that 0.1 mm mirror coordinates were equivalent to 1 mm on the sample. Beyond that, the values of the jogging parameters which represent the movement step size of the stepper motors are directly related to the ion current outcome. Moving the laser beam a distance of nearly 0.5 mm represented a large distance when compared to the target's dimensions. The latter can be seen in Figure 4.11. Shifting the ablation position lead to a change in the trajectories followed by the expelled ions before reaching the ion collector and possible systematic effects from differences in the electric field. Therefore, the step size was modified to be twice the diameter of the focused laser since the ablation process must be carried out on a different spot and essentially in the same area or as close to the previous point as possible.

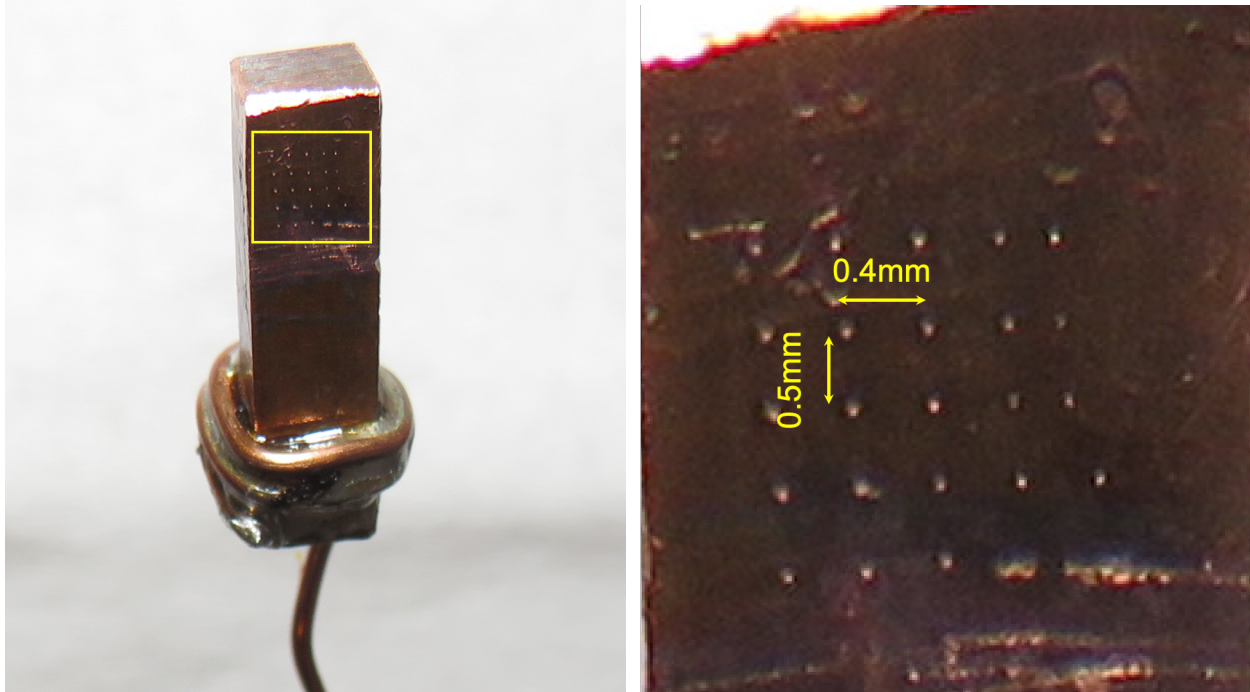


(a) Ion current obtained as result of laser ablation of a Cu sample. All measurements were taken at the same position, leading to a lower current output.



(b) Measurements taken over different positions on the sample's surface. A more detailed description of the changing position parameters can be found in the text.

Figure 4.10: Average ion current as function of the applied voltage on the collector plate. Each color represents a different energy density applied on the sample surface. Error bars were obtained by taking the variance of the data.



(a) Ablation marks are visible at the upper part of the sample.

(b) Ablation area zoomed in. A set of small craters as a result of 10-minutes ablation exposure can be observed. Arrows indicate the spacing on the target surface.

Figure 4.11: Ablation marks on the surface of the copper sample. Big gaps between two continuous ablation positions are shown. This was later changed to a step size of twice the beam diameter.

Target bias

Up to this point only the collector plate had been biased. In order to study the ion ejection efficiency, the next step was applying a bias to the target. The voltage in the target was increased from 0 V to 30 V in steps of 10 V at a laser power of 90%. A picture indicating the scan pattern is shown in Figure 4.12. For each applied voltage, the position of the beam in the target was changed in small increments. The starting coordinates were (4.98 mm, 3.51 mm) and the position was changed by 0.20 ± 0.01 mm in the x direction for every 10 V applied to the target, and -0.20 ± 0.01 mm in the y direction for every -5 V applied to the collector plate. At every position the average ion current on the collector was measured.

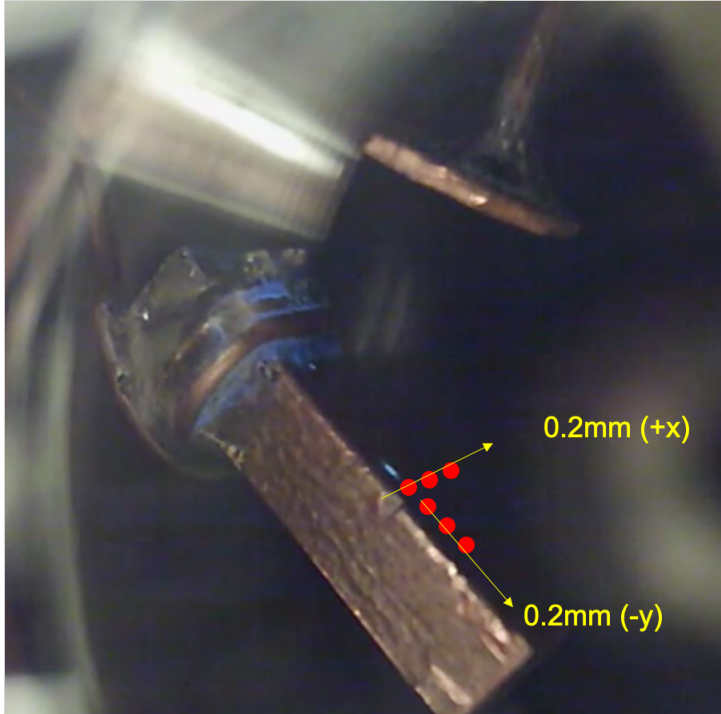


Figure 4.12: Scan pattern followed over the surface of the copper target, while being biased. The laser spot mapped the target surface by switching 0.2 mm in +x or -y for every voltage from 0 V to 30 V in steps of 10 V.

The voltages applied to this electrode resulted in a boost in the measured ion current, for a comparable time exposure. The resulting plot (Figure 4.13) shows a decaying behaviour as for previous measurements, when the target was grounded. A summary of the averaged values as function of the applied voltages is shown in Figure 4.14. From the measured current values it is possible to get an estimation of the amount of ions leaving the target per unit time. This value will be calculated in the following section. The amount of free ions can be later compared to the associated charge of a single ion (in this case Cu^+), giving a description of the charge-size relation in the ion plume formation process.

4.3.3 Ion current dependence on the target position and geometry

From previous sections it was found that the measured ion current can easily increase when changing parameters directly linked to the target. In order to find the values which maximize the ion current, measurements were carried out taking the target itself as the main point of interest.

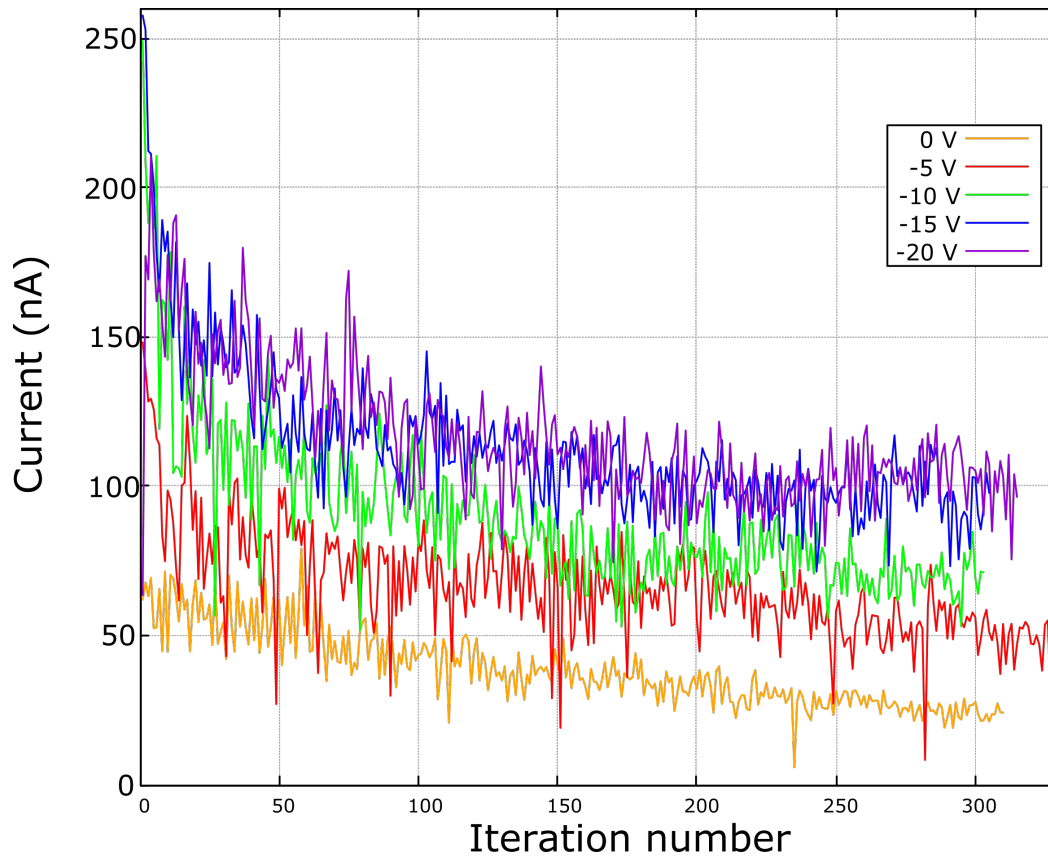


Figure 4.13: This plot shows the ion current trend decaying over time in the particular case when 10 V are applied to the target electrode. Different colors represent every studied value from 0 V to -20 V in steps of -5 V, applied to the collector plate.

Scanning the edge of the rectangular target

Along with the exposure time, another studied feature was the sample surface and its correlation with the ablation process. This involves studying the characteristics of the geometry and the area exposed to the UV beam. To do this, measurements were performed with various target shapes and textures. A series of 1D scans along a line were executed on the surface of the Cu sample, searching for irregularities in the material. These measurements consisted of scanning vertical and horizontal lines over the surface to observe the gradient in measured ion current. The scans were carried out on-target speeds of¹: 1.5 mm/s, 0.6 mm/s, 0.3 mm/s and 0.2 mm/s as shown in Figure 4.15. These plots rep-

¹These values correspond to the displacement on the target surface in millimeters per second.

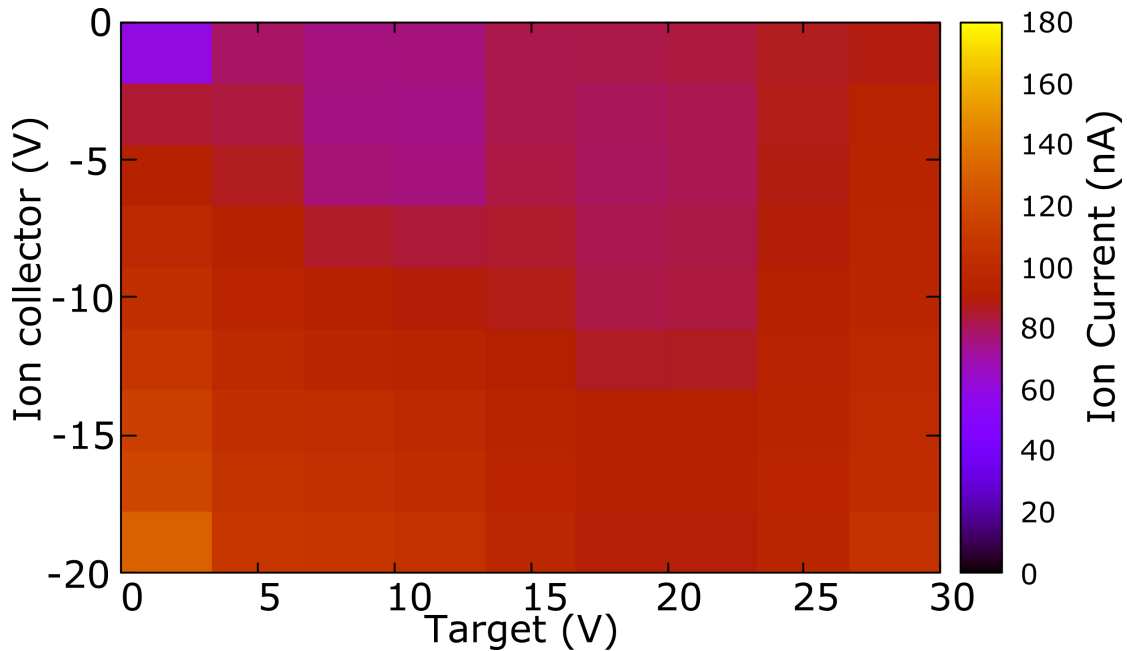
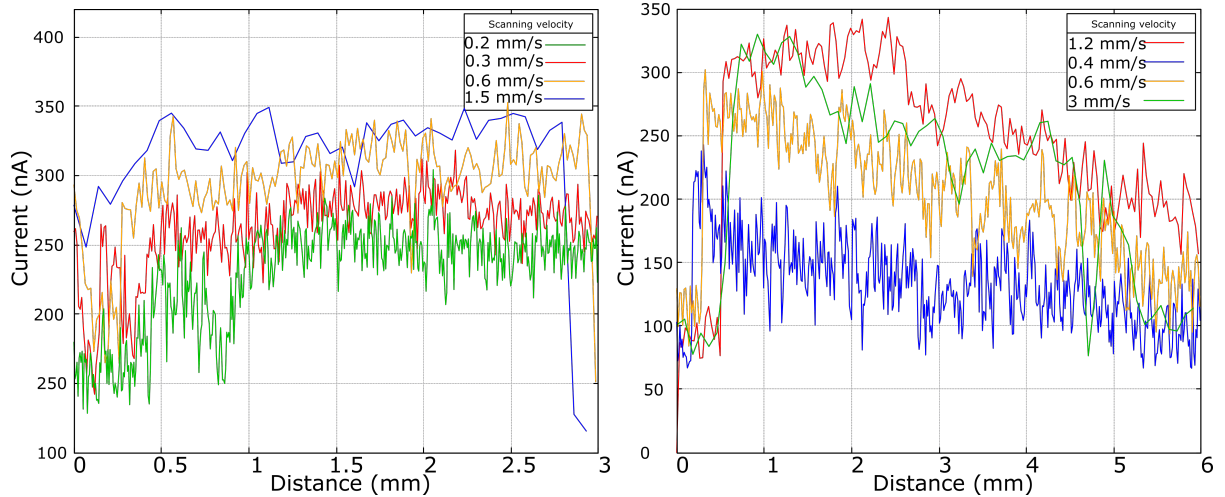


Figure 4.14: Ion current plot as function of applied voltages in the rectangular target and in the collector plate. For most voltage configurations the measured current was around 100 nA.

resent the results in target coordinates of the vertical and horizontal scans, respectively. The scans were performed at four different velocities represented by the lines of different color. The laser power and the repetition rate were fixed at 90% and 1000 Hz, respectively which calculates to $(27.0 \pm 0.1 \text{ mW})$ laser power. Since the current values oscillate around 250 nA for bidimensional scans at different velocities, it is possible to take the target's surface along the vertical and horizontal axis as uniform.

Changing the shape of the copper target

The geometry as well as the position of the target were changed. This was done to investigate potential systematic effects arising from either surface or edges of the new target. While still having copper as the studied material the target was changed from a rectangle to a circular plate (see Figure 4.16). Unlike the previous sample, this was essentially a disk of 5 mm diameter and 1 mm thickness. The surface of this target was smoother and



(a) Results of the horizontal scans. The UV beam travelled 3 mm along the horizontal axis.

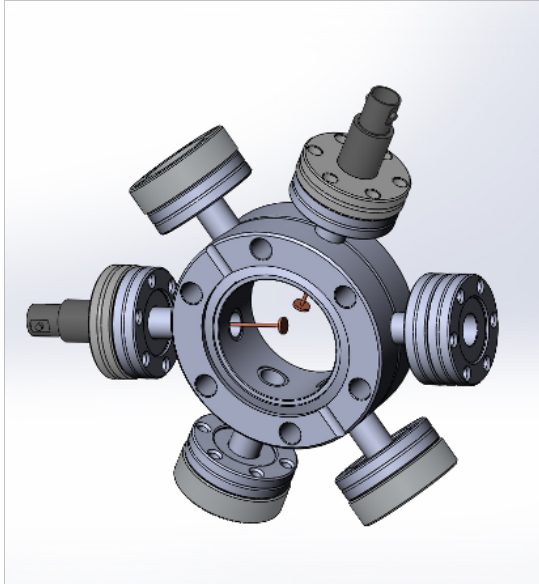
(b) Results of the vertical scans. The UV beam travelled 6 mm along the vertical axis.

Figure 4.15: 1D scans of the rectangular Cu target. The upper plot represents scans along the horizontal edge. The lower plot represents scans along the vertical edge. The scans were performed at four different velocities in target coordinates, represented by the lines of different color. Length values correspond to target coordinates.

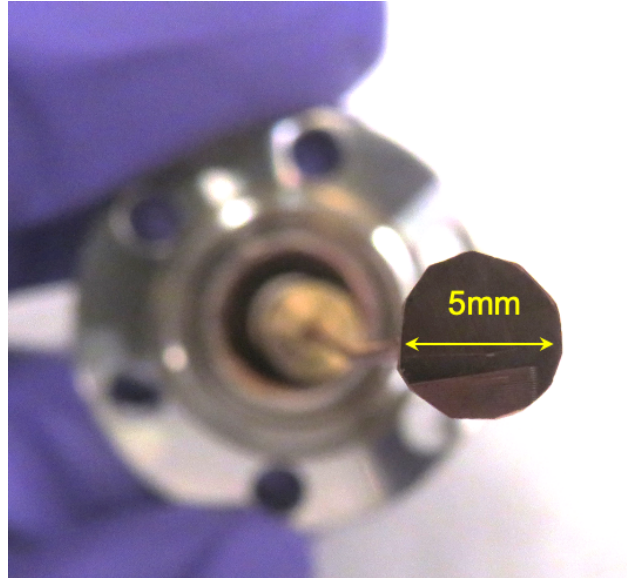
the ablation effective area (the area over the target surface in which the incident laser can strike) did also increase.

Scanning line segments on the circular target

Because of the circular geometry of the target horizontal (passing close to the diameter) as well as vertical scans (passing through the bottom crescent) were conducted. The scan direction on the target is indicated in Figure 4.17. The bias on the target electrode was changed from 0 V to 30 V in steps of 10 V and from 0 V to -20 V in steps of -5 V on the collector plate. The displacement made by the beam for each step is expressed in mirror coordinates. The laser power value was measured and fixed at 90% ($P = 27$ mW) and manual-range for data acquisition was set to take ~ 160 measurements in nearly 5 seconds at each laser location. The results are summarized in a heat map shown in Figure 4.18, where the ion current has been plotted as function of applied voltages in the circular target and in the collector plate. The results show that for more negative collector biases



(a) Engineering rendering of the chamber with the circular target geometry.



(b) Image of the circular Cu sample attached to a CF 1.33" flange. The diameter dimension is shown in yellow.

Figure 4.16: External view of the pressure chamber with modified geometry and position of the target.

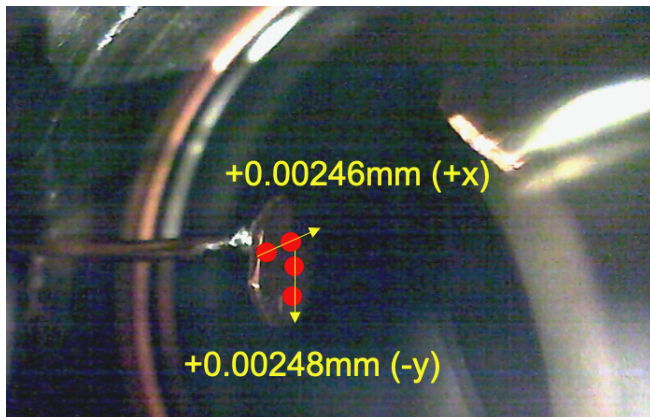


Figure 4.17: Photograph of the target with scanning steps indicated on its surface. For these measurements a bias from 0 V to +30 V in steps of 10 V was applied to the target. The quantity shown in yellow represents the displacement made by the beam for each step, in mirror coordinates.

the applied bias on the target is becoming less of an importance.

After applying various voltages to the circular target, the measured ion current was found to be $\sim 1\mu\text{A}$ (see Figure 4.19). Moreover, the differences between the obtained values in Figure 4.18 and Figure 4.19 come from the different ion production approaches. In Fig-

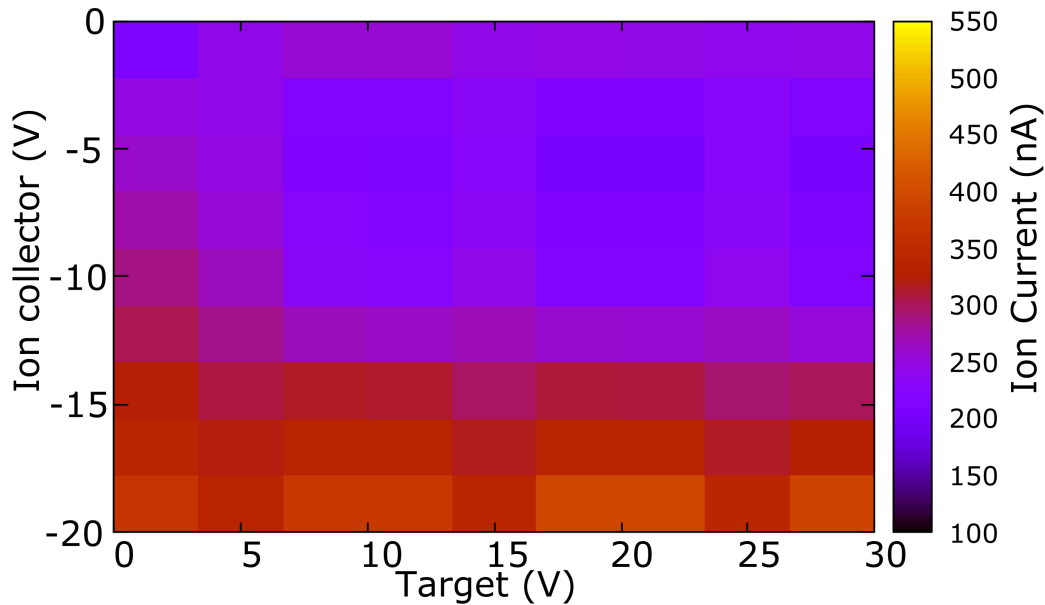


Figure 4.18: Ion current plot as function of applied voltages in the circular target and in the collector plate. For most voltage configurations the measured current was around 200 nA.

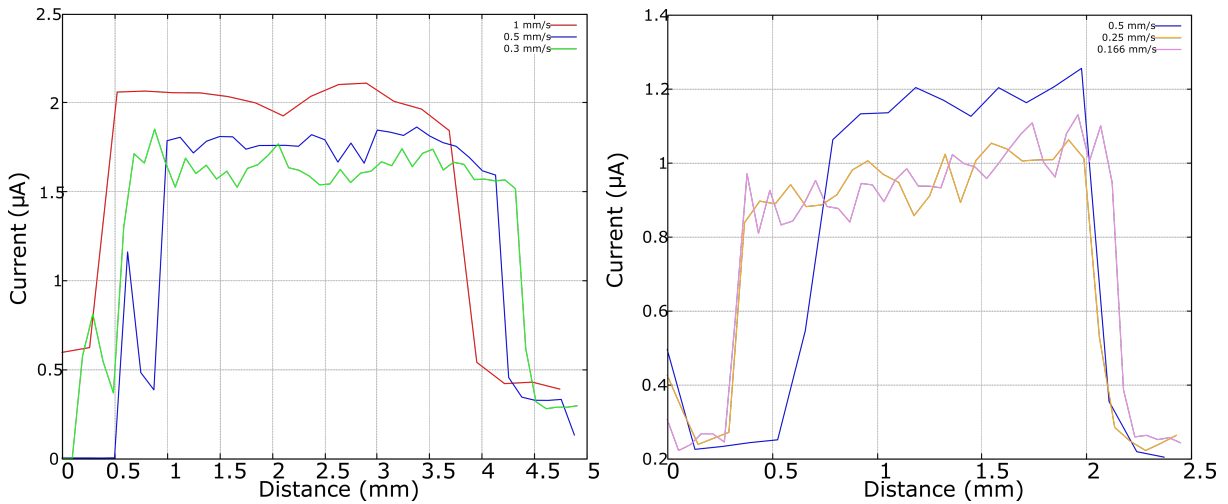
Figure 4.18 the ion cloud is produced by ablating the surface continuously in the same spot whereas in Figure 4.19, the values are the outcome of an ion cloud generated by a laser beam in movement. This means ablating new position every time, avoiding the creation of rims from the melted material, releasing more ions and consequently increasing the measured ion current. In fact, different experimental methods use rotating targets while performing laser ablation [72] to prevent these changes in ion current.

The overall observed values increased by almost one order of magnitude compared to previous targets. The applied electric field is expected to dominate the overall ion dynamics. However, some factors that could have contributed to this growth are: 1) The distance between the electrodes was increased by a few millimeters. Since the previous

sample had larger dimensions, the bottom end of the sample was closer to the collector plate by default; 2) The position of the target inside the pressure chamber. The target electrode was switched to a neighboring contiguous flange colinear to the incoming beam port. This would position the sample perpendicular to the beam plane, tilting the ions plume by 60° from the incoming beam plane and increasing the amount of ions flying directly towards the collector plate. The angled position of the previous sample lead to less power density per unit area. This results in lower fluence values and complicates the ablation process; 3) A higher purity of the sample composition. The two copper samples were not taken from the same source. It could have been that something in their composition differed or one sample was slightly contaminated with other elements. 4) The physical characteristics of the sample. This can be better explained through Figure 4.20. The rectangular-shaped sample had an uneven surface unlike the round target, which had a polished finish. Since the measured ion current values increased for the circular target, the roughness of the rectangular target potentially contributed to getting ions expelled in aleatory directions, similar to the diffuse reflection phenomenon in optical physics. This means that previous alterations in the target's surface will be reflected on further current measurements.

Evolution of the copper ion cloud

The size and evolution over time of the ion cloud produced from the circular copper target can be seen in Figure 4.21. For instance, the shape of the ion plume could be divided in two sections. The inner section has a well-defined elliptical shape where the size is hard to estimate because of the viewing angle. The outer section on the other hand resembles a parabola where the aperture points towards the incoming beam port. It does maintain its shiny green color and it gets a white tone on the spot of highest concentration. The size and the duration of the ion cloud are a function of the applied voltages on both electrodes. An estimation of its dimension was obtained when 20 V and -30 V were applied to the target and the ion collector, respectively. From posterior image processing the ion



(a) Results of the horizontal scans. The UV beam travelled 5 mm along the horizontal axis. (b) Results of the vertical scans. The UV beam travelled 2.5 mm along the vertical axis.

Figure 4.19: 1D scans of the circular Cu target. The left plot represents scans along the horizontal edge. The right plot represents scans along the vertical edge. The scans were performed at three different velocities represented by the different color lines. Length values correspond to target coordinates.

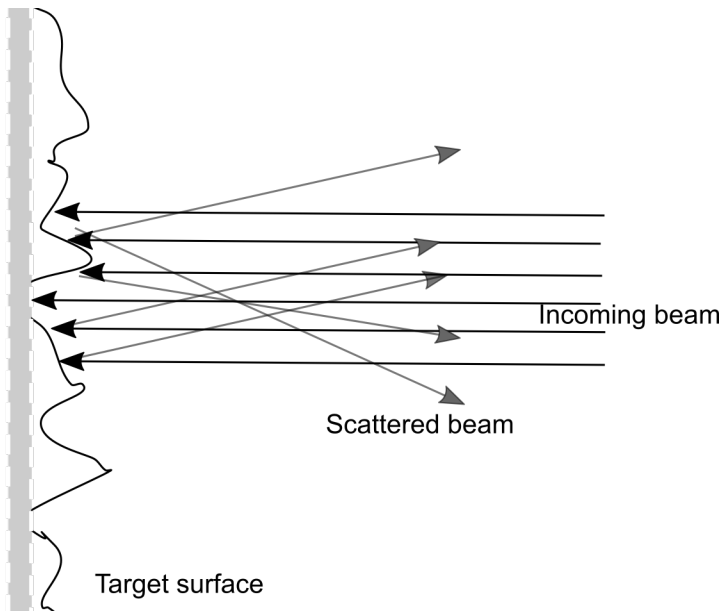


Figure 4.20: The roughness of the rectangular target may have contributed to getting ions expelled in aleatory directions, similar to the diffuse reflection phenomenon in optical physics.

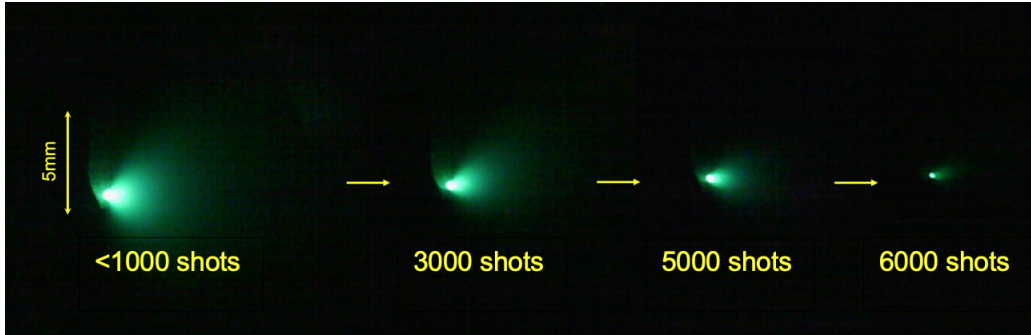


Figure 4.21: Ion plume with circular target of a copper sample. This picture represents the evolution of the ion plume since its emergence at < 1000 laser shots until its gradual disappearance at nearly 6000 shots, after ~6 seconds of ablation at the same position.

cloud was determined to have an approximate extension of 5 mm under the previously mentioned conditions. The evolution time of the cloud's first captured moment until its disappearance was around 6 seconds with laser on.

Ablated ion flux

An estimation of the ion loss rate as a function of the applied fluence would serve as an indicator of how efficiently ions are created on the target². Through the ion current measurements it was intended to find the mass loss rate during the ablation process.

To calculate the accumulated charge Q_{ac} in a period of time t (equivalent to the system signal duration of the laser running at 1 kHz repetition rate) would be the first step to find the loss rate. Previous results have shown that for the measurement time t the current value I is on the order of 100 nA. Then from

$$Q_{ac} = I \cdot t \quad (4.1)$$

²Another way to find it could be by applying scanning white light interferometry to the resulting craters produced on the sample as in [73].

it is determined that $Q_{ac} = 1 \times 10^{-10}$ C per laser shot. Considering singly ionized particles being ejected from the target, the charge of every single particle would be equivalent to $Q_s = 1.6 \times 10^{-19}$ C. The number of ions N_i is calculated as

$$N_i = \frac{Q_{ac}}{Q_s}. \quad (4.2)$$

Therefore, around 6×10^8 ions were leaving the target per second or 6×10^5 ions per laser shot.

4.3.4 Gold sample ablation measurements

Following Cu as the material under investigation the target was replaced by a gold (Au) foil of dimensions $5 \text{ mm} \times 5 \text{ mm} \times 0.1 \text{ mm}$ as shown in Figure 4.22. This target had a particular square-shape with a thickness less than 1 mm and the surface was smooth and shiny in comparison to the dull surface of the copper samples. As the target electrode and its position changed it was necessary to re-calculate the conversion factor for the mirror and target coordinates. The conversion factor was obtained knowing that in order for the beam to travel 1 mm over the gold target surface, the mirror actuators must shift 0.14 mm.

1D scans

1D scans were performed over the vertical and horizontal axis of the Au target. This was mapped by travelling through the sample's vertical and horizontal axis at different velocities: 2.5 mm/s, 1 mm/s, 0.5 mm/s and 0.3 mm/s. The latter can be seen in Figure 4.23. The UV beam travelled 5 mm along the horizontal and 5 mm along the vertical axis. The plots represent scans along the horizontal and vertical edge, respectively.

During these measurements a voltage of -10 V was applied to the collector plate and 10 V to the target electrode. The current was set to 90% laser power and the repetition rate to 1000 Hz. These parameters remained fixed during this set of measurements. The calculated mean for each measurement is shown in Table 4.5.

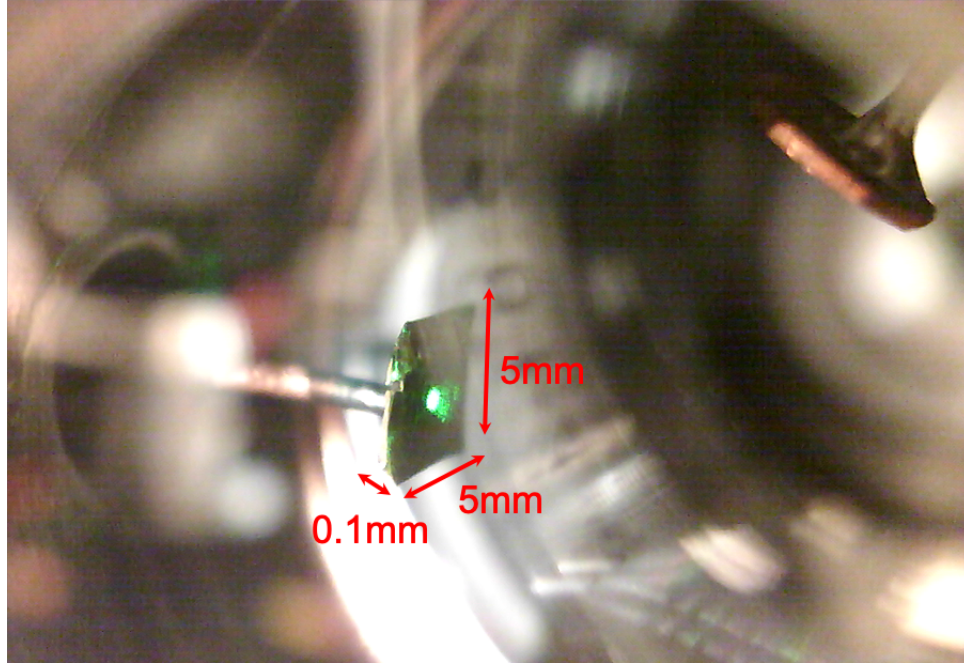


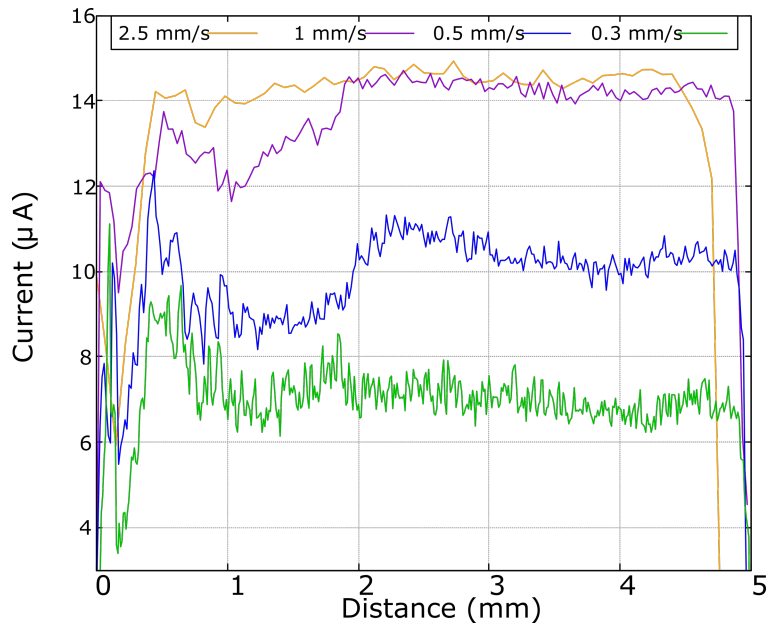
Figure 4.22: In-vacuum setup with Au foil target. The 532 nm alignment laser can be seen striking the surface of the target. Dimensions are shown in red.

Scan velocity (mm/s)	Average measured current (μA)	
	Horizontal scan	Vertical scan
0.3	13 ± 3	11 ± 4
0.5	13 ± 2	10 ± 4
1	10 ± 1	10 ± 3
2.5	7 ± 1	10 ± 2

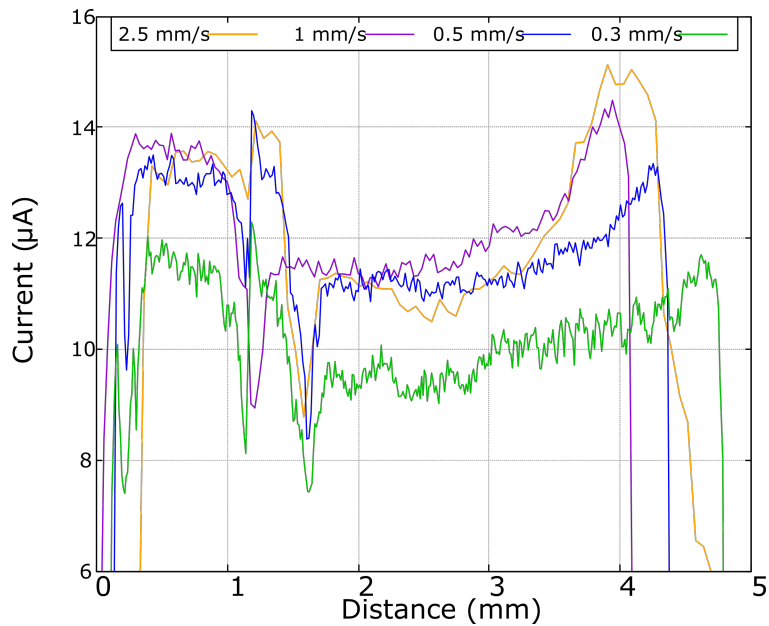
Table 4.5: Average measured current obtained from 1D scans in gold. The calculated error corresponds to the standard deviation of the studied data.

Repetition rate and laser power dependence

Up to this point, the repetition rate of the laser has remained fixed at 1 kHz. To see the influence of this parameter, vertical and horizontal scans were performed changing the UV laser repetition rate to 100 Hz, 250 Hz, 500 Hz, 750 Hz and 100 Hz as shown in Figure 4.24. Through these results it is possible to conclude that the repetition rate and the measured ion current in the detector are directly proportional. The mean value for each measurement was obtained. The results are shown in Table 4.6. For these measurements



(a) Results of the horizontal scans. The UV beam travelled 5 mm along the horizontal axis.



(b) Results of the vertical scans. The UV beam travelled 5 mm along the vertical axis.

Figure 4.23: 1D scans of the square-shaped Au target. The top plot represents scans along the horizontal edge. The lower plot represents scans along the vertical edge. The scans were performed at four different velocities represented by the different color lines. Length values correspond to target coordinates.

Repetition rate (Hz)	Average measured current (μA)	
	Horizontal scan	Vertical scan
250	2 ± 1	3 ± 1
500	5 ± 2	5 ± 4
750	7 ± 2	7 ± 3
1000	10 ± 1	10 ± 4

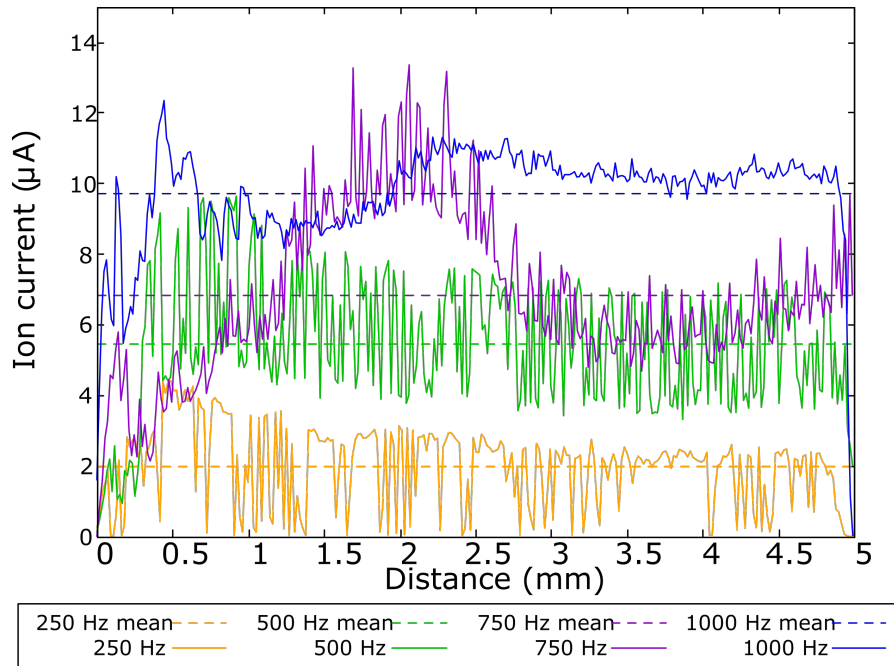
Table 4.6: Average measured current obtained when changing the laser repetition rate on the target's surface. The calculated error corresponds to the standard deviation of the studied data.

Laser power %	Average measured current (μA)	
	Horizontal scan	Vertical scan
65	0.01 ± 0.02	0.4 ± 0.6
70	0.6 ± 0.3	3 ± 1
75	2 ± 1	5 ± 1
80	4 ± 2	8 ± 2
85	8 ± 2	8 ± 5

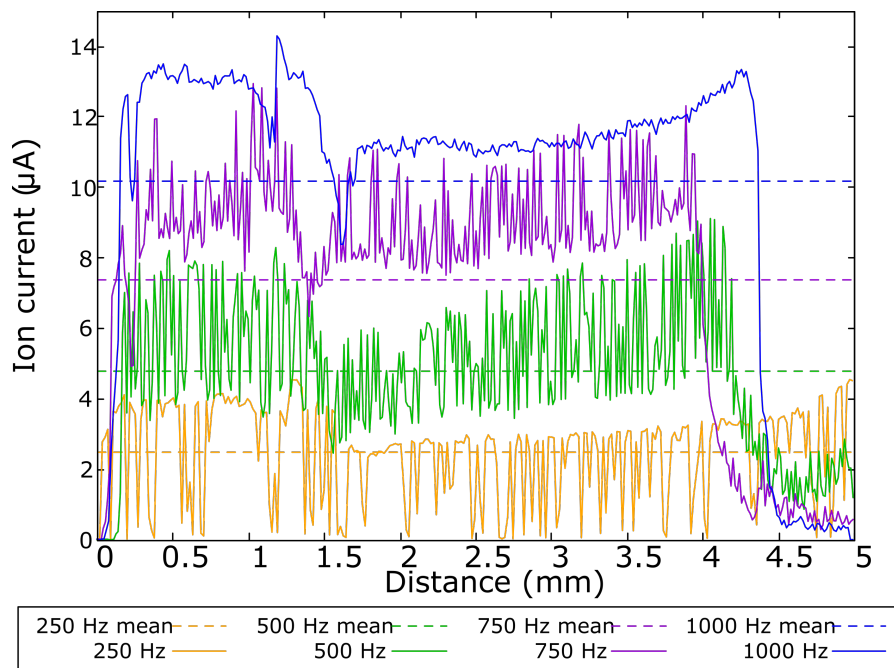
Table 4.7: Average measured current obtained when changing the laser power on the target's surface. The calculated error corresponds to the standard deviation of the studied data.

the scanning velocity was set to 0.5 mm/s.

Later, to study the ion current variation of the Au sample on the emitted laser power, the latter was set from 65% to 85% (this is from 11.2 mW to 24.3 mW) in steps of 5% at 1 kHz. The resulting plots can be seen in Figure 4.25 and the mean values are shown in Table 4.7. The measured current values were higher than those measured for the Cu sample for comparable laser power (see Figure 4.10). These values led to the production of an ion cloud in the gold sample easily observed applying no bias to the electrodes. Particularly the observation of an ion cloud was unexpected. For copper it was very difficult to see the ion cloud when both electrodes were grounded (see Figure 4 in the Appendix section). Even though, previous SIMION simulations predicted a larger ion cloud. From the energy density laser measurements it was found that the minimum power the laser must be set to get a current reading is 64% ($P \approx 10.5$ mW) for gold, whereas for copper

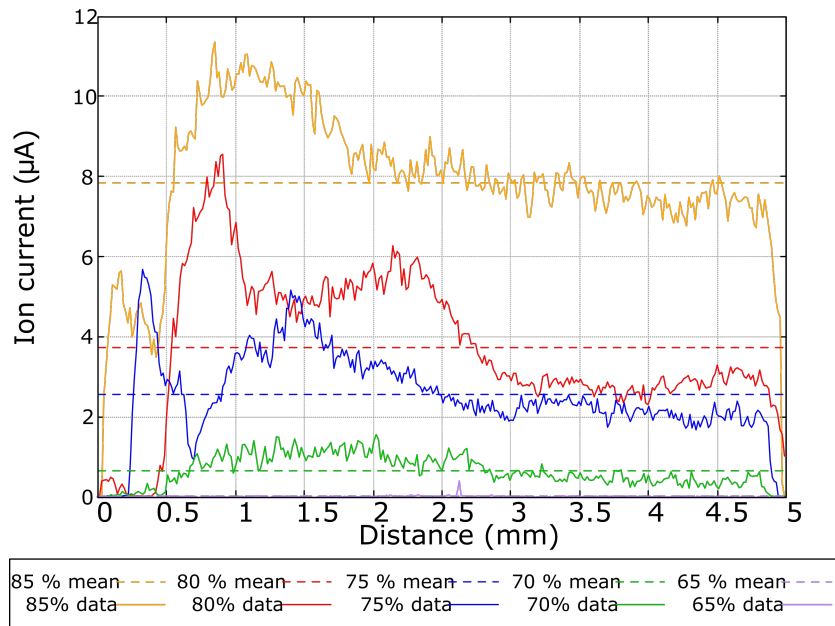


(a) Horizontal scans in Au.

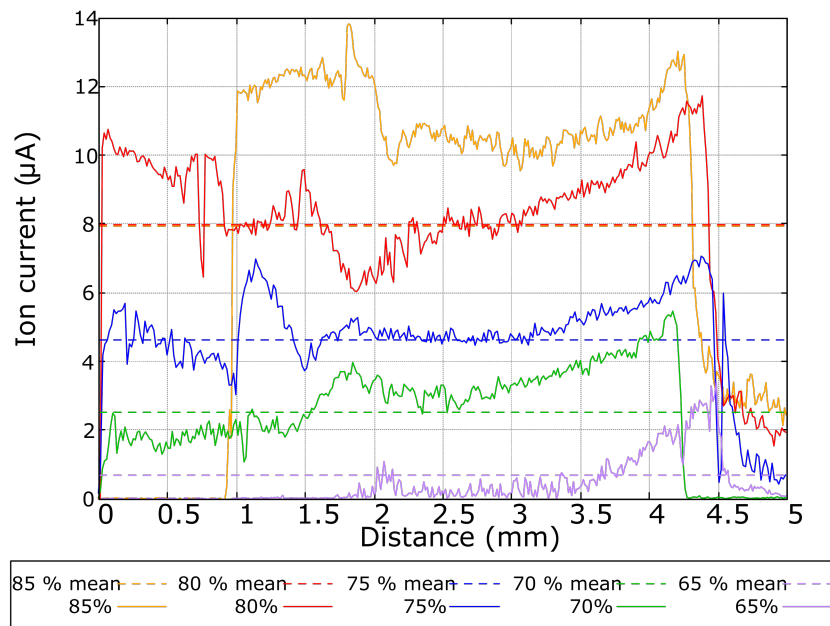


(b) Vertical scans in Au.

Figure 4.24: Results of the scans performed over the surface of the Au target, at laser repetition rates of 250, 500, 750 and 1000 Hz. The dotted lines represent the estimated mean value for each vertical measurement. The scans show that the greater the repetition rate set value, the greater will be the measured current.



(a) Results of the horizontal scans at different laser power.



(b) Results of the vertical scans at different laser power.

Figure 4.25: Laser power variation on the Au target. The upper plot represents scans along the horizontal edge. The lower plot represents scans along the vertical edge. The scans were performed at five different laser power represented by the different color lines. Length values correspond to target coordinates.

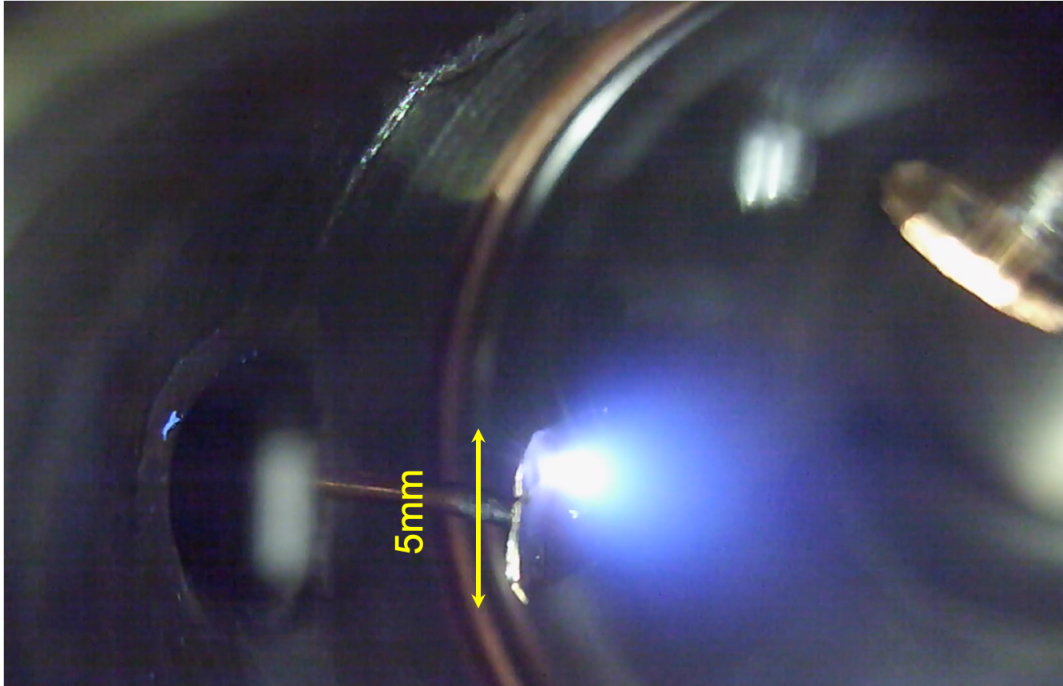


Figure 4.26: The blue and purple color of the ion cloud can be seen as result of Au ablation. The dimensions of the cloud are comparable with the size of the sample.

this value corresponds to 73% ($P \approx 16$ mW).

For Au, the ion cloud shows a blue color with a few purple shades as shown in Figure 4.26. The inner section size of the ion cloud was big and dense enough as to leave burn marks a few millimeters around the ablation spot. A contrast between the ion clouds obtained from Cu and Au respectively can be found in Figure 5 in the Appendix section.

Biasing the collector plate

The next step for the surface analysis was to bias the collector plate. The resulting curve showed a notable bump one second after the laser first hit the target denoted as the highest peak in the ion current plots in Figure 4.27. This occurred for all the measurements with the gold sample. Interestingly, if these measurements taken in manual range mode of the multimeter had instead been taken using the autorange mode, the bump would have been lost and the corresponding values would have quickly decayed to a flat line.

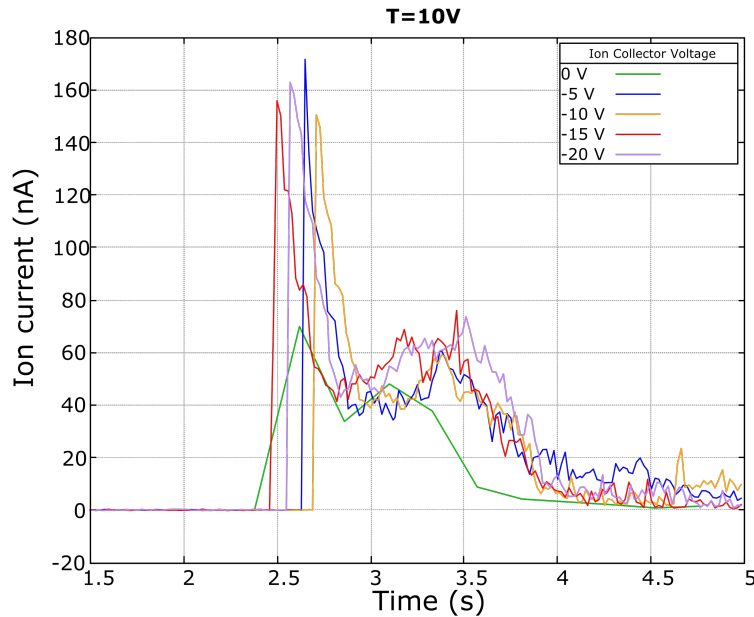


Figure 4.27: Ion current measured for voltages between [0 V, -20 V] applied to the ion collector. For these measurements, the target was biased at a fixed 10 V.

An interpretation for this bump might be oxidation or contamination layers on the sample surface, but this is unclear and yet to be confirmed under the microscope.

Au target mapping

The Au studies followed the same structure as for the Cu target. The ablation process started with both electrodes grounded, then the field was changed as the laser was moved. A full mapping was undertaken by applying a bias to the collector plate from 0 V to -20 V in intervals of -5 V. Likewise, the target bias was increased from 0 V to 30 V in steps of 10 V and again shifting the laser on the target surface by an equivalent distance of twice the beam diameter vertically and horizontally. Every measurement consisted of 5 seconds of data acquisition in manual-range mode with 90% laser power and 1000 Hz repetition rate.

Map of the applied bias

The heat map shown in Figure 4.28, represents the current distribution of the gold target according to the applied bias. The obtained results show a uniform response, being not

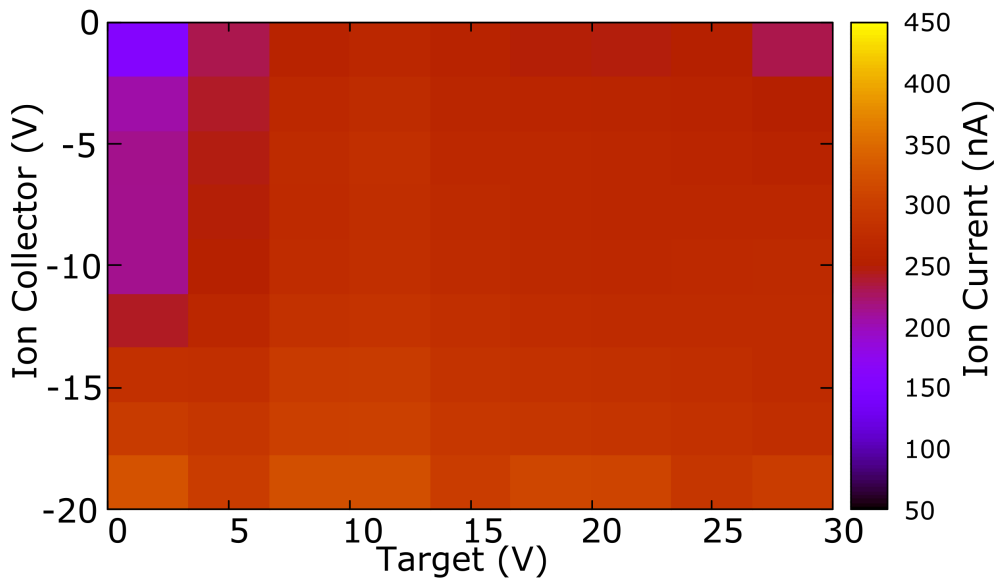


Figure 4.28: Intensity map of ion current for different collector and target voltages. Every color represents the average ion current calculated for the coincident applied voltages. High values are obtained even when both electrodes are grounded.

highly sensitive to small voltage changes. Larger applied bias might show larger ion current values and consequently a more massive ion plume.

A heat map representing the measured current obtained from the Cu and the Au target are compared in Figure 4.29. These measurements were taken under similar conditions, with different target materials. This allowed one to observe the differences between the ion current distribution over the applied voltages. The heat maps follow the same color scale. When compared to gold copper seems to produce lower ion current values.

Measuring the leaving current

In order to verify the collection efficiency of the collector plate, the ion current was measured using a different approach. Unlike the previous procedures, the target was con-

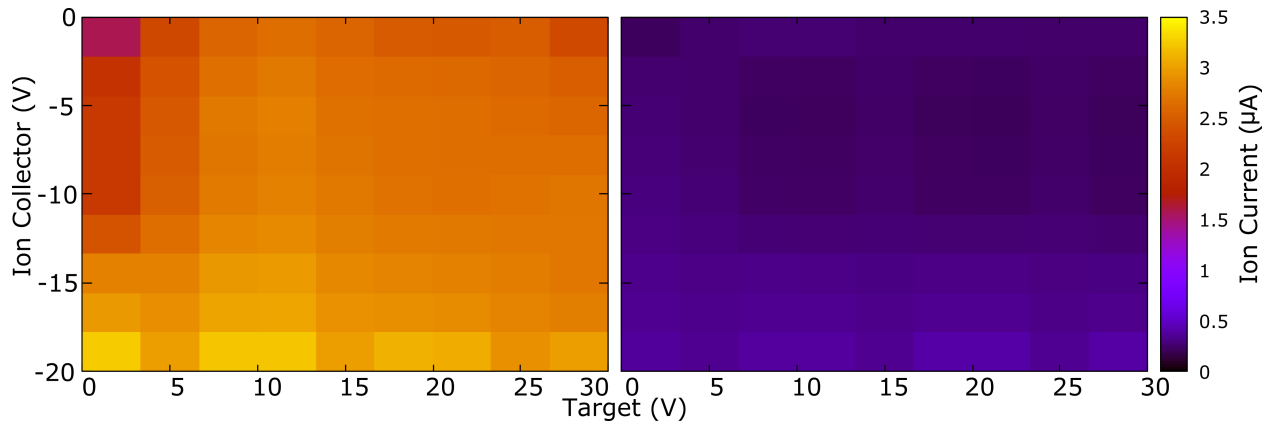
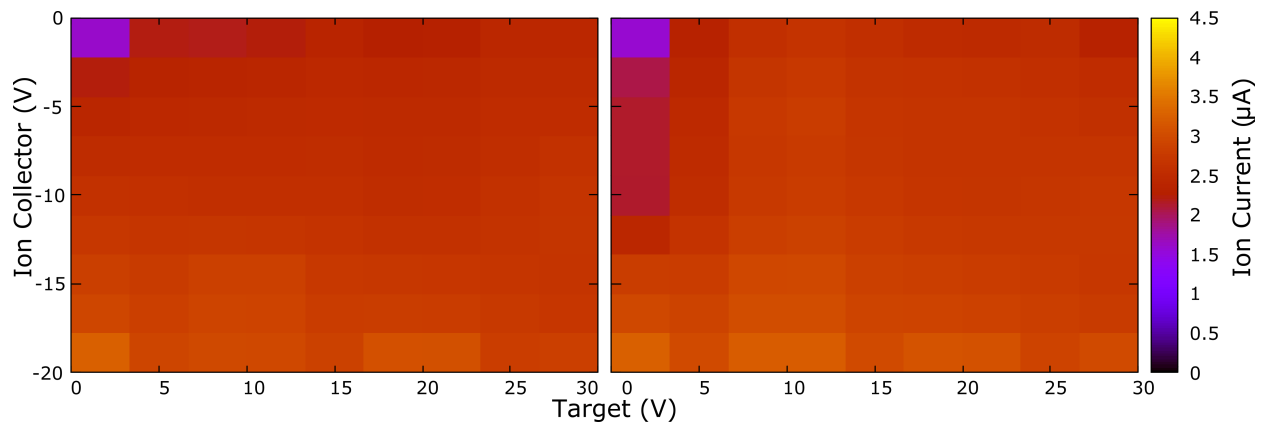
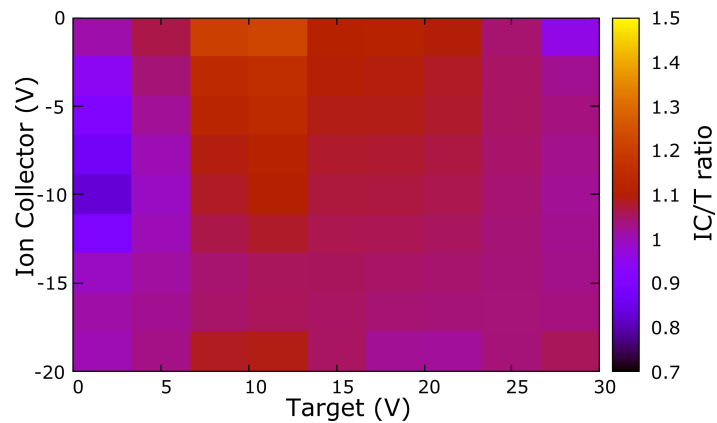


Figure 4.29: Previously shown Cu and Au results using the same ion current scale for comparison. A noticeable difference of almost one order of magnitude can be seen between the plots.

nected to the digital ammeter to measure the target's outgoing current. In principle, in an ideal system the measured values for the ion current would be the same in the collector plate and in the target with the outgoing current. The results were compared with previous measurements to show the system efficiency. The latter can be viewed in Figure 4.30. The top plots show the measured current values as function of the positive voltage applied to the target, and the negative voltage applied to the ion collector. Different colors represent current values within the range of $0\mu\text{A}$ - $4.5\mu\text{A}$. The left plot represents the obtained results when using the ion collector as the detection electrode. The right plot represents the target. The lower plot is the calculated ratio between the upper plots. It shows the variation in the measured ion current and consequently, the system efficiency on leaving and collecting ions. From Figure 4.30(a) it can be seen that both measured current values are very similar. However, Figure 4.30(b) highlights the fraction of the two measured values, i.e., the transport efficiency, which is close to 1 for most voltage value sets. Especially in the case with no bias at the target, the efficiency is reduced. Similar decrease in efficiency has been observed in SIMION simulations.



(a) The plots show the current measured from both electrodes as function of the applied voltage. Left: Ion current values as measured from the ion collector. Right: Ion current as measured from the target.



(b) This heat map shows the system efficiency on leaving and collecting ions. Different colors represent the variation in the measured ion current. This was obtained by finding the ratio between the upper plots.

Figure 4.30: Measured ion current from both electrodes, (a left) on collector and (a right) on target as function of the applied voltage. The bottom plot represents the ratio between the ion collector plate and the target measured values.

4.4 In-gas studies

After the successful in-vacuum measurements, the next step was to study the plume expansion within the presence of a background gas. Due to COVID-19 these measurements had to be postponed until after this MSc thesis. This work would study ion interaction and drift in GAr and GXe, with the latter being the main focus for the development of the Ba-tagging technique. The ablation process itself is expected to be similar in-vacuum and in-gas in a non-vacuum medium, although ion drift in gas is reduced.

The pressure chamber was modified to operate in high-pressure gas. The blank top flange was changed for a Pfeiffer Full Range Gauge PKR360. This gauge has an operating range from 10^{-9} Pa to 10^3 hPa (equivalent to 1 bar), allowing to measure from vacuum to a high pressure environment inside the chamber. A gas line was designed using 1/4" stainless steel pipes for incoming gas from the Xe Gas Handling System (XeGHS). A pressure regulator was installed to set the pressure inside the chamber. A MKS Baratron Pressure Transducer 622A, with operating range from 0.10 Torr to 1000 Torr, was added for measuring the pressure inside the chamber. This transducer must be connected to a ± 15 V power source through two different channels. The Baratron provides a measurement of the internal pressure by transforming mechanical impulses to electrical signals. The signals are read and interpreted by a Labjack T7, which is remotely controlled by the LJM interface where output voltages from 0 V to 10 V are directly proportional to 0 Torr - 1000 Torr. The test readings displayed a signal of 7.5 ± 0.1 V under atmospheric conditions, which corresponded to 756 ± 10 Torr in pressure units. This result agrees with the atmospheric pressure. In vacuum, the measured value was around $P = (4.3 \pm 0.1) \times 10^{-7}$ Torr as mentioned in section 4.3.

After the in-gas modifications, the optical setup of the LAS remained the same.

Anticipating results

Lower ion current values are expected to be measured when the ablation process is carried out under gaseous conditions. Since the gas acts as a damping force, it slows the transmission of ions. The intensity of the observed plasma is expected to decrease considerably as the gas pressure increases to ~ 10 mbar or more. This is attributed to Ar gas which cools down and confines the plasma plume [64]. In addition, for pressure values larger than 10^{-2} mbar, the experiment discussed in [67] showed a splitting of the ion plume. These and other gas-plasma interactions are yet to be studied under various applied biases and similar pressure values.

Chapter 5

Conclusions and outlook

The Laser Ablation Ion Source is a powerful tool to produce ions under very specific conditions. It allows the Ba-tagging group to study ion extraction properties for a future upgrade to nEXO. Through the study of background rejection techniques it is possible to anticipate the ion extraction and identification process of Ba-tagging.

The IGLAS system was commissioned and tested in vacuum conditions. In this setup the laser spot can be moved across a target. This allows the study of the ablation process and the repercussions in the target features. From the in-vacuum studies the following were determined:

- The beam spot size. This was determined by using two different methods. Through ablation marks in the surface of materials and by an analytical approach calculating the beam waist of the laser. Results agreed and are in the range of $\sim 100 \mu\text{m}$.
- The required voltages in the target and in the ion collector plate for the IGLAS system to read ion current under vacuum is in the range of 30 V.
- The data acquisition mode for ion current measurements. The measurements were initially carried out in manual-mode and then switched to auto-mode for higher precision. The resolution set values were also studied.

- The stability of the ion current. During ion current measurements, the UV beam should move over the target surface. The measured ion current is not stable over time, the melted material being the main cause of the current decrease.
- The average measured ion current in Cu for an angled target was in the range of hundreds of nA.
- The average measured current for a Cu and Au target respectively, perpendicular to the beam was in the range of hundreds of nA.
- The number of ions leaving the target. This is 6×10^5 and 6×10^6 ions per laser shot for Cu and Au, respectively.
- The overall behaviour of Cu and Au ion trajectories in a GAR and GXe background up to 10^5 Pa through SIMION simulations.

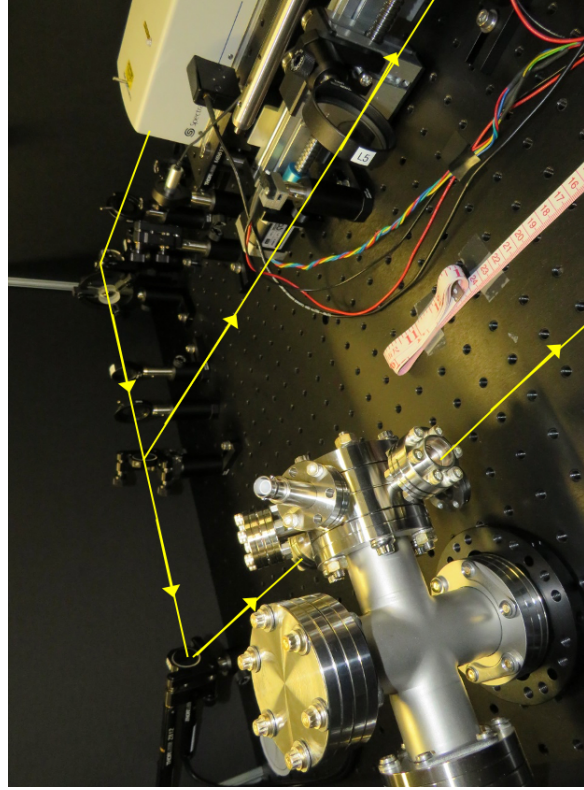
An external gas line for the IGLAS system was also built for coupling it to the gas handling system (XeGHS), currently under development.

Moving forward, the IGLAS system is now just a few steps from being tested in GAR and GXe. These measurements will consist in measuring the ion current from the ion collector plate and the target electrode while slowly increasing the pressure up to 10 bar to study the response of the setup. Additionally, a picoammeter will be included to particularly track the current leaving the target and the current received by the ion collector, at the same time. Another key improvement would be the image capturing technique. By using a device with higher exposure time, it will be feasible to study the growing process of the ion cloud.

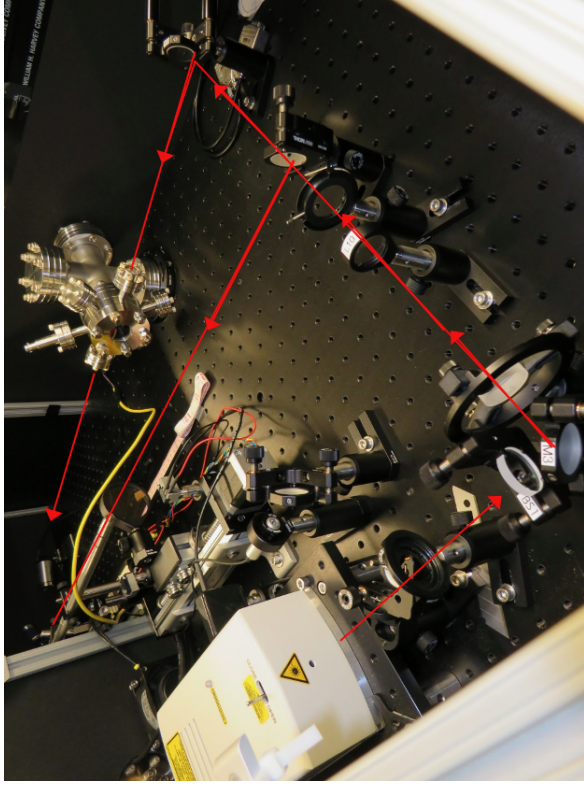
Lastly, this research represents a contribution on the ion identification for the Ba-tagging technique. It opened a way to study in-gas laser ablation which represents a

whole new challenge. The obtained results from the in-vacuum tests combined with the simulations provide an estimation of what to expect, and yet a lot remains to be explored.

Appendix



(a) UV optics as seen from the ending point of the laser trajectory.



(b) UV optics as seen from the starting point of the laser trajectory.

Figure 1: Optical path followed by the beam coming from the UV laser source. These pictures were taken from two opposite sides of the setup to provide an overview of the setup. The yellow and red lines represent the trajectory followed by the UV laser.

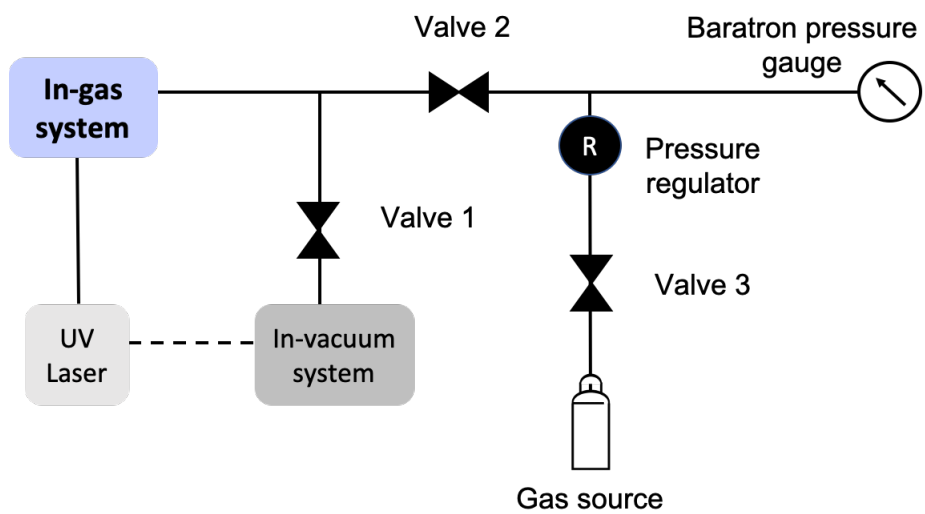


Figure 2: IGLAS gas line connecting the pressure chamber to the gas source.

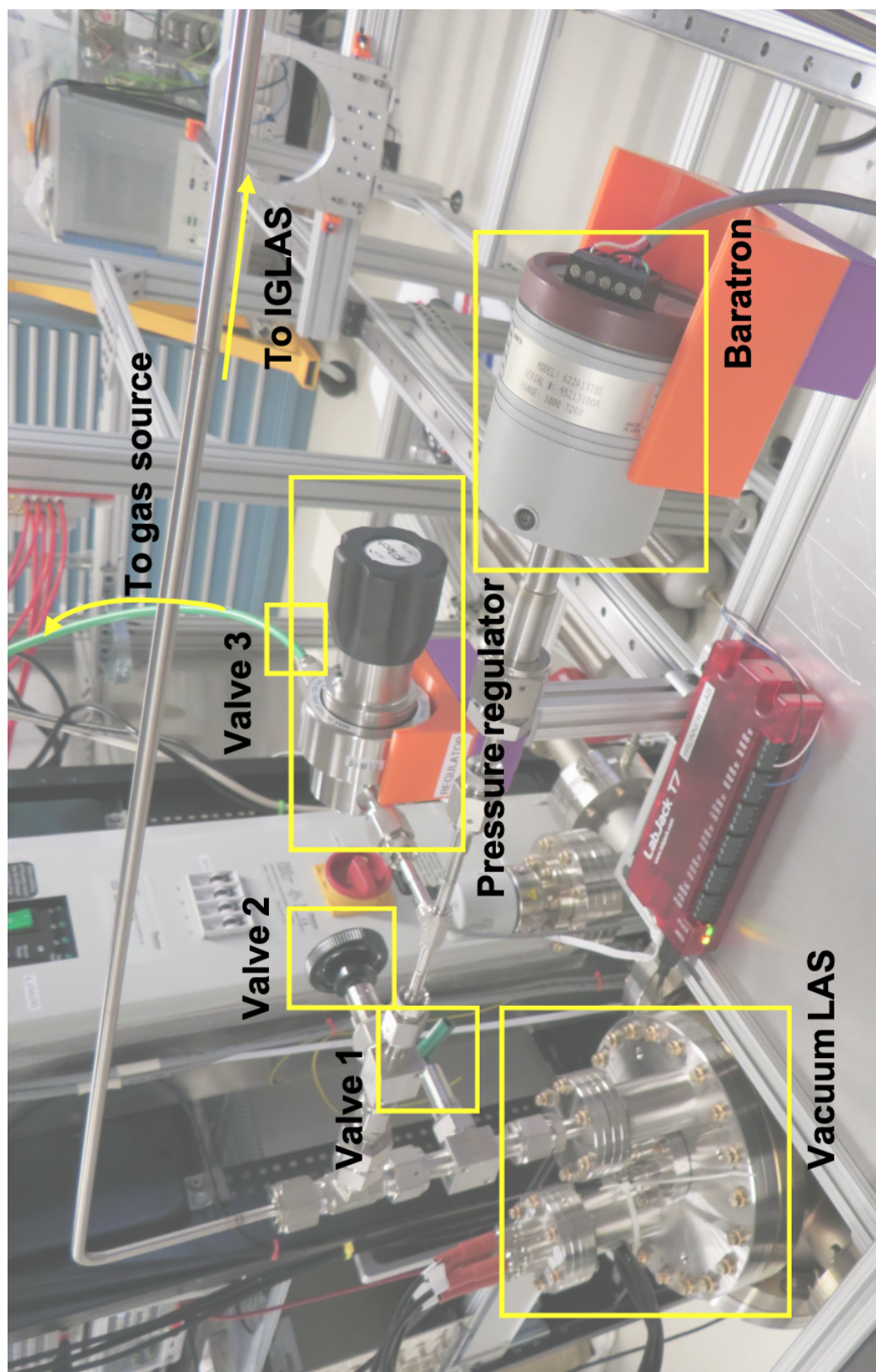


Figure 3: External view of the added gas line.

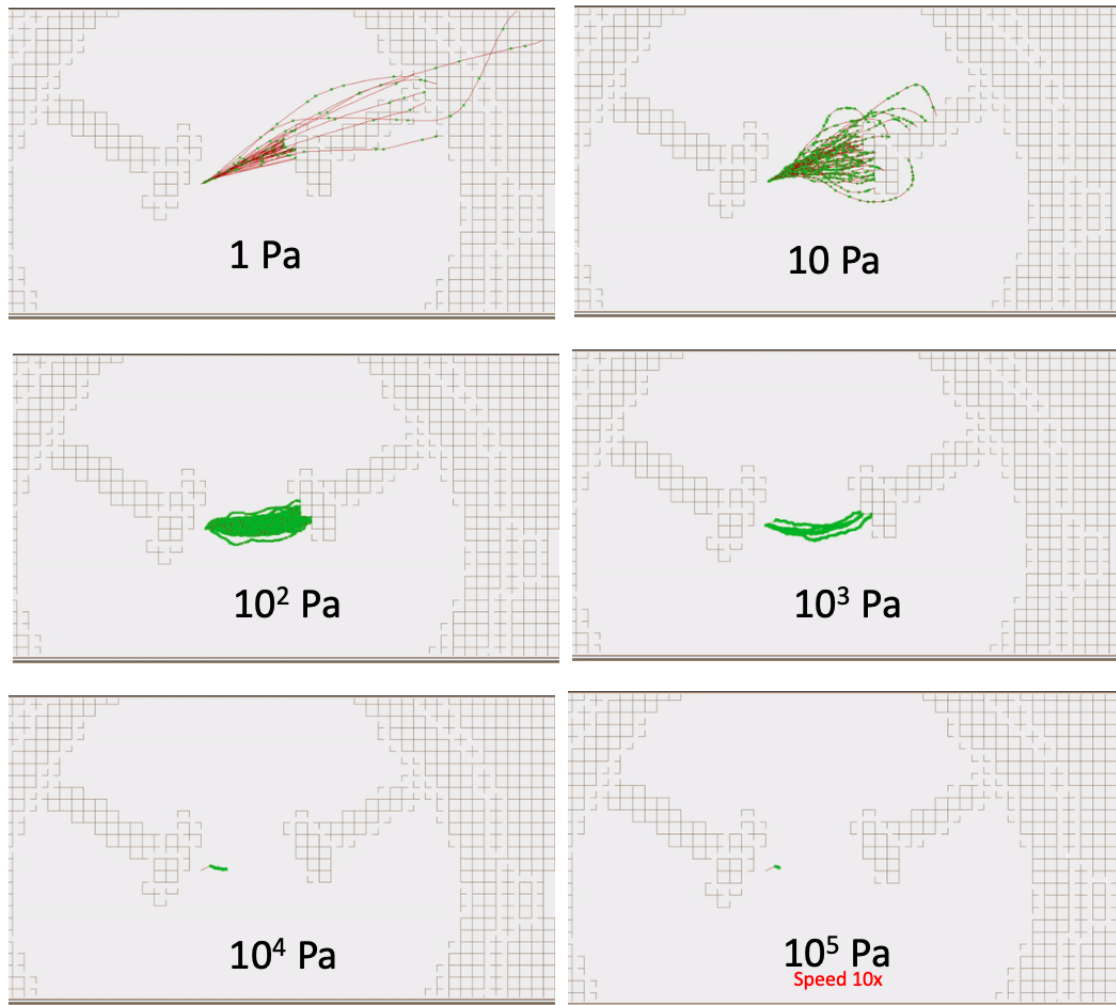


Figure 4: SIMION Simulations of a Cu sample in a GXe environment at 1 Pa, 10 Pa, 10² Pa, 10³ Pa, 10⁴ Pa and 10⁵ Pa. The particle trajectories can be observed for low pressure values and as the pressure is increased, so does the simulation times. The high pressure makes it more difficult to get ions directed from the target to the collector plate.

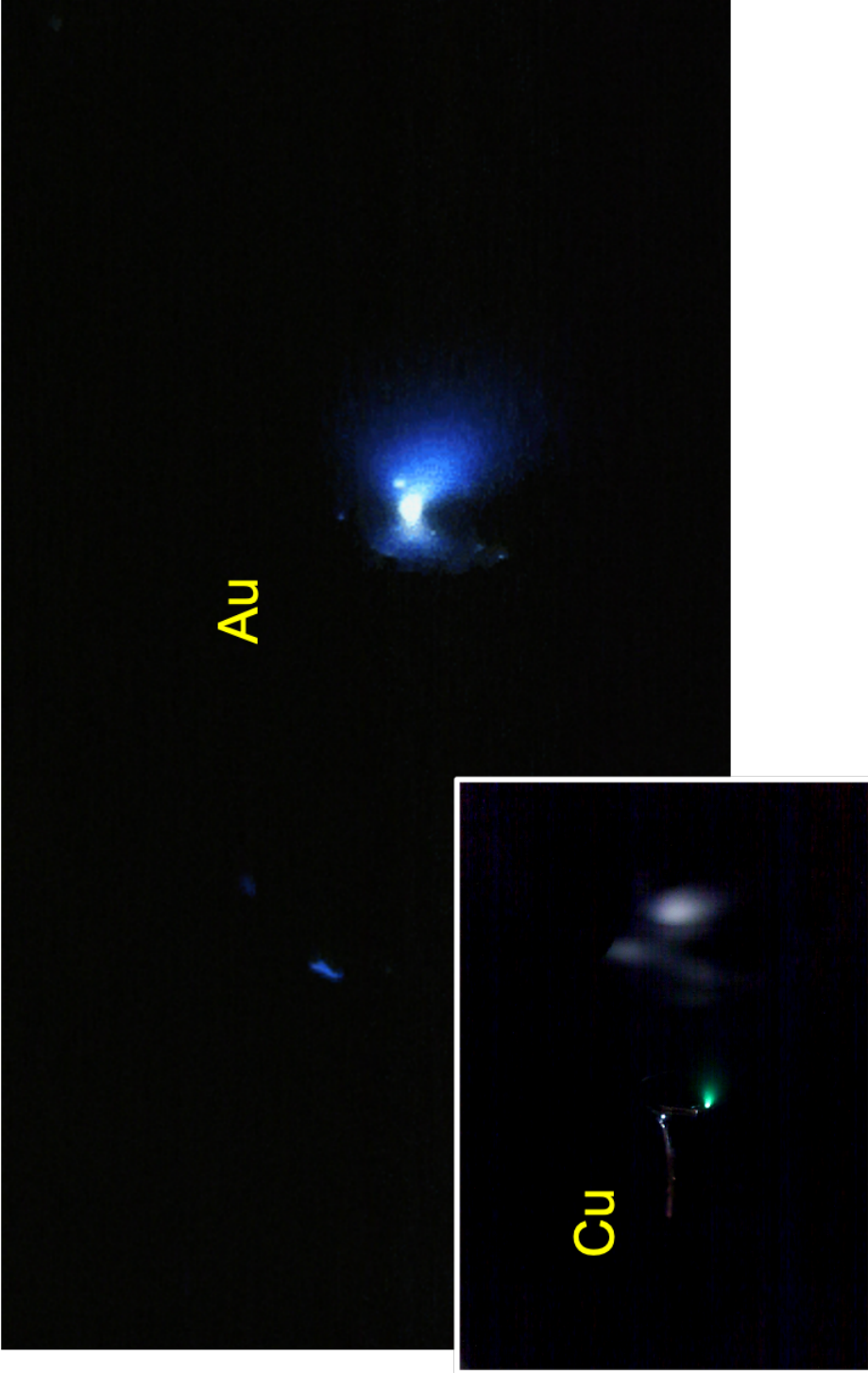


Figure 5: Ion cloud comparison. The resulting green and blue ion clouds are from copper and gold respectively.

Bibliography

- [1] D. J. Griffiths, *Introduction to elementary particles*. Physics textbook, Weinheim: Wiley-VCH, 2nd ed., 2008.
- [2] J. R. Gustafson, “Wolfgang Pauli 1900 to 1930: His Early Physics in Jungian Perspective,” 2010.
- [3] S. M. Bilenky, A. Faessler, and F. Šimkovic, “Majorana neutrino masses, neutrinoless double beta decay, and nuclear matrix elements,” *Physical Review D*, vol. 70, p. 033003, Aug. 2004.
- [4] Y. Fukuda *et al.*, “Evidence for oscillation of atmospheric neutrinos,” *Physical Review Letters*, vol. 81, pp. 1562–1567, 1998.
- [5] T. Araki *et al.*, “Measurement of neutrino oscillation with KamLAND: Evidence of spectral distortion,” *Physical Review Letters*, vol. 94, no. 8, pp. 081801–1, 2005.
- [6] A. B. McDonald, “Sudbury Neutrino Observatory Results,” *Physica Scripta*, vol. T121, pp. 29–32, 2005.
- [7] T. Kajita, “Discovery of atmospheric neutrino oscillations,” *Annalen der Physik*, vol. 528, pp. 459–468, May 2016.
- [8] G. Gratta and N. Kurahashi, “In search of no neutrinos,” *Physics world*, vol. 23, no. 04, pp. 27–30, 2010.

- [9] R. Cahn, D. Dwyer, S. Freedman, W. Haxton, R. Kadel, Y. Kolomensky, K. Luk, P. McDonald, G. Orebi Gann, and A. Poon, “White Paper: Measuring the Neutrino Mass Hierarchy,” in *Community Summer Study 2013: Snowmass on the Mississippi*, 7 2013.
- [10] X. Qian and P. Vogel, “Neutrino mass hierarchy,” *Progress in Particle and Nuclear Physics*, vol. 83, pp. 1–30, 2015.
- [11] K. Zuber, *Neutrino Physics*. CRC Press, 2020.
- [12] F. Reines and C. L. Cowan, “Neutrino physics,” *Physics Today*, vol. 10, no. 8, pp. 12–18, 1957.
- [13] M. Goepfert-Mayer, “Double beta-disintegration,” *Physical Review*, vol. 48, pp. 512–516, Sep. 1935.
- [14] C. A. Bertulani, *Nuclear physics in a nutshell*. In a Nutshell Series, Princeton University Press., 2007.
- [15] S. R. Elliott, A. A. Hahn, and M. K. Moe, “Direct evidence for two-neutrino double-beta decay in ^{82}Se ,” *Physical Review Letters*, vol. 59, pp. 2020–2023, Nov. 1987.
- [16] N. Ackerman *et al.*, “Observation of two-neutrino double-beta decay in Xe-136 with the EXO-200 detector,” *Physical Review Letters*, vol. 107, no. 21, p. 212501, 2011.
- [17] J. D. Vergados, H. Ejiri, and F. Šimkovic, “Theory of neutrinoless double-beta decay,” *Reports on Progress in Physics*, vol. 75, no. 10, p. 106301, 2012.
- [18] J. J. Gomez-Cadenas, J. Martín-Albo, M. Mezzetto, F. Monrabal, and M. Sorel, “The search for neutrinoless double beta decay,” *La Rivista del Nuovo Cimento*, vol. 35, no. 2, p. 29–98, 2012.
- [19] S. Herrin, *Double beta decay in Xenon-136: Measuring the neutrino-emitting mode and searching for Majoron-emitting modes*. PhD thesis, Stanford University, 2013.

- [20] H. V. Klapdor-Kleingrothaus, *Seventy years of double beta decay: from nuclear physics to beyond-standard-model particle physics*. World Scientific, 2010.
- [21] M. J. Dolinski, A. W. Poon, and W. Rodejohann, "Neutrinoless double-beta decay: Status and prospects," *Annual Review of Nuclear and Particle Science*, vol. 69, pp. 219–251, 2019.
- [22] S. Umehara, T. Kishimoto, I. Ogawa, R. Hazama, H. Miyawaki, S. Yoshida, K. Matsuoka, K. Kishimoto, A. Katsuki, H. Sakai, D. Yokoyama, K. Mukaida, S. Tomii, Y. Tatewaki, T. Kobayashi, and A. Yanagisawa, "Double beta decay of ^{48}Ca studied by $\text{CaF}_2(\text{Eu})$ scintillators," *Journal of Physics: Conference Series*, vol. 120, no. 5, p. 052058, 2008.
- [23] M. Agostini *et al.*, "Probing Majorana neutrinos with double- β decay," *Science*, vol. 365, no. 6460, pp. 1445–1448, 2019.
- [24] S. I. Alvis *et al.*, "Search for neutrinoless double- β decay in Ge-76 with 26 kg yr of exposure from the Majorana Demonstrator," *Physical Review C*, vol. 100, no. 2, p. 025501, 2019.
- [25] O. Azzolini *et al.*, "Final Result of CUPID-0 Phase-I in the Search for the Se-82 Neutrinoless Double- β Decay," *Physical Review Letters*, vol. 123, no. 3, p. 032501, 2019.
- [26] J. Argyriades *et al.*, "Measurement of the two neutrino double beta decay half-life of Zr-96 with the NEMO-3 detector," *Nuclear Physics A*, vol. 847, no. 3-4, pp. 168–179, 2010.
- [27] R. Arnold *et al.*, "Results of the search for neutrinoless double- β decay in Mo-100 with the NEMO-3 experiment," *Physical Review D*, vol. 92, no. 7, p. 072011, 2015.
- [28] A. Barabash *et al.*, "Final results of the Aurora experiment to study 2β decay of ^{116}Cd with enriched $^{116}\text{CdWO}_4$ crystal scintillators," *Physical Review D*, vol. 98, no. 9, p. 092007, 2018.

- [29] C. Arnaboldi, C. Brofferio, C. Bucci, S. Capelli, O. Cremonesi, E. Fiorini, A. Giuliani, A. Nucciotti, M. Pavan, M. Pedretti, G. Pessina, S. Pirro, C. Pobes, E. Previtali, M. Sisti, and M. Vanzini, “A calorimetric search on double beta decay of ^{130}Te ,” *Physics Letters B*, vol. 557, no. 3-4, pp. 167–175, 2003.
- [30] D. Q. Adams *et al.*, “Improved limit on neutrinoless double-beta decay in ^{130}Te with CUORE,” *Physical Review Letters*, vol. 124, p. 122501, Mar. 2020.
- [31] A. Gando *et al.*, “Search for Majorana Neutrinos Near the Inverted Mass Hierarchy Region with KamLAND-Zen,” *Physical Review Letters*, vol. 117, no. 8, p. 082503, 2016.
- [32] G. Anton *et al.*, “Search for neutrinoless double- β decay with the complete EXO-200 dataset,” *Physical Review Letters*, vol. 123, p. 161802, Oct. 2019.
- [33] R. Arnold *et al.*, “Measurement of the double-beta decay half-life and search for the neutrinoless double-beta decay of ^{48}Ca with the NEMO-3 detector,” *Physical Review D*, vol. 93, no. 11, p. 112008, 2016.
- [34] J. B. Albert *et al.*, “Improved measurement of the $2\nu\beta\beta$ half-life of ^{136}Xe with the EXO-200 detector,” *Phys. Rev. C*, vol. 89, p. 015502, Jan 2014.
- [35] J. Albert *et al.*, “Cosmogenic backgrounds to $0\nu\beta\beta$ in EXO-200,” *Journal of Cosmology and Astroparticle Physics*, vol. 2016, no. 04, pp. 029–029, 2016.
- [36] S. A. Kharusi *et al.*, “nEXO Pre-Conceptual Design Report.” arXiv:1805.11142, 2018.
- [37] M. Redshaw, E. Wingfield, J. McDaniel, and E. G. Myers, “Mass and Double-Beta-Decay Q-Value of Xe-136,” *Physical Review Letters*, vol. 98, no. 5, p. 053003, 2007.
- [38] J. B. Albert *et al.*, “Sensitivity and discovery potential of the proposed nEXO experiment to neutrinoless double- β decay,” *Physical Review C*, vol. 97, no. 6, p. 065503, 2018.

- [39] S. Kravitz, T. Brunner, D. Fudenberg, and nEXO Collaboration, “Barium Tagging for nEXO in Liquid and Gas Xenon,” in *APS April Meeting Abstracts*, vol. 2015 of *APS Meeting Abstracts*, p. S4.007, 2015.
- [40] M. K. Moe, “Detection of neutrinoless double-beta decay,” *Physical Review C*, vol. 44, pp. R931–R934, Sep 1991.
- [41] T. Brunner *et al.*, “An RF-only ion-funnel for extraction from high-pressure gases,” *International Journal of Mass Spectrometry*, vol. 379, pp. 110–120, 2015.
- [42] M. Green *et al.*, “Observation of single collisionally cooled trapped ions in a buffer gas,” *Physical Review A*, vol. 76, no. 2, p. 023404, 2007.
- [43] R. E. Russo, “Laser ablation,” *Applied Spectroscopy*, vol. 49, no. 9, pp. 14A–28A, 1995.
- [44] S. Canulescu, T. Lippert, and A. Wokaun, “Mass and kinetic energy distribution of the species generated by laser ablation of $\text{La}_{0.6}\text{Ca}_{0.4}\text{MnO}_3$,” *Applied Physics A*, vol. 93, no. 3, pp. 771–778, 2008.
- [45] N. Angert, “Ion sources,” in *CERN Accelerator School: Course on General Accelerator Physics*, pp. 619–642, 1992.
- [46] C. W. Schneider and T. Lippert, *Laser Ablation and Thin Film Deposition*, pp. 89–112. Berlin, Heidelberg: Springer Berlin Heidelberg, 2010.
- [47] D. A. Davies, D. J. Morrissey, G. Bollen, P. A. Lofy, J. Ottarson, and S. C. Schwarz, “A high-power laser ablation ion source for penning trap studies of nuclear reaction products,” *Journal of Physics: Conference Series*, vol. 59, pp. 136–139, 2007.
- [48] S. Mihai, M. Aurelian, and N. N. Puscas, *Pulsed Laser Ablation of Solids Basics, Theory and Applications*. Springer Series in Surface Sciences, Springer, 2014.
- [49] T. E. Lellinger, “Ion production by pulsed laser ablation in a helium atmosphere,” Master’s thesis, Technical University Darmstadt, 2019.

- [50] S. Amoruso, R. Bruzzese, N. Spinelli, and R. Velotta, "Characterization of laser-ablation plasmas," *Journal of Physics B: Atomic, Molecular and Optical Physics*, vol. 32, pp. R131–R172, Jul. 1999.
- [51] Laser shop online, "Configuration of optics." <https://laseroflove.wordpress.com/2010/03/05/configuration-of-optics/>. [accessed: 20.09.2020].
- [52] A. Bogaerts, Z. Chen, and D. Bleiner, "Laser ablation of copper in different background gases: comparative study by numerical modeling and experiments," *Journal of Analytical Atomic Spectrometry*, vol. 21, p. 384, 2006.
- [53] B. Toftmann, J. Schou, and S. Canulescu, "Energy distribution of ions produced by laser ablation of silver in vacuum," *Applied Surface Science*, vol. 278, pp. 273–277, 2013.
- [54] B. Wolf, *Handbook of Ion Sources*. CRC Press, 2017.
- [55] B. Toftmann and J. Schou, "Time-resolved and integrated angular distributions of plume ions from silver at low and medium laser fluence," *Applied Physics A*, vol. 112, no. 1, pp. 197–202, 2012.
- [56] C. R. Phipps, *Laser ablation and its applications*. Springer, 2007.
- [57] F. Belloni, D. Doria, A. Lorusso, V. Nassisi, and L. Torrisi, "Development of an ion source via laser ablation plasma," *Conference Proceedings C*, vol. 060626, pp. 3119–3121, 2006.
- [58] D. A. Davies, *A high-power Laser Ablation Ion Source for Penning trap studies of rare isotopes*. PhD thesis, Michigan State University, 2006.
- [59] M. Okamura, "Laser ion source for heavy ion inertial fusion," *Matter and Radiation at Extremes*, vol. 3, no. 2, pp. 61–66, 2018.

- [60] D. Dahl, "Simion 3D Version 6.0 User's Manual," 1995.
- [61] R. Chang, *Essential chemistry*. McGraw-Hill, 1996.
- [62] W. R. Inc., "Van Der Waals Radius of the elements." <https://periodictable.com/Properties/A/VanDerWaalsRadius.v.html>. [accessed: 05.01.2020].
- [63] B. Doggett and J. G. Lunney, "Expansion dynamics of laser produced plasma," *Journal of Applied Physics*, vol. 109, p. 093304, May 2011.
- [64] A. Khalil, "Production of current and ion beams on a copper surface by laser radiation of various wavelengths under the presence of an applied electric field," *Surface Coatings Technology*, vol. 200, pp. 774–779, 10 2005.
- [65] Thorlabs, "Beam splitters." https://www.thorlabs.com/newgrouppage9_pf.cfm?guide=10&category_id=155&objectgroup_id=913. [accessed: 08.01.2020].
- [66] A. H. Hamad, K. S. Khashan, and A. A. Hadi, "Laser ablation in different environments and generation of nanoparticles," in *Applications of Laser Ablation - Thin Film Deposition, Nanomaterial Synthesis and Surface Modification*, InTech, 2016.
- [67] S. Amoruso, A. Sambri, and X. Wang, "Propagation dynamics of a LaMnO₃ laser ablation plume in an Oxygen atmosphere," *Journal of Applied Physics*, vol. 100, no. 1, p. 013302, 2006.
- [68] Image J, "Image J features." <https://imagej.nih.gov/ij/features.html>. [accessed: 08.01.2020].
- [69] Keysight technologies, "Keysight Truevolt Series Digital Multimeters: Operating and Service Guide." <https://literature.cdn.keysight.com/litweb/pdf/34460-90901.pdf>. [accessed: 08.10.2020].

- [70] K. K. Anoop, X. Ni, M. Bianco, D. Paparo, X. Wang, R. Bruzzese, and S. Amoruso, "Two-dimensional imaging of atomic and nanoparticle components in copper plasma plume produced by ultrafast laser ablation," *Applied Physics A*, vol. 117, no. 1, pp. 313–318, 2014.
- [71] S. S. Harilal, C. V. Bindhu, M. S. Tillack, F. Najmabadi, and A. C. Gaeris, "Internal structure and expansion dynamics of laser ablation plumes into ambient gases," *Journal of Applied Physics*, vol. 93, no. 5, pp. 2380–2388, 2003.
- [72] O. Auciello, J. Emerick, J. Duarte, and A. Illingworth, "New rotating target holder for laser ablation and ion beam sputter deposition of multicomponent and multilayered thin films," *Journal of Vacuum Science & Technology A: Vacuum, Surfaces, and Films*, vol. 11, no. 1, pp. 267–270, 1993.
- [73] T. Donnelly, J. G. Lunney, S. Amoruso, R. Bruzzese, X. Wang, and X. Ni, "Dynamics of the plumes produced by ultrafast laser ablation of metals," *Journal of Applied Physics*, vol. 108, no. 4, p. 043309, 2010.